ERDC/GSL TR-18-20

Geotechnical and Structures Laboratory

US Army Corps
of Engineers®
Engineer Research and
Development Center

ERDC
ENGINEER RESEARCH & DEVELOPMENT CENTER

U.S. Air Force Rapid Airfield Damage Repair (RADR) Program

Camouflet Repair Alternatives

Ben C. Cox and Thomas A. Carr

August 2018

The U.S. Army Engineer Research and Development Center (ERDC) solves the nation's toughest engineering and environmental challenges. ERDC develops innovative solutions in civil and military engineering, geospatial sciences, water resources, and environmental sciences for the Army, the Department of Defense, civilian agencies, and our nation's public good. Find out more at www.erdc.usace.army.mil.

To search for other technical reports published by ERDC, visit the ERDC online library at http://acwc.sdp.sirsi.net/client/default.

ERDC/GSL TR-18-20
August 2018

Camouflet Repair Alternatives

Ben C. Cox and Thomas A. Carr

Geotechnical and Structures Laboratory
U.S. Army Engineer Research and Development Center
3909 Halls Ferry Road
Vicksburg, MS 39180-6199

Final report

Prepared for Headquarters, Air Force Civil Engineer Center
139 Barnes Avenue, Suite 1
Tyndall AFB, FL 32403-5319

Under Project 457442; Rapid Airfield Damage Repair (RADR) Program

Abstract

The inability to operate aircraft on a runway after an attack on an airbase poses significant operational challenges. To address limitations of legacy airfield damage repair (ADR) equipment, materials, and tactics, the U.S. Air Force Air Combat Command began the ADR Modernization program, which eventually transitioned to the Rapid ADR (RADR) program. Within the RADR program, this project's objective was to investigate repair materials and methods for camouflets (i.e., subsurface cavities created by the penetration and detonation of an explosive ordnance).

The objective was accomplished through laboratory testing and full-scale testing at the Silver Flag Exercise Site at Tyndall Air Force Base, FL. A method was developed to quickly provide reasonable camouflet volume estimates. Various repair materials were used to repair simulated camouflets that were trafficked at 30-min to 2-hr cure times with a load cart simulating C-17 aircraft. Repairs sustained 112 passes up to 1,568 passes. Repair performance was controlled primarily by existing concrete slab thickness and strength; repair material strength had no perceivable impact (all other factors being equal, this would not be expected to be the case). Repair performance was not adversely affected for the suggested 30-min cure time.

Contents

Figures and Tables

Figures

Tables

Preface

This study was conducted for the U.S. Air Force Civil Engineer Center (AFCEC), Tyndall Air Force Base, FL. The program manager for this project was Dr. Robert Diltz of AFCEC.

The work was performed by the Airfields and Pavements Branch (GMA) of the Engineering Systems and Materials Division (GM), U.S. Army Engineer Research and Development Center, Geotechnical and Structures Laboratory (ERDC-GSL). Mr. Jeb S. Tingle provided technical oversight of the project for ERDC.

At the time of publication, Dr. Timothy W. Rushing was Chief, CEERD-GMA; Dr. Gordon W. McMahon was Chief, CEERD-GM; and Ms. Pamela G. Kinnebrew, CEERD-GZT, was Technical Director for Military Engineering. Dr. William P. Grogan was Deputy Director, ERDC-GSL, and Mr. Bartley P. Durst was Director.

COL Ivan P. Beckman was the Commander of ERDC, and Dr. David W. Pittman was the Director.

Unit Conversion Factors

Multiply	By	To Obtain
degrees Fahrenheit	(F-32)/1.8	degrees Celsius
feet	0.3048	meters
gallons (U.S. liquid)	0.1336	cubic feet
inches	0.0254	meters
miles per hour	0.44704	meters per second
pounds (mass)	0.45359237	kilograms
square feet	0.09290304	square meters
square yards	0.8361274	square meters
yards	0.9144	meters

1 Introduction

1.1 Background

The inability to operate aircraft on a runway after an attack on an airbase poses significant operational challenges. Airfield Damage Repair (ADR) equipment, materials, and tactics are utilized in recovery activities in response to such an attack in order to recover the airfield operating surfaces. Resuming aircraft launch and recovery operations as quickly as possible is often a first-order concern; therefore, it is critical to complete ADR activities in an efficient and expedient manner. Within the context of the U.S. Air Force Rapid ADR (RADR) program, this report documents an investigation of equipment, materials, and tactics for repair of camouflets.

A camouflet is a subsurface cavity caused by the penetration and detonation of an explosive ordnance that results in varying degrees of surface damage. Davis (1976) identified seven classifications of bomb damage in runway pavements; three of these were camouflets: (1) a camouflet with a spall crater, (2) a camouflet with a heave mound, and (3) a standard camouflet (i.e., little to no surface damage other than the ordnance point of entry (OPE). Discussions with the U.S. Air Force Civil Engineer Center (AFCEC) indicated that, in their attempts to simulate camouflets with manually placed explosive charges, four types of surface damage were encountered: (1) little to no surface damage other than the simulated OPE, (2) minor to moderate cracking around the simulated OPE, (3) upheaval of the pavement surface, and (4) collapse of the pavement surface. Although the degree of surface damage of a camouflet can vary, the key distinction between a camouflet and a crater is that a camouflet exhibits a large subsurface damage radius relative to the surface damage, resulting in a pavement surface section (e.g., a concrete slab) that has no supporting base material underneath and is susceptible to collapse under vehicle or aircraft loads. In general, camouflet subsurface void characteristics have not been studied or documented on a widespread basis.

Since 2006, engineers at the U.S. Army Engineer Research and Development Center (ERDC) have been conducting modern ADR research, in which time considerable effort has been devoted to ADR techniques such as those used to repair several large craters or numerous small craters. In contrast, camouflet repair methodologies have been

studied to a lesser extent. While some traditional ADR methodologies, such as those used for craters, may also be applicable to camouflets, some typical crater repair procedures, such as saw-cutting and debris removal, are likely unnecessary where pavement surfaces surrounding a camouflet remain relatively intact. Instead, methods and materials for adequately backfilling and stabilizing camouflet subsurface voids need to be evaluated for construction and structural feasibility. Adapting current ADR technologies and methods to suit camouflet repair needs provides a logical path forward in order to best utilize currently fielded technologies.

1.2 Objectives

The overall objective of this project was to evaluate camouflet repair alternatives. Specific objectives are as follows.

1. Better characterize attributes of camouflet subsurface voids,
2. Evaluate proper construction practices for effectively and efficiently repairing camouflets,
3. Evaluate the suitability of different repair materials for camouflet repairs to support heavy cargo aircraft operations.

1.3 Scope

To achieve these objectives, laboratory testing was conducted alongside full-scale field testing. Simulated camouflets were created with manually-placed explosive charges at the Silver Flag Exercise Site, Tyndall AFB, FL. Void characterization was conducted on these full-scale camouflets followed by subsequent repairs. Repairs were trafficked with simulated C-17 traffic, and data were collected and analyzed to evaluate repair integrity.

Camouflets in concrete pavements were the focus of this project since it was expected that craters, rather than camouflets, are more likely to be encountered in asphalt pavements. Full-scale simulated camouflets were designed to target the standard camouflet (Austin et al. 1984) with no cracking to moderate cracking around the simulated OPE and less than 0.75 in. of upheaval or collapse. Subsurface void characterization focused on providing information on void characteristics for research purposes as well as for the development of rapid field assessments of void volume. Unexploded ordnance (UXO) detection was not a part of this project. In all, 13 simulated camouflets were attempted during blasting, and 10 were ultimately repaired and trafficked. This project was conducted from

January to December 2016 with full-scale field testing at Silver Flag occurring in September 2016.

1.4 Outline of chapters

Chapter 2 presents a literature review encompassing camouflets and repair materials. Chapter 3 details the experimental program utilized in this project. Chapter 4 provides laboratory material characterization results. Chapter 5 presents results from laboratory and field void characterization trials. Chapter 6 discusses the full-scale camouflet repair processes and presents repair evaluation results throughout trafficking. Chapter 7 provides a discussion of all results, and Chapter 8 describes the conclusions and recommendations. Appendix A provides camouflet photographs, Appendix B provides a summary of the recommended camouflet repair process, and Appendix C provides drawings of the Modified Laser Range Finder device used to characterize camouflet voids.

2 Literature Review

2.1 Camouflets

Camouflets have not been documented in a widespread manner, though a limited amount of camouflet literature is publicly available. Davis (1976) investigated aspects of airfield runway vulnerability and runway crater damage, among other items. Seven classifications of airfield damage that can be formed by explosions on, in, or underneath pavements were described and are shown in Figure 2.1. The formation of a given type of damage results from a combination of ordnance size and type, depth of blast, pavement thickness, and subsurface characteristics (i.e., base, subbase, subgrade). Though not stated as a factor in Davis (1976), it is also likely that ordnance angle of attack, water table depth, and soil saturation conditions have some effect on damage characteristics. As shown in Figure 2.1e to Figure 2.1g, Davis (1976) defined three unique types of camouflets: camouflets with a spall crater (Type 5), camouflets with a heave mound (Type 6), and standard camouflets (Type 7). Nearly 10 years later, Austin et al. (1984) presented a state-of-the-art survey on damage-resistant pavements and also utilized the same seven damage classifications as Davis (1976).

Davis (1976) provided a brief summary of USAF camouflet repair recommendations at the time. For Type 5, 6, and 7 camouflets (Figure 2.1) where the degree of heave over a Type 6 camouflet was not severe, it was recommended to fill the camouflet void through the OPE with a free-flowing material in order to easily pass through the hole. Materials mentioned were sand, small-sized select aggregate, and quick-setting concrete. Once the void was filled up to the bottom of the OPE hole, it was recommended that sand and aggregate fill be ram-tamped and concrete fill be vibrated. The remaining OPE hole, or spall crater in the case of Type 5 camouflets, would then be filled with a resin or quick-setting concrete. For Type 6 camouflets where slab heave was severe, it was stated that the camouflet should be repaired as if it were a Type 3 or 4 crater (i.e., remove damaged concrete and repair using traditional crater repair methods).

Figure 2.1. Bomb damage classifications (cross indicates depth of blast).

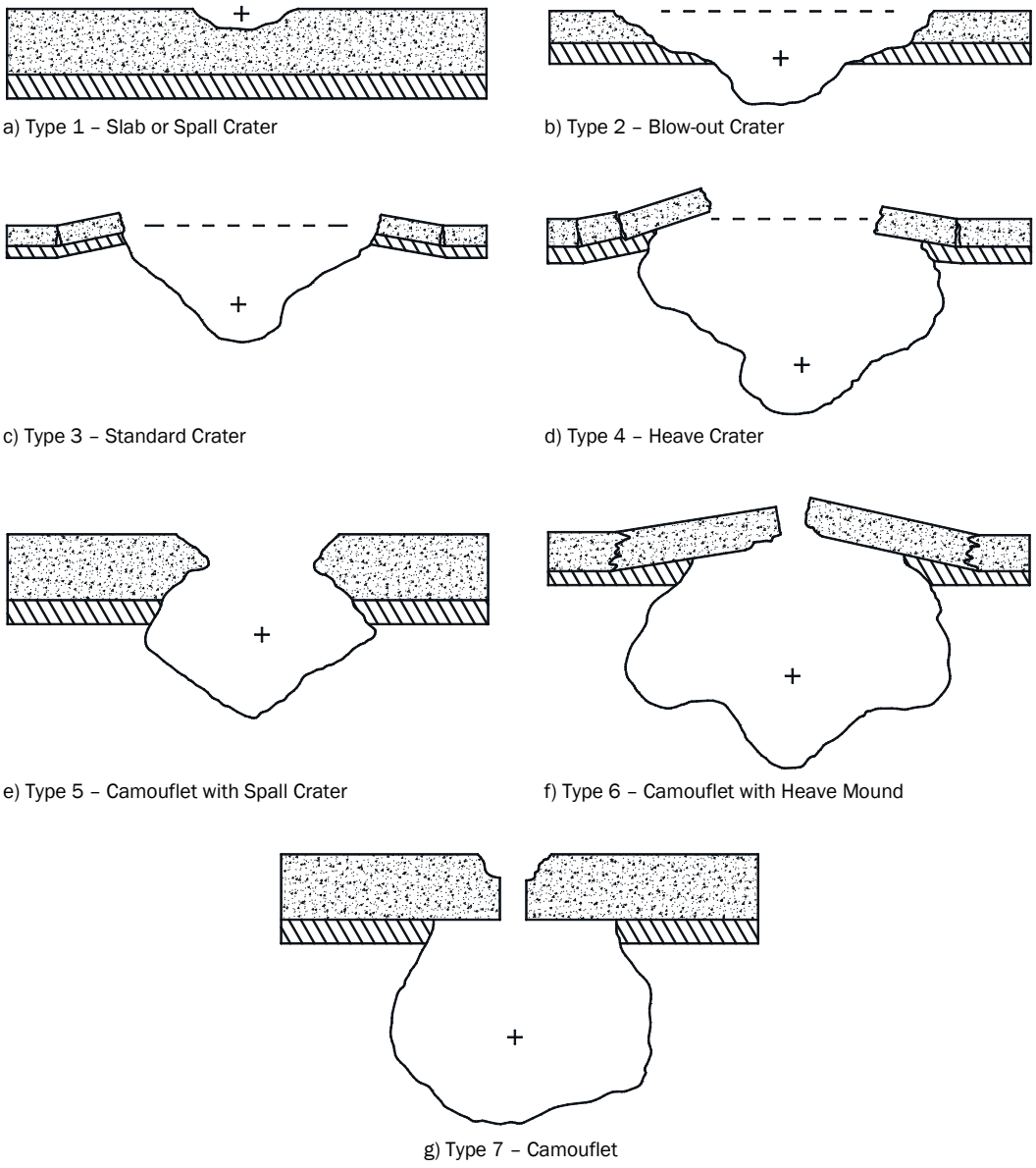

There are multiple publications by J.W. Bull and C.H. Woodford that provide useful background information on camouflets and present their use of finite element modeling of camouflets (Bull and Woodford 1996, 1998a, 1998b, 1999, 2000, 2001, 2003). Work presented within these papers was fairly similar, especially regarding camouflet background information. Therefore, further discussion herein is presented collectively from Bull and Woodford's works with specific references to individual publications provided where needed for clarity.

Bull and Woodford used a diagram similar to that in Figure 2.2 to describe camouflets and also in developing finite element models. The term "optimum depth" was used to refer to the depth below the air-ground interface at which a detonation produces the maximum apparent and maximum true crater diameters and depths. An apparent crater refers to a crater as it appears following an explosion (i.e., with disturbed materials remaining in the crater), whereas a true crater would be larger and refers to the crater that would remain if all disturbed materials (e.g., concrete, subgrade) were removed. Bull and Woodford maintained that a detonation occurring greater than the optimum depth would produce a camouflet having three primary characteristics that can be seen in Figure 2.2: (1) a hollow spherical cavity which may collapse on itself with time, (2) a shell of densified subgrade material surrounding the cavity, and (3) an inverted cone of disturbed material extending to the air-ground interface with its apex at the point of detonation. In addition, a shaft left by the ordnance upon entry may or may not be visible.

Figure 2.2. Camouflet showing disturbed subgrade zones.

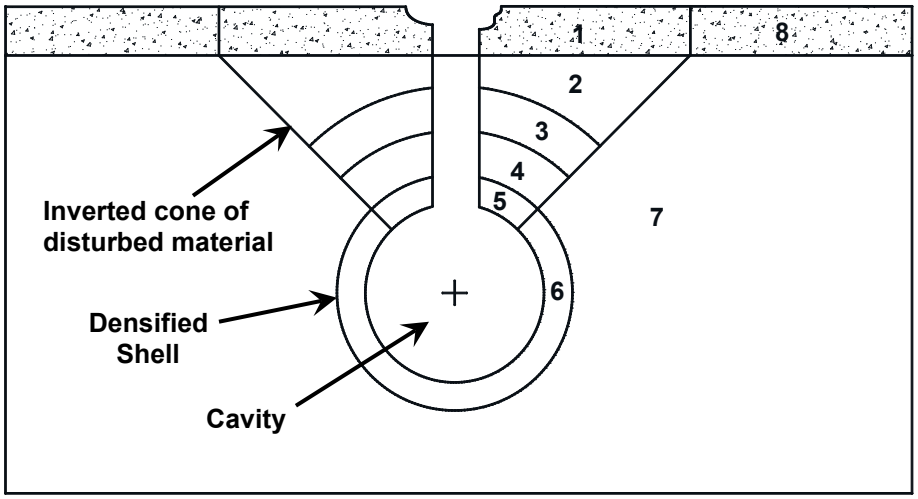

There are several variables that can affect camouflet characteristics such as mass of the explosive, detonation depth, and properties of surrounding medium. Consequently, defining exact optimum depths for camouflets is not straightforward. Bull and Woodford discussed two common means of describing and distinguishing camouflets from craters.

First, Bull and Woodford referenced work where a Z/R aspect ratio parameter (crater depth (Z) divided by crater radius (R)) was used to categorize detonation depth on a normalized scale. Shallow detonation

depths ($Z/R \leq 1.0$) produced hemispherical craters with no appreciable heaving or cracking within the pavement beyond the crater. Deep detonation depths ($Z/R > 5.0$) produced no apparent crater but instead produced a camouflet cavity with a small OPE hole at the surface accompanied with extensive heaving and radial cracking in the overlying concrete. Intermediate detonation depths ($1.0 < Z/R \leq 5.0$) exhibited characteristics of both.

Second, Bull and Woodford described crater and camouflet characteristics using Hopkinson's Law, or the cube root scaling law, which states that any dimension of a crater or camouflet may be expressed as some constant multiplied by $W^{0.33}$, where W is the mass of the equivalent yield of TNT of the explosive charge. This law was used to express diameter and volume estimations as discussed later but was also used to derive another means of distinguishing craters and camouflets. The parameter λ_c is the detonation depth divided by $W^{0.33}$ as shown in Equation 2.1; therefore, λ_c is another type of normalized depth term. λ_c is equal to zero for a detonation occurring at the air-ground interface and less than zero for a detonation occurring below the air-ground interface.

$$\lambda_c = -\frac{Z}{W^{0.33}} \tag{2.1}$$

Where

λ_c = detonation depth normalized by explosive charge size
Z = detonation depth beneath the air-ground interface (ft)
W = mass of equivalent yield of TNT (lb)

Similar to the Z/R ratio classifications, three classifications were given based on the value of λ_c. Conventional crater shapes corresponded to λ_c values between -2.0 and 0.5. The apparent crater size increases as λ_c decreases (i.e., depth increases) up to a point; then the apparent crater size decreases as λ_c decreases further and increasing amounts of material initially expelled from the crater fall back into it. The maximum apparent crater is formed when λ_c is between -1.0 and -1.5, while the maximum true crater is formed when λ_c equals approximately -2.0. Camouflets corresponded to a λ_c value less than -3.5 and may exhibit no disturbance at the pavement surface, a small mound, a depression, a hole, or only loose subgrade. With λ_c between -2.0 and -3.5, the damage appears to be a

conventional crater but is more appropriately a partial camouflet. While the apparent crater may appear small and suggest only a small ordnance was detonated, the reality is that a considerable depth of material has been disturbed, which should be taken into account during repairs.

Bull and Woodford described the process of camouflet formation as follows. The shock wave and high gas pressures produced from a detonation would result in the plastic deformation and densification of the surrounding subgrade forming an approximately spherical cavity with a densified outer shell (zone 6 in Figure 2.2). On the shock wave front, voids within the soil would collapse due to the compressive stresses induced, and the soil would densify. Behind the shock wave front, the subgrade would rebound slightly. When this shock wave reaches significant pavement layer changes (e.g., between soil and concrete, between concrete and air), a negative shock wave would be generated that propagates back into the subgrade. Intersecting shock waves could produce considerable tensile stresses which, if exceeding the subgrade's tensile strength, could cause the subgrade to break in tension, or spall, creating free surfaces and weakening the subgrade. This seems most likely to occur within the cone of disturbed material (zones 2 through 5 in Figure 2.2).

Experimental data referenced in Bull and Woodford (1999) cited experimental data from other references and proposed that camouflet diameter (D) in the vertical (D_v) and horizontal (D_h) directions is equal to Equation 2.2. Further, the cavity was shown to be nearly spherical. One reference provided a range of a values of 1.9 to 2.7 for calculating apparent diameters in cohesive soils with moderate moisture contents and stated that true camouflet diameters (i.e., the diameter including the outer densified shell, or zone 6 in Figure 2.2) would be approximately 20% greater. Others reported values of a between 2.9 and 3.0 or 2.5 and 2.7. Another reported that D_v was 91% of D_h on average and, thus, reported two unique ranges of values for a.

$$D_v \text{ or } D_h = a \times W^{0.33} \tag{2.2}$$

Where

D_v or D_h = vertical or horizontal camouflet diameter (ft)
a = constant equal to 1.9-2.7; 2.9-3.0; 2.5-2.7; or 1.83-2.32 for D_v and 1.98-2.45 for D_h
W = mass of equivalent yield of TNT (lb)

Bull and Woodford (1999) also provided Equation 2.3 as a means to estimate camouflet volume, which was assumed to be true volume given the context, though this was somewhat unclear.

$$V = b \times W \tag{2.3}$$

Where

V = true camouflet volume (ft^3)
b = constant equal to 9 to 11
W = mass of equivalent yield of TNT (lb)

With respect to depths, diameters, and volumes, it is important to note that values which Bull and Woodford's works were considering were significantly greater than those presented in later chapters of this report. A diameter of 20.5 ft was used in models (Bull and Woodford 2003) based on a 470-lb TNT charge. Several depths were modeled ranging from approximately 27 to 60 ft. For this reason, relationships (e.g., Equations 2.1 to 2.3) may not be accurate or as appropriate when scaled to the smaller camouflet sizes presented in this report.

Over time, a camouflet cavity will collapse, further disturbing the surrounding subgrade. The time required for this to occur would be dependent primarily on subgrade properties. In rock, the cavity may collapse within a few minutes (Bull and Woodford 2001). In saturated or partially saturated sandy soils, the cavity may collapse within a few days, while the cavity may remain stable for years in unsaturated cohesive soils (Bull and Woodford 1999). Bull and Woodford (2001) stated that cavity collapse usually occurs either quickly in one stage or progressively in multiple stages as the dome of material in the roof of the cavity succumbs to excessive stress states. Dome collapse could be severe enough that a visible basin of ground settlement could be observed on the surface. The collapse could also fill the cavity with loose material yet have visible effects on the surface though structural capacity may be greatly reduced. Lastly, during the collapse, material may bridge on itself and form a new stable but fragile dome.

All Bull and Woodford publications referenced in this report presented camouflet finite element modeling. The general modeling format within each publication was similar; slight variations were utilized to consider

various scenarios, repair materials, etc. In each publication, finite element modeling was conducted for multiple material property cases. Up to 17 cases were considered in addition to an undisturbed (i.e., camouflet not present) case. For the undisturbed case, a subgrade California Bearing Ratio (CBR) of 9.5 was assumed and was used to obtain an elastic modulus of approximately 14,000 psi following the approximation that modulus is equal to 1,500 times CBR. Concrete modulus was fixed at 5.2 million psi for all cases. For disturbed cases, subgrade modulus values were varied by zone (same zones in Figure 2.2) and either remained the same (14,000 psi), doubled, increased 10 times, or decreased 13.5 times. For example, zone 6 was normally assigned a 140,000 psi modulus since it was expected to be considerably densified. Zone 7 modulus was always fixed at 14,000 psi. Variations with modulus occurred mostly in zones 2 through 5 in the inverted cone where various scenarios were investigated. Examples of such scenarios are as follows: (1) zone 5 strengthened while zones 2 through 4 remained unchanged, (2) zone 5 strengthened while zone 4 remained unchanged and zones 2 and 3 weakened, and (3) zones 2 through 5 weakened. While considerable work was conducted, the most representative material property case remains unknown, and findings from modeling evaluated all material property cases collectively, resulting in few specific conclusions. Overall, modeling work by Bull and Woodford was not ideally suited for this report's objective.

2.2 Rapid-setting concrete materials

Recent ADR research efforts have relied heavily on the use of materials that set quickly and exhibit rapid strength gain. Most notably, rapid-setting concrete materials are an instrumental component in current ADR methods. These types of materials were primarily the product of two research programs, the ADR Modernization program and the Critical Runway AssessmenT and Repair (CRATR) Joint Capabilities Technology Demonstration (JCTD) program. These programs were focused on the potential for many small craters (8.5-ft diameter) rather than a few large craters (30-ft diameter). Rapid-setting concrete for capping small and large craters was one product from these programs. CRATR JCTD focused on methods to rapidly assess and repair airfield bomb damage in a base recovery after attack scenario of up to 120 small craters in an 8-hr timeframe. The CRATR JCTD included three large demos: limited operational utility assessment 1 (LOUA1), limited operational utility assessment 2 (LOUA2), and operational utility assessment (OUA). The remainder of this section briefly describes the evolution of the

development and use of rapid-setting concrete materials within these two programs.

Priddy et al. (2007) conducted laboratory and field testing that evaluated technologies for repairing small craters. Ten rapid-setting (RS) concrete materials were laboratory tested for compressive strength, bond strength, and set time. Most of these materials were also field tested in simulated craters subjected to F-15E load cart traffic. Most repairs failed by high-severity joint spalls; however, several were deemed suitable for small crater repairs. Rapid Set® Concrete Mix (further denoted RSCM) manufactured by CTS Cement was the user's choice when considering ease of use, controllable workability/set time, performance, and cure time. At the start of this work, RSCM was mixed in a 9-ft^3 portable drum mixer and placed by wheelbarrow but was eventually mixed and placed by a 2-yd^3 portable concrete mixer featuring a chute that directly deposited material into a crater.

Priddy et al. (2008) conducted more detailed laboratory testing based on ETL 08-2 testing requirements including compressive strength, bond strength, set time, elastic modulus, thermal expansion, ring shrinkage, flexural strength, and length change. RSCM, Pavemend SLQ, and Pavemend TR were tested, and RSCM satisfied the minimum protocol requirements in ETL 08-2, which lays out a testing protocol for rigid spall repair materials. Field testing was also conducted and showed that thicker RS crater caps withstood more load cart passes and that, when encountered, failure was generally due to high-severity joint spalling. As before, RSCM was the preferred RS repair material and was also mixed and placed using the 2-yd^3 portable mixer.

LOUA1 was conducted at the Silver Flag Exercise Site, Tyndall Air Force Base, FL, in August to October of 2008 (Tingle et al. 2009) to demonstrate multiple aspects of airfield damage assessment and repair that had been researched at ERDC up to this point. RSCM was used for crater capping based on previous testing (i.e., Priddy et al. 2007, Priddy et al. 2008) and performed favorably. It was mixed and placed using one of four mixers with varying configurations, one of which was CemenTech Inc.'s ABC FAST mixer, a tow-behind volumetric mixer with simplified controls, which best satisfied ADR objectives. Recommendations based on LOUA1 included the improvement of the ABC FAST mixer to further simplify its use and incorporate factory calibrations for additional materials. From

LOUA1 forward, RSCM has been the primary product used for capping craters.

Prior to LOUA1, rapid-setting flowable fill (FF) was identified as a potential crater backfill alternative to compacted soil or aggregate because of its flowable, self-leveling, and self-consolidating characteristics (Priddy et al. 2013a), although it was not demonstrated until LOUA2. Typical FFs are also referred to as controlled low-strength material (CLSM) and are designed to be excavatable (Folliard et al. 2008) and, thus, do not develop the necessary strength quickly enough to support either rigid or flexible crater caps. This led to the development of rapid-setting FF to meet ERDC objectives. Work at ERDC pertaining to FF originally spanned 2008 to 2011. Although it is not available in a citable document, this work established rapid-setting FF compressive strength requirements of 250 psi at 30 min and 750 psi at 1 day. Several vendors submitted FF products to ERDC for consideration, and, ultimately, Utility Fill 1-Step 750 manufactured by Buzzi Unicem USA Inc. (further denoted FF-BU) was recommended based on laboratory testing at ERDC.

LOUA2 was conducted at the Silver Flag Exercise Site, Tyndall Air Force Base, in April 2009 (Priddy et al. 2013a) to support the selection of two repair material and equipment packages. LOUA2 was the first demonstration of FF as a crater backfill material; FF-BU was used. It performed well when placed using the dry method for RSCM-capped craters (rigid) or the wet method for pelletized asphalt-capped craters (flexible). The dry method consisted of placing dry FF-BU directly into a crater followed by dispensing a prescribed volume of water into the crater and allowing it to percolate through the FF-BU. While this method is simpler and more efficient, it produces lower strengths and, therefore, was used only for rigid crater caps. With the wet method, FF-BU was mixed in batches in a more traditional manner using a ready-mix concrete truck and was used for flexible crater caps that required greater support. A new simplified volumetric mixer (SVM) was developed with CemenTech based on LOUA1 recommendations and demonstrated in LOUA2; it is the same as the SVM used for camouflet repairs in this report, although it was only used to mix RSCM in LOUA2. From LOUA2 forward, FF-BU has been the primary product used for backfilling craters.

OUA was conducted at Avon Park Air Force Range, FL, in August 2009 (Priddy et al. 2013b). The OUA included crater repairs with dry-placed FF-

BU backfill and RSCM caps as well as wet-placed FF-BU backfill and pelletized asphalt caps. As in LOUA2, the SVM was used to mix RSCM, while a traditional concrete truck was used to mix FF-BU. As before, these materials and methods proved successful.

Priddy et al. (2011a) details live-flight certification of CRATR technologies at Avon Park. Rigid and flexible capping systems used in conjunction with FF-BU backfill were evaluated at the conclusion of the OUA. The SVM was used for RSCM placement, and a traditional concrete truck was used to mix and place FF-BU. These systems performed well. Permanent deformation was minimal indicating sufficient load bearing capacity to support the F-15 and C-17 aircraft used for certification.

Priddy (2011) conducted additional laboratory experiments on RS materials with two main objectives. First, the laboratory selection criteria for evaluating RS concrete products was modified and refined. Several updates to ETL 08-2 specifications were recommended. Second, recommendations for suitable applications of various RS concrete materials were made. RSCM was one of four products that was suitable for all applications discussed (e.g., small crater repair, spall repair, etc.).

Following the CRATR JCTD demonstrations and flight certification of the repairs, the crater repair systems utilizing RSCM and FF-BU have been evaluated in additional scenarios. Edwards et al. (2013) conducted cold weather crater repairs at Malmstrom Air Force Base, MT, where the average temperature and wind chill during repairs were 33°F and 27°F, respectively. Note that the SVM was described therein as capable of mixing FF; however, FF-BU was still placed via the dry method for the rigid repairs in this project. Bell et al. (2013) conducted wet weather crater repairs at the Silver Flag Exercise Site, Tyndall Air Force Base. Note that the SVM was used to mix and place FF-BU as the backfill for flexible crater caps in this project. Carruth et al. (2015) evaluated the ability of the FF-BU backfill and RSCM cap system, which was developed for small craters, to repair large craters.

Carruth and Howard (2016) evaluated the suitability of wet-placed FF-BU as a crater-capping material. Several cases were tested where FF-BU was placed full depth or where it was used as a cap over an aggregate backfill. Several thicknesses and crater diameters were tested. Cores taken from the repairs and tested at 28 days exhibited 1,273 to 2,337 psi compressive

strength, depending primarily on the water-to-solids (*w/s*) ratio. Prior to Carruth and Howard (2016), field compressive strengths are only documented for RSCM; strengths for FF-BU were reported as in-situ California Bearing Ratio (CBR) values. Load cart trafficking results of repairs were favorable.

While there is no citable document as of the date of this report, additional laboratory material characterization of FF-BU has been conducted at ERDC, and a technical report documenting the results is forthcoming. This testing subjected FF-BU to the suite of tests described in ETL 08-2, similar to the testing of RSCM and other RS concrete materials conducted by Priddy (2011).

Much of the work presented in the technical reports referenced in this section was also published in peer-review journals (Priddy et al. 2009, Griffin and Brown 2011, and Priddy and Rushing 2012). In favor of the technical reports, journal references were not explicitly discussed though the references are provided for convenience.

2.3 Rigid polyurethane foam materials

Similarly to the rapid-setting cementitious materials, rigid polyurethane foam materials (simply referred to herein as foam) have been studied for use as a crater backfill material within the overall ADR program and were included in multiple full-scale demonstrations (e.g., LOUA1, LOUA2, and OUA). These are generally two-part systems (component A, isocyanate component, and component B, polyol component) that react when mixed to expand in volume and then set to form a rigid material capable of supporting loads. Priddy and Hodo (2009) is a fairly comprehensive literature review of polyurethane foams; full details on the basic characteristics of polyurethane foams can be found therein. The remainder of this section briefly describes the evolution of the development and use of foam materials for ADR purposes.

Priddy et al. (2007), in addition to evaluating rapid-setting concrete materials as discussed in Section 2.2, evaluated 10 foam materials for crater backfill. Properties evaluated in the laboratory included unconfined compressive strength (UCS), tensile strength, density, rise time, set time, and expansion ratio. Some of the basic foam characteristics were first documented. For example, density and expansion are inversely related, and reasonable compressive strengths (e.g., 200 psi, 300 psi) relative to

compacted aggregate backfill were achievable. Some foam materials were used to backfill simulated craters. Materials were generally mixed in large buckets with electric drills and paddle mixer attachments. Extending foam using limestone aggregate was also considered. In general, foam performed reasonably under load cart traffic when no major issues were encountered with placement. Generally, however, issues were encountered with materials either reacting too quickly or exhibiting high sensitivity to any moisture present (excessive expansion and significant strength loss).

Priddy et al. (2008) continued the research initiated in Priddy et al. (2007) and recommended Foam-iT! 10 or Foam-iT! 15 manufactured by Smooth-On Inc. for small crater backfill. The development of dispensing equipment was also recommended since producing individual batches of foam by hand mixing in buckets was time consuming and typically produced non-uniform backfill surfaces due to each batch of foam reacting at varying times.

Priddy (2009) conducted a field evaluation of the Navy's ADR injectable foam concept that used Uretek/EagleLIFT USA's expeditionary injectable foam dispensing system to inject Uretek 486 Star 6-lb polyurethane foam underneath concrete crater caps that were initially backfilled with crater debris. Repairs exceeded the Navy's 200-pass expedient requirement, typically failing after 1,400 passes of an F-15E load cart. Findings showed that injecting foam into debris backfill with significant amounts of high-quality concrete was not of meaningful benefit relative to debris backfill with no foam (i.e., the foam was an added, unnecessary expense).

LOUA1 conducted foam backfill testing (under RSCM caps); Foam-iT! 10 was used as it was recommended in Priddy et al. (2008). It was dispensed using the ESCO Model B-100 prototype that had insufficient output rate (needed to be increased by 500%) and had to be periodically flushed with solvent to avoid clogs. This, coupled with the short reaction time (approximately 1.5-min pot life) and moisture sensitivity of Foam-iT! 10, made effective and efficient placement of the foam difficult. However, where foam was able to be successfully placed, it performed relatively well under load cart traffic. Given the numerous difficulties experienced, dispenser modifications were recommended, and a set of required foam specifications were drafted as follows:

- Minimum expanded density of 10-15 pcf,
- Minimum UCS of 300 psi at 2% strain,
- Insensitive to water and moisture,
- Expansion ratio of 4-10 by volume,
- Minimum reaction time of 5-10 min to 15-20 min maximum,
- Tack-free time of 15-20 min,
- Maximum cure time of 1 hr, and
- Minimum shelf life of 3 years.

Based on LOUA1 results, Priddy et al. (2010b) sought to identify a new foam material for use with a foam dispenser to be showcased in LOUA2. Additional foam products were tested including Foam-iT! 10 SLOW (FI-10S), which was a reformulated version of Foam-iT! 10 designed to have a longer reaction time (approximately 4 min). In addition to laboratory testing in Priddy et al. (2007), testing for moisture sensitivity was conducted. Cylinders were fabricated by pouring foam into concrete molds that contained standing water, moist soil, and plastic sheeting over moist soil. Results were poor in all cases; standing water yielded a 96% UCS decrease, moist soil yielded a 60% UCS decrease, and the plastic sheeting was uplifted and absorbed into the foam, creating a slip plane within the foam cylinder and also allowing foam to reach and react with the moist soil. From laboratory testing, FI-10S was preferred based on UCS (average 282 psi UCS when targeting 300 psi). Field testing confirmed FI-10S's moisture sensitivity; as a result, the spreading dry FF or cement along the sides and bottom of a crater to absorb moisture prior to placing foam was recommended.

Priddy et al. (2010b) also evaluated two foam dispensers. The first was the ESCO B-100 modified to use a static mixhead; however, this did not meet the desired output rate. The second was a new ESCO dispenser that was referred to as prototype 2. It still required periodic flushing but was able to dispense foam at 100 to 1,000 lb/min, a considerable improvement. Concerns regarding mechanical problems and inconsistent performance of the dispensers were presented (some of them based on testing conducted at ERDC after LOUA2), and further modifications were recommended.

LOUA2 (Priddy et al. 2013a) conducted foam backfill testing utilizing FI-10S and the ESCO prototype 2 dispenser used in Priddy et al. (2010b) with no additional modifications. Overall, the dispenser performed relatively well; however, further modifications were recommended to eliminate the

need for separate flushing systems. Regarding the FI-10S material, it was stated that consistency, quality, and strengths achieved did not measure up to those obtained in prior field testing. Moisture sensitivity remained a concern, albeit less of one once FF was used to absorb moisture. Trafficking results indicated foam backfill was suitable for 100 to 2,000 F-15E load cart passes but may not be able to support more than 100 C-17 load cart passes. No repair withstood the minimum passes of 112 initial (1,800 final) of the F-15E load cart plus 500 of the C-17 load cart. Overall, repairs backfilled with foam did not perform as well as those backfilled with FF-BU. Ultimately, foam backfill was not recommended for the OUA; rather, it was recommended that additional equipment and material investigations be conducted.

Kyzar et al. (2010) conducted a field evaluation of the Navy's prototype foam dispenser for repairing threat munition craters. This dispenser was an ESCO dispenser that had gone through several design iterations under the ADR Modernization and CRATR programs (not ESCO prototype 2). Of pertinence to this report, FI-10S was used for the repairs, and it was observed that the material must be maintained between 65 and 85°F to use the dispenser. Hand mixing was necessary between 50 and 65°F or 85 and 90°F. Overall, repairs withstood 50,000 passes of a 20,000-lb dual tandem gear configuration simulating truck traffic using the Heavy Vehicle Simulator (HVS) with only low-severity distresses.

Although not officially included in the OUA, several foam-backfilled craters were prepared after the initial OUA troop demonstration. Live flight certification of deployable crater repair technologies (i.e., foam, fiber-reinforced polymer (FRP) matting) is documented in Priddy et al. (2011b). The ESCO prototype 2 dispenser was utilized to place FI-10S but repeatedly malfunctioned and was ultimately abandoned in favor of hand mixing in 18-gal buckets. Ten gallons per batch were mixed for 1 min with an electric mixer and paddle attachment. All of the four craters repaired using foam backfill withstood over 100 passes of combined F-15 and C-17 traffic, and two could have withstood much more before needing permanent repair. Overall, the foam backfill proof of concept was validated.

Continued research has been taking place at ERDC to further refine foam backfill technologies. Gurtowski et al. (2016) conducted a laboratory evaluation of additional foam products and is phase 1 of a two-phase

project, with phase 2 consisting of a field evaluation of new prototype foam dispensers. Key findings from the laboratory study were (1) that FI-10S remained one of the most favorably performing materials when all factors are considered, and (2) that a second product, Primal Innovations Medium, provided equivalent or better laboratory properties. HMI's RR601 foam was also among the products tested in Gurtowski et al. (2016), which is worth noting since HMI products were tested in this project as described later.

Much of the work presented in the technical reports referenced in this section has also been published in peer-review journals (Priddy and Newman 2010, Priddy et al. 2010a, and Priddy et al. 2016). In favor of the technical reports, journal references were not explicitly discussed although the references are provided for convenience.

3 Experimental Program

3.1 Materials tested

3.1.1 Rapid-setting flowable fill

Flowable fill is a highly fluid mixture of cement, fine aggregate, and water and is often used for backfilling utility cuts or other applications where flowable, self-leveling, and self-consolidating materials are advantageous. Rapid-setting flowable fills use rapid-setting cements to quickly obtain sufficient bearing capacity in expedient ADR scenarios. Two rapid-setting flowable fills were tested in this project.

The first RS FF was Buzzi Unicem Utility Fill 1-Step 750 (FF-BU), which, with respect to pre-blended RS FF materials used for ADR purposes, has been utilized exclusively since it was first recommended for use in LOUA2 as described in Section 2.2. FF-BU was acquired in 50-lb buckets for laboratory testing or 3,000-lb supersacks (approximately 1 yd^3) for full-scale field testing.

The second RS FF was CTS Flowable Fill (Mil. Spec.) (denoted FF-CTS herein) manufactured by the CTS Cement Manufacturing Corporation specifically for the work in this project. The vendor was asked to formulate a flowable fill product adhering to military specification MIL-DTL-32527 that details requirements for rapid-setting flowable fill backfill materials; performance specifications are shown in Table 3.1. FF-CTS was pre-blended by the vendor and also acquired in buckets and supersacks.

Table 3.1. MIL-DTL-32527 flowable fill performance specifications.

Test	Test Method	Placement Method	Criteria
Compressive Strength	ASTM D4832	Wet	≥ 750 psi at 28 days
		Dry	≥ 500 psi at 28 days
Initial Hardening	ASTM D6024/D6024M	n/a	≤ 30 minutes
Segregation	ASTM C1610/C1610M	Wet	< 5%
Linear Shrinkage	ASTM C426	Wet	< 2%

3.1.2 Rapid-setting concrete

CTS Rapid Set® Concrete Mix (RSCM) is a proprietary, pre-blended, rapid-setting concrete material, which, with respect to concrete materials used for ADR purposes, has been utilized essentially exclusively since it

was first recommended for use and demonstrated in LOUA1. Desirable attributes of RSCM in the context of ADR are its fast set time (10 to 20 min) and its high early strength and load carrying capacity after only 2 hr of curing. RSCM contains CTS's proprietary Rapid Set® Cement as well as 3/8-in. maximum size pea gravel. Military specification MIL-DTL-32526 governs requirements for rapid-setting concrete capping materials. It is similar to spall repair material specification ETL 08-2 but incorporates recommended changes from Priddy (2011) as discussed in Section 2.2. RSCM was acquired in buckets or supersacks depending on the use.

3.1.3 Polyurethane foam

Polyurethane foam is a product of the reaction of isocyanate (component A) and polyol (component B) that yields a rigid material capable of supporting load. Component B, in addition to polyol, contains catalysts, blowing agents, and other additives that control variables such as pot life, reaction speed, and expansion ratio. The blowing agent (most commonly water) in component B reacts with component A to release CO_2 gas that disperses through the material creating the cellular structure present in foams. Because the blowing agent is typically water, the presence of additional water will uncontrollably affect the reaction and is the reason most foam products are moisture sensitive. Three foam products were tested in this project.

The first foam was Smooth-On Foam-iT! 10 SLOW (FI-10S), which, as discussed in Section 2.3, has been the predominant product of choice for ADR foam backfilling. It is a water-blown foam designed to expand approximately 6 times its initial volume and yield a final density of approximately 10 pcf. FI-10S is the reformulation of Foam-iT! 10 designed to provide a relatively slow reaction rate to facilitate large-pour operations. FI-10S was acquired in 1-gal containers for laboratory testing or 250-gal plastic totes for full-scale field testing.

The second and third foams, RR401 and RR401G, were manufactured by HMI Inc. These were tested primarily to investigate the moisture insensitivity of RR401G, which is marketed as a gas-blown foam rather than a water-blown foam and should, therefore, be unaffected by the presence of moisture. Note that this was of interest to this project since spreading cement to absorb moisture would not be as effective for camouflets since access to the entire void would be limited to the OPE. Both foams are designed to yield a final density of approximately 4 pcf. At

the time of this report, HMI did not offer a 10-pcf gas-blown foam. Therefore, RR401 was tested as the water-blown control for comparison with RR401G since comparisons between RR401G and FI-10S would not be appropriate due to the density differences (strength and density are correlated). If the gas-blown foam did in fact prove to be moisture insensitive, the intent was to then work with HMI to produce a gas-blown 10-pcf foam for direct comparison to FI-10S. Ultimately, RR401 and RR401G were tested only in the laboratory; batches of each were supplied by HMI in 5-gal containers.

3.2 Laboratory material characterization

3.2.1 Cementitious materials

Various laboratory properties of the cementitious materials tested in this project were obtained for baseline references in a controlled environment for purposes of comparing one material to another. Full laboratory characterizations have been previously conducted for RSCM and FF-BU as they were fairly comprehensively evaluated at ERDC prior to this project. Therefore, these materials were not laboratory tested in this project; instead, results from tests specified in MIL-DTL-32536 and provided in other reports are referenced where useful. For RSCM, which was evaluated approximately five years prior to this report in Priddy (2011), this approach was not expected to be the most reliable since numerous factors could lead to the RSCM used in this report differing from that tested in Priddy (2011) (e.g., plant production inconsistencies over time). This approach was considered less of a concern for FF-BU since its laboratory characterization largely took place within the same year as that of FF-CTS. Full findings from the FF-BU study will be published in a forthcoming technical report as discussed in Section 2.2; pertinent FF-BU findings for initial comparison to FF-CTS are provided in this report.

In Priddy (2011), RSCM was mixed according to the manufacturer's recommendations. In the FF-BU study, it was mixed according to manufacturer's recommendations to one of two *w/s* ratios: 0.11 or 0.21. These *w/s* ratios were chosen to represent the dry and wet placement methods, respectively, and were calculated by proportionally scaling down full-scale material quantities to laboratory-scale batch quantities.

FF-CTS laboratory characterization was conducted by the Concrete and Materials Branch (CMB) at ERDC's Materials Testing Center (MTC),

similar to the testing of RSCM and FF-BU. Table 3.2provides a summary of the tests conducted. In all, 42 strength specimens were produced and tested, and 24 basic control parameter tests were performed. Initially, FF-CTS was to be tested at *w/s* ratios of 0.11 and 0.21 similar to FF-BU; however, preliminary testing suggested FF-CTS would be too dry to cast cylinders at the 0.11 *w/s* ratio. Ultimately, *w/s* ratios of 0.21 and 0.25 were selected, which produced relatively similar consistencies to FF-BU at *w/s* ratios of 0.11 and 0.21, respectively.

Table 3.2. Laboratory characterization test plan for FF-CTS.

Test	Test Method	*w/s* Ratio	Cure Time	Replicates	Total
Compressive Strength	ASTM C39	0.21, 0.25	1 hr, 2 hr, 1 d, 28 d	3	24
Flexural Strength	ASTM C78	0.21, 0.25	2 hr, 1 d, 28 d	3	18
Flow Consistency	ASTM D6103	0.21, 0.25	n/a	3	6
Density	ASTM D6023	0.21, 0.25	n/a	3	6
Air Content	ASTM C231	0.21, 0.25	n/a	3	6
Set Time (Penetrometer Resistance)	ASTM C403	0.21, 0.25	n/a	3	6

– 4 by 8 in. cylinders tested for compressive strength; 6 by 6 by 18 in. beams tested for flexural strength
– Strength specimens were cured the prescribed cure time in a near 100% humidity moisture room at 73.5 ± 3.5°F
– Flow consistency measured using a 3 by 6 in. cylinder open on both ends and performed similar to slump tests

FF-CTS was mixed identically to FF-BU. One batch was produced at a time using an entire 50-lb bucket of dry FF-CTS. Mixing was performed at 73°F and 50% relative humidity in an aluminum container using a dual paddle mixer. Prior to water addition, the dry material was mixed briefly to counter segregation that may have occurred during handling. Water was added slowly, and once all water was added, it was mixed for 3 min. Immediately after mixing, the material was tested or used to cast specimens. Specimens were tested at a range of cure times as shown in Table 3.2. Figure 3.1 shows an example of a cylinder tested for compressive strength.

Figure 3.1. Tested compressive strength cylinder.

3.2.2 Foam materials

Laboratory characterization of foam materials was conducted primarily to evaluate the moisture sensitivity of HMI RR401G in considering gas-blown foams as a potential replacement for FI-10S for camouflet repairs. Similar to RSCM and FF-BU discussed previously in Section 3.2.1, FI-10S has been previously evaluated at ERDC, and results are presented in Gurtowski et al. (2016). Testing of FI-10S was not repeated in this project since the FI-10S testing occurred around the same timeframe as this project; rather, FI-10S results are referenced where useful. Recall that since direct comparisons between RR401G and FI-10S could not be made due to differences in density (and thus strength), RR401 was also tested as the control for RR401G.

Table 3.3 illustrates the foam test plan, which, in this report, included only UCS testing under various conditions to evaluate moisture sensitivity. Three cases (dry, damp, and wet) were considered as shown in Table 3.3. In all, 18 specimens were tested for UCS.

Table 3.3. Laboratory characterization test plan for foam.

Test	Test Method	Cure Time	Foam	Condition	Replicates
Compressive Strength at 2% Strain	ASTM D1621	~1 d	RR401	Dry	3
				Damp	3
				Wet	3
			RR401G	Dry	3
				Damp	3
				Wet	3

– Cure times were overnight, corresponding to approximately 18 to 24 hr
– Damp indicates foam was poured into cylinder mold containing ~1/2 in. moist sand
– Wet indicates foam was poured into cylinder mold containing ~1/2 in. plain water

Gurtowski et al. (2016) provides full details of specimen preparation and testing procedures. Pertinent details are provided in this report. Specimens were cast individually in 4- by 8-in. plastic concrete cylinder molds that were sprayed with Stoner Release & Paint™, a release agent, to facilitate later specimen removal. First, components A and B of a given foam product were agitated separately to ensure each was well-mixed. The appropriate weight of component B was batched into a 1-qt steel paint can with the rim removed (Figure 3.2a). This was set on a scale and tared, and then component A was batched directly into the paint can. Batch weights were determined based on densities of each component and calculated to yield a 1:1 ratio of components A and B by volume. For the dry cases, 229 g

component A and 205 g component B were used per batch. For the damp and wet cases, batch weights were reduced to 123 g component A and 110 g component B since expansion of the foam increased considerably in the presence of moisture.

Immediately, this material was mixed at a high rate using a pneumatic mixer with an impeller-style mixing paddle attachment as shown in Figure 3.2b to 3.2d. Mixing times varied by material. For example, FI-10S in Gurtowski et al. (2016) was mixed for 30 sec, which was the standard mixing time. However, RR401 and RR401G were not slow-reacting formulations and would begin reacting in the mixing container within 30 sec. Therefore, the HMI products were mixed for 7 sec. The mixture was immediately poured into a single plastic cylinder and allowed to react as shown in Figure 3.2e. Specimens remained in the cylinder molds until they were ready to be prepared for strength testing.

Figure 3.2. Foam specimen production photographs.

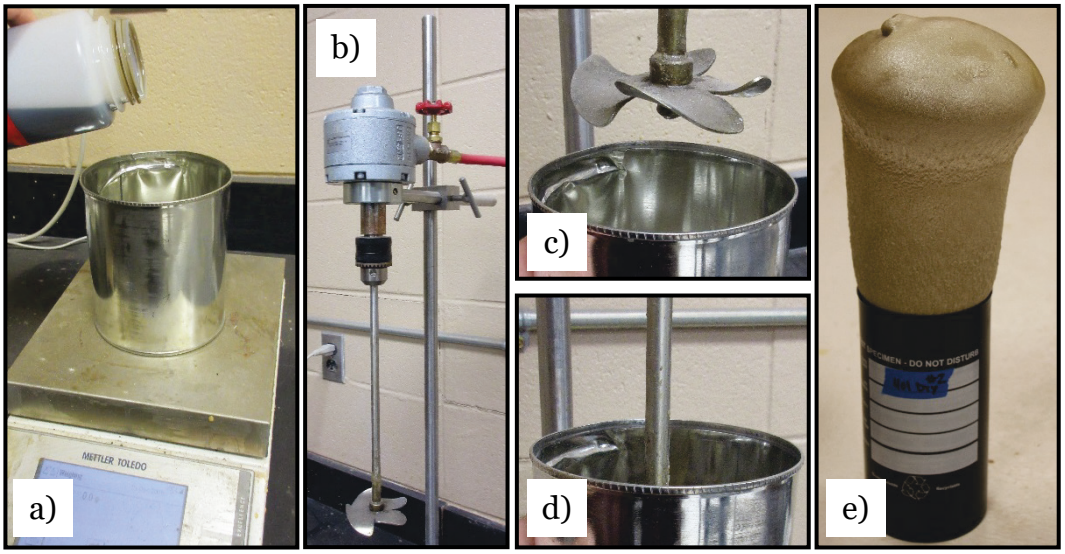

After curing overnight, specimens were removed from the molds and cut for testing. One 4- by 4-in. test specimen was cut with a miter saw or band saw from each cylinder approximately 2 in. from the bottom of the specimen (i.e., the middle 4 in. of the 8-in.-tall cylinder). This section was typically the most homogeneous section of the specimen and, therefore, would be the best-case scenario in terms of strength. Actual specimen dimensions were obtained with calipers and used to calculate UCS.

UCS testing was conducted on an Instron electromechanical load frame with a 60,000-lb capacity using a 10,000-lb load cell. A simple test

program was written in the Blue Hill 3.0 software that applied a static loading of 0.1 in. per min and automatically calculated UCS at 2% strain. UCS at 2% strain was established based on Priddy et al. (2007); 2% strain was the maximum expected strain in the field for foam under a loaded concrete crater cap. Figure 3.3 shows photographs of a foam test specimen in the UCS setup and during testing.

Figure 3.3. Foam specimen: a) UCS setup, and b) during UCS test.

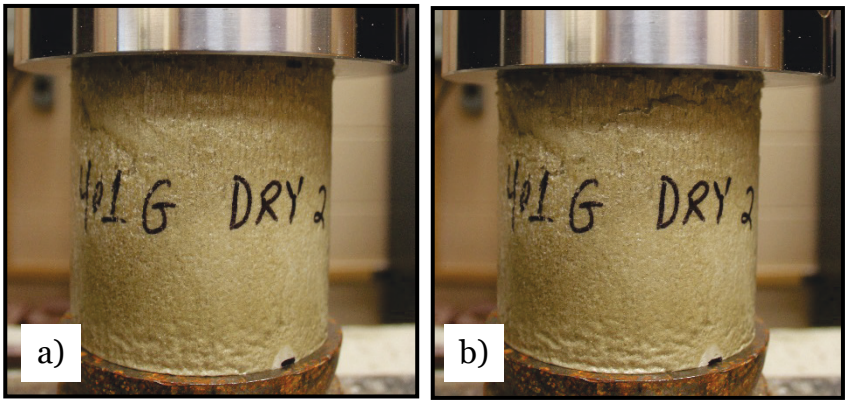

3.3 Void characterization

Multiple approaches to characterize a camouflet void were evaluated, ranging from techniques that were advanced and expensive but provided more comprehensive data to techniques that were simple and cheap but provided less data. Void characterization focused primarily on determining the size and shape of the void and was conducted for two purposes. First, void characterization was performed for research purposes since relatively little is known about camouflet characteristics. For example, it has generally been assumed in the past that camouflets are relatively spherical, but documentation of exact shapes is not readily available. Second, knowing camouflet volumes is useful for estimating repair material quantities. Table 3.4 provides a list of all the techniques considered; each is discussed in more detail in the following sections.

A model camouflet was built in the laboratory to conduct a preliminary evaluation of Table 3.4 techniques as well as to refine data collection procedures prior to collecting actual data at the Silver Flag Exercise Site. In addition, a single camouflet at Silver Flag was intended for destructive void characterization (i.e., saw-cut and remove the overlying slab). Details regarding construction of the model camouflet and the destructive void characterization are provided in the following sections.

Table 3.4. Camouflet void characterization techniques considered.

Technique	Approx. Cost ($)	Data Output Type	Volume Calculation
Cavity Auto Laser Scanner (C-ALS®)	$75,000	Visual, 3-D Scan, Volume	Direct - Continuous
MC1 Borescope	$10,000	Visual	Direct - Continuous
Subsea Video Systems Camera	$10,000	Visual	Direct - Continuous
Modified Laser Range Finder (MLRF)	$1,000	Diameter, Depth	Direct - Discrete
Uniprise Flexible Tubing	$100	Diameter, Depth	Direct - Discrete
Loc-Line Tubing	$100	Diameter, Depth	Direct - Discrete
Plumb Bob	$10	Depth	Indirect (e.g., correlations)

-- The C-ALS provides an instant 3-D scan with low to high resolution (determined by user) and its software can instantly calculate volume
-- The MC1 borescope and Subsea Video Systems camera could be used with third party photogrammetry software to construct a 3-D point cloud and calculate volume
-- The MLRF can provide multiple point measurements of diameter and depth; volume can be directly calculated using equations
-- The Uniprise flexible tubing and Loc-line tubing can provide multiple point diameter and depth measurements but with less reliability; volume can be directly calculated using equations
-- The plumb bob can provide depth; volume can be indirectly calculated using assumptions (e.g., void is spherical)

3.3.1 Cavity auto laser scanner

The Cavity Auto Laser Scanner (C-ALS®), shown in Figure 3.4, is manufactured by Renishaw, PLC. It is used primarily in the mining industry for mapping inaccessible portions of mines safely and quickly. At a diameter of 2 in., it can be deployed through narrow mineshafts over 100 ft long. A camera in the C-ALS nose cone is used to visually determine when the probe has reached the cavity. Once fully deployed into the cavity, the head swivels to collect a 360° laser scan of the cavity. Data are fed via a cable to a data acquisition unit above ground and then to a computer where it is processed and displayed in real time on the C-ALS software graphical interface. Key specifications are provided in Table 3.5.

Figure 3.4. C-ALS equipment overview.

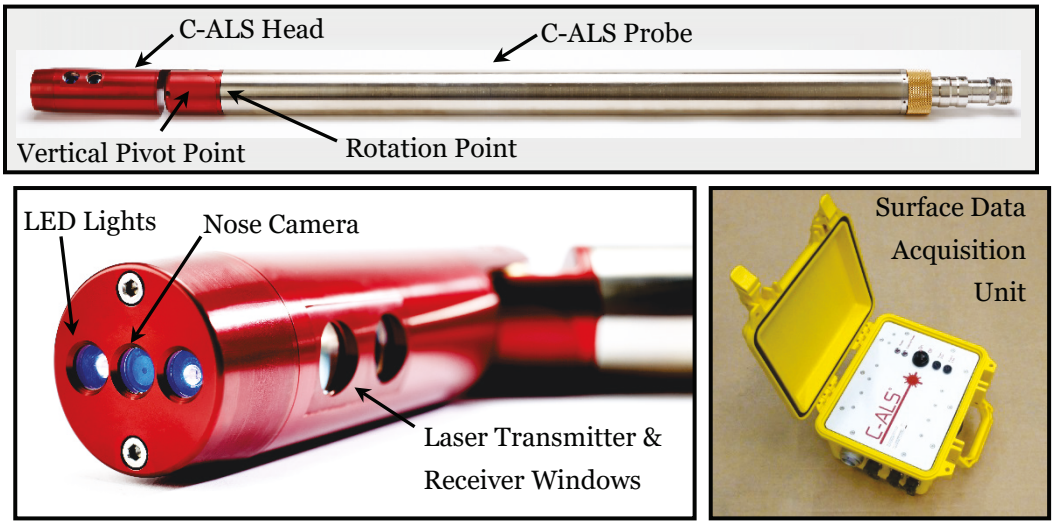

Table 3.5. C-ALS published specifications.

Laser	
Laser Classification & Type	Class 1 – InGaAs laser diode
Wavelength (typical)	905 nm
Resolution (i.e., Distance Accuracy)	0.4 in.
Range	1.6 to 490 ft
Angle Measurement	
Accuracy	0.2°
Range (Vertical)	-90° to 90°
Range (Horizontal)	0° to 360°
Motion	Two-axis servo-driven gear w/ manual clutch override
Physical	
Construction	Machined aluminum and stainless steel
Water and Dust Resistance	IP67
Dimensions: Case for C-ALS and Accessories	15.5 in. depth × 15.0 in. height × 56.0 in. length
Dimensions: C-ALS Probe	2 in. dia. × 3.6 ft length
Dimensions: C-ALS Probe with Ext. Rod	2 in. dia. × 7.1 ft length
Dimensions: Surface Data Acquisition Unit	10.6 in. width × 9.6 in. depth × 6.7 in. height
Weight: Probe	13.0 lb
Weight: Probe with Ext. Rod	19.6 lb
Weight: Surface Data Acquisition Unit	9.0 lb
External Power Input	12 to 15 V DC (rechargeable battery pack or deep cycle battery) or 110 to 240 V AC (requires clean power; generator not acceptable)
Power Consumption During Scan	0.8 to 2.0 A

– *Generators cannot directly power C-ALS because generators produce square-waveform power; however, generators can be used to keep battery pack charged*

The C-ALS Cavity Profiler software is free and can be installed on any computer, connecting to the data acquisition unit via an Ethernet cable or a WiFi connection. The software controls the C-ALS scan functions, provides a video feed from the C-ALS nose camera, displays scan data in a 3-D point cloud format, can edit collected data, conducts volume calculations, and can output data in various formats for use in third-party software. Figure 3.5 provides a screen shot of the software with an example data file provided by Renishaw. Each individual scan layer can be turned on or off for viewing.

Both horizontal and vertical scans can be conducted. For horizontal scans, the C-ALS head pivots to a fixed angle (-90° to 90°) for each scan sweep (angle increments are determined by the user-defined scan resolution) and then rotates around the axis of the probe from 0° to 360° (i.e., one scan sweep produces a horizontal ring). For vertical scans, the C-ALS head rotates around the probe axis to a fixed position (0° to 360°) for each scan sweep (position increments are determined by the user-defined scan resolution) and then pivots from -90° to 90° (i.e., one scan sweep produces a vertical ring).

Figure 3.5. C-ALS Cavity Profiler software graphical interface.

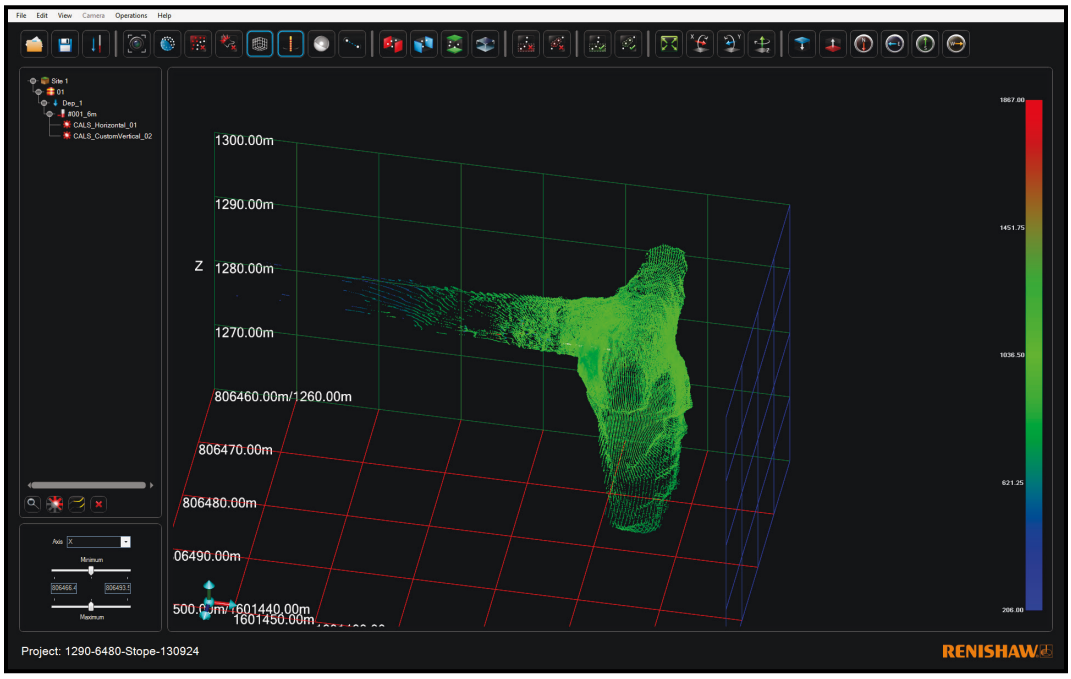

Volume calculations are very straightforward as shown in Figure 3.6. A scan is selected, then the “Create Surface” button is selected, and the software creates a triangulated surface from the point cloud and displays a volume. Time to perform this calculation and obtain a volume is measured in seconds.

Figure 3.6. C-ALS Cavity Profiler software showing calculated surface and volume.

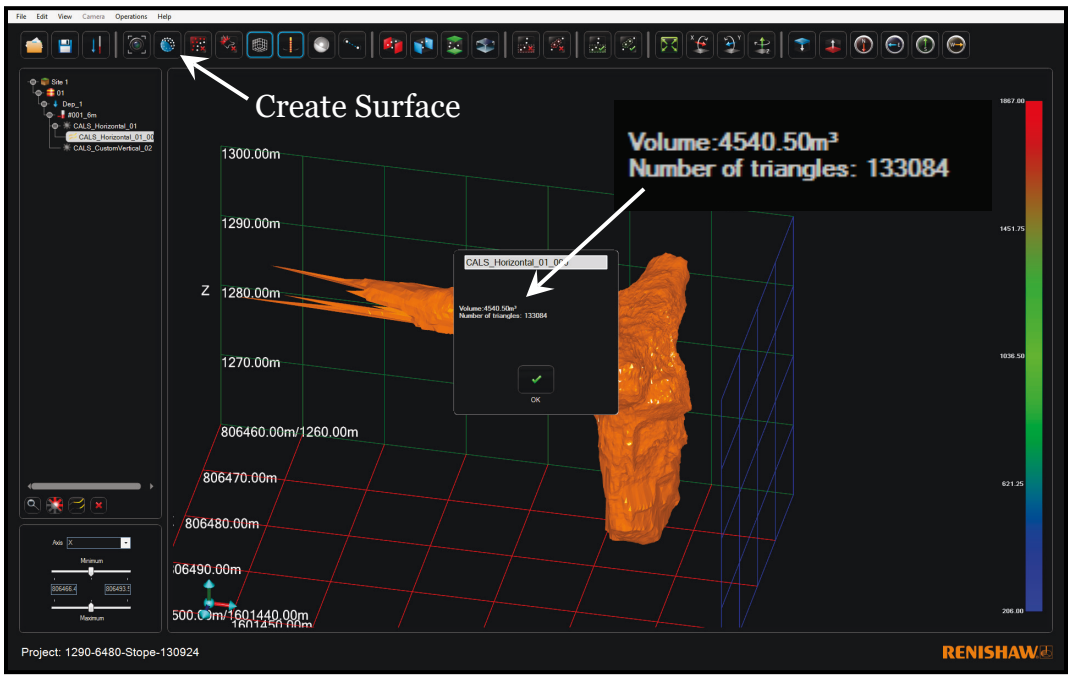

For this project, Renishaw traveled to Silver Flag and performed a training demonstration with ERDC engineers, who were allowed to keep data collected during this time. Since this application differed from that of the mining industry, Renishaw constructed a custom support frame for deploying the C-ALS into camouflets at Silver Flag (note that no testing was conducted in the laboratory with the C-ALS system). Figure 3.7 shows the frame that consisted of a standard survey tripod mounted on a fabricated dolly. The dolly was fitted with locking casters to make transporting the C-ALS from one camouflet to another relatively easy. In use, the C-ALS is inserted through the center opening at the top of the tripod and then through the spring-loaded rollers shown in Figure 3.7. Once the C-ALS is deployed to the desired depth, a clamp is placed on the C-ALS itself directly above the tripod's top plate to hold the C-ALS at that position.

Figure 3.7. C-ALS support frame for camouflet deployments.

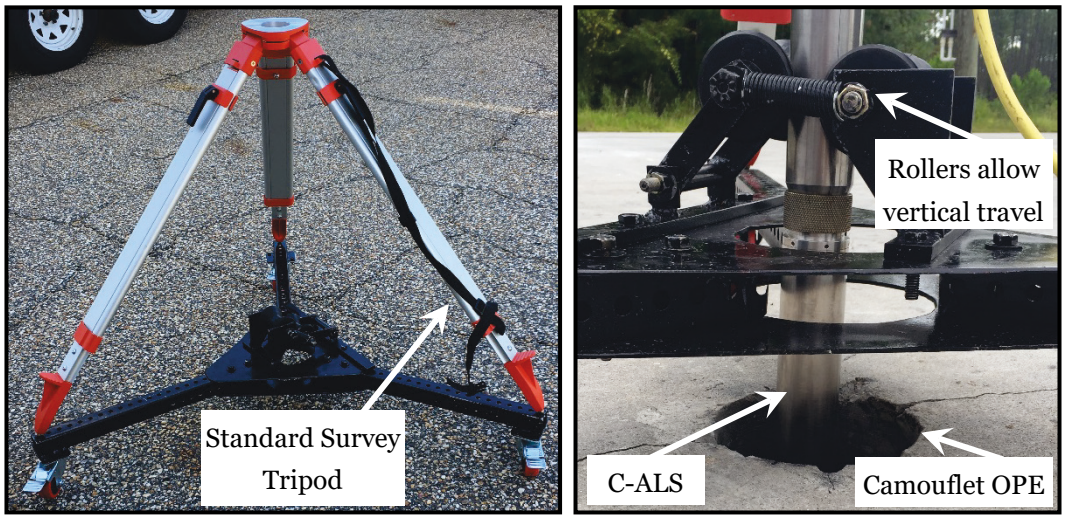

Figure 3.8 demonstrates the typical deployment procedure of inserting the C-ALS into the support frame and then the camouflet. When moving from one camouflet to the next, it was not necessary to completely withdraw the C-ALS from the support frame; it could be raised so that there was clearance between the C-ALS head and pavement surface. Figure 3.8 also shows the extension rod attached to the C-ALS, the 13-ft data cable, the data acquisition unit, the battery pack, and the data collection computer.

Figure 3.8. C-ALS deployment and setup during scans.

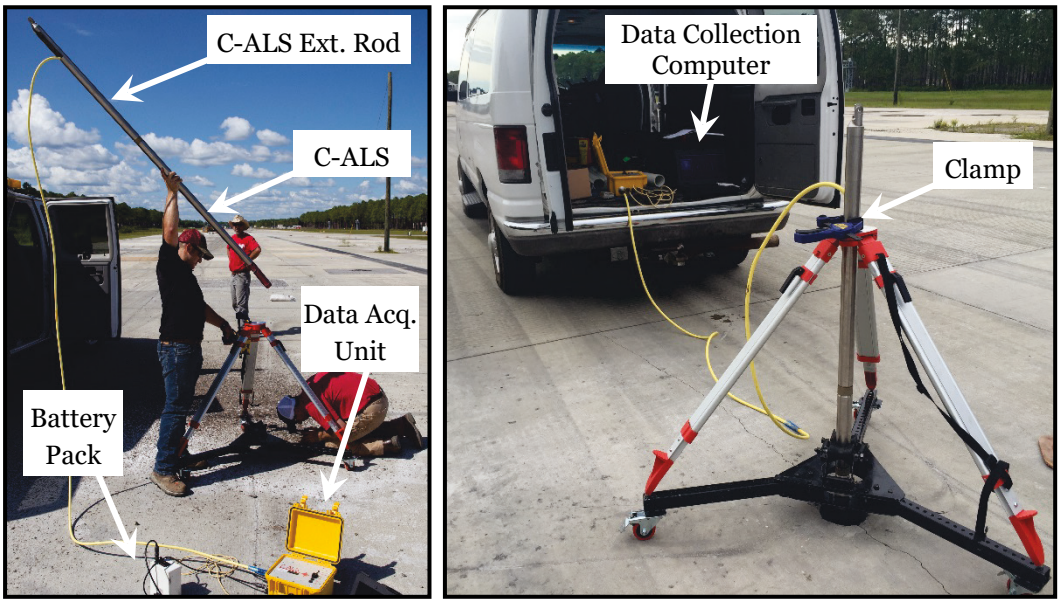

The video feed from the C-ALS camera is used as a guide in setting the C-ALS depth as shown in Figure 3.9. The operator monitors the video as the C-ALS is deployed and looks for the breakout point, the point at which the C-ALS nose enters the cavity. From that point, the C-ALS is lowered approximately 12 in. further to ensure the head has unobstructed clearance to freely rotate and pivot.

Once an initial C-ALS depth is set, a ring scan is conducted. During the ring scan, the head rotates 360° but does not pivot. This scan is displayed on the computer showing the amount of clearance around the C-ALS head. For example, if the C-ALS head was still located within the camouflet shaft, the ring scan would be approximately 0.5-ft diameter, and the operator would know the C-ALS must be lowered further. In contrast, if the ring scan diameter was approximately 1 ft or greater, the operator could begin conducting scans of the cavity. If the C-ALS is lowered, this process is repeated. Each ring scan requires approximately 5 sec.

Figure 3.9. Still images from C-ALS video during deployment.

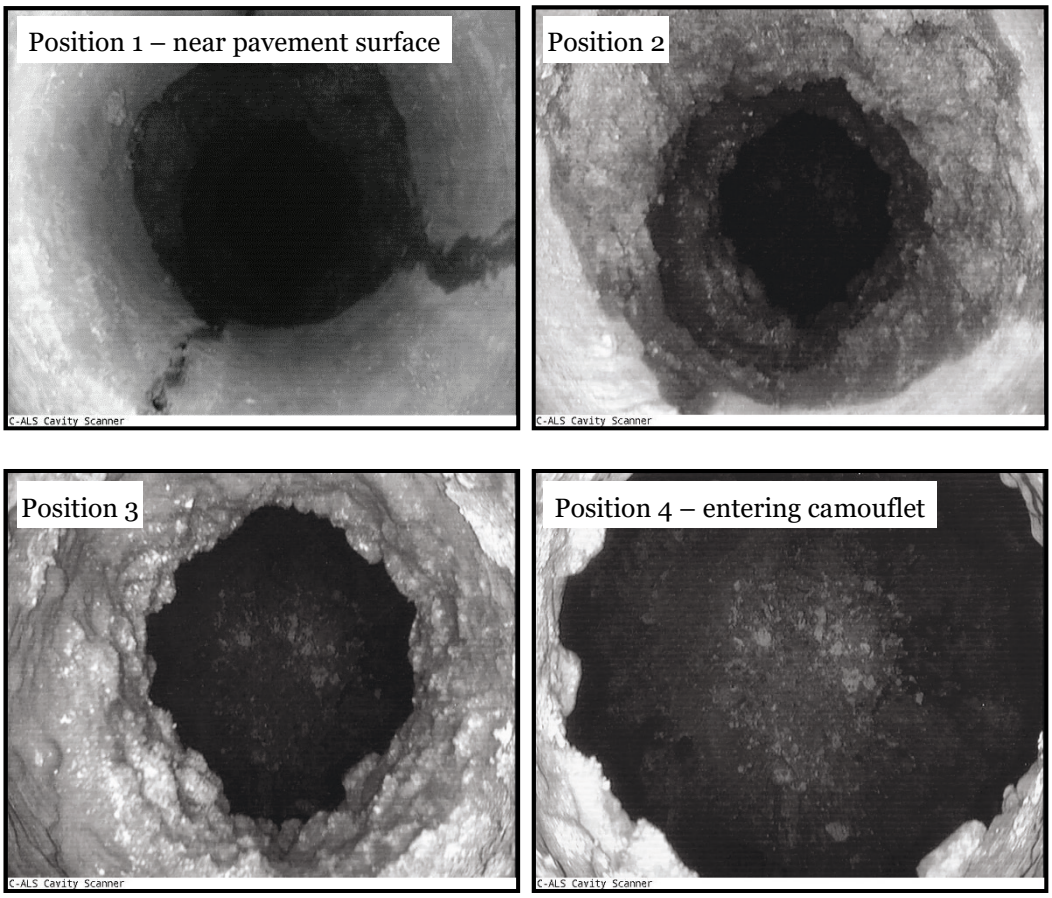

Once the C-ALS is fully positioned, the operator inputs the scan type (vertical or horizontal) and scan resolution, and then commands the C-ALS to begin scanning. The default scan resolution used in this project was 3°. For two camouflets, scan resolution angles of 1, 3, 5, 10, 20, and 25° were conducted as well as timed in order to investigate the tradeoff between calculated volume accuracy and scan time.

3.3.2 MC1 borescope

The MC1 borescope, shown in Figure 3.10 , that was manufactured by SPI Borescopes and rented for this project was investigated as a means of visually inspecting camouflet voids. In addition, using photographs and videos taken by the device to perform photogrammetry tasks was considered. This would allow a 3-D point cloud to be constructed and used for volume determination. Table 3.6 provides key specifications of the MC1. The MC1 was tested both in the laboratory camouflet model and full-scale Camouflets 1 and 12 at Silver Flag.

Figure 3.10. MC1 borescope photographs.

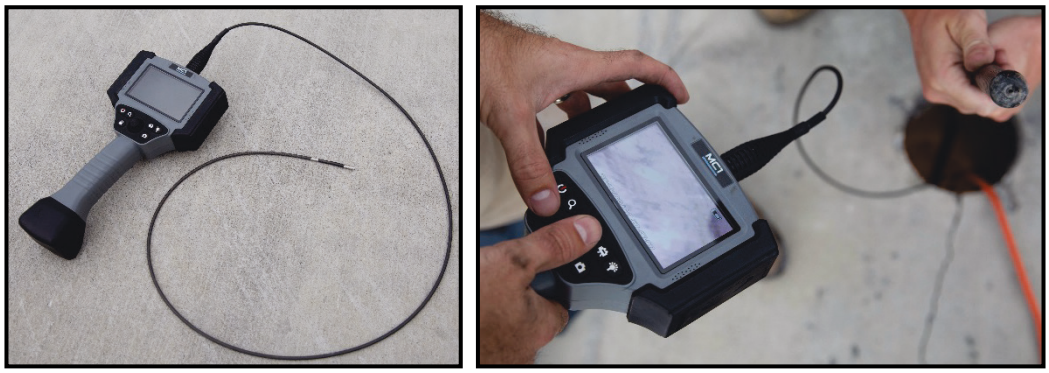

Table 3.6. MC1 borescope specifications.

Camera	
Material	Stainless steel, titanium alloys
Water Resistance	IP65
Illumination	6 Ultra-White Light LEDs
Brightness Adjustment	Off to High (5 Brightness Levels)
Still Image Format	JPEG; 1024 × 768 pixels
Video Format	AVI; 720 × 576 pixels at 30 fps
Field of View	> 90°
Zoom	1x to 3x Digital
Storage	SD Card
Physical	
LCD Video Display Size	4.3 in.
Insertion Tube Length	4.92 ft.
Insertion Tube Diameter	~ 3/16 in.
Insertion Tube Material	High-Density Braided Tungsten
Articulation Control	4-Way Mechanically Controlled Joystick Articulation
Articulation Range of Motion	360° Full Rotation
Articulation Bending Angle	> 120°
Power	Rechargeable Lithium-Ion Battery

The MC1 insertion tube is entirely flexible and unsupported with the exception of the approximately 1.5-in. articulating tip. Typical applications for the MC1 include inspecting internal portions of engines or small diameter plumbing systems. In these typical applications, the insertion tube is guided toward the area of interest by the articulating tip, and the flexibility of the insertion tube facilitates its ability to be inserted into tight spaces. For inspecting camouflets, simply lowering the insertion tube into the camouflet allowed it to swing freely, and the camera was not steady enough to capture useful images or video. Therefore, the insertion tube was attached at the end to the Uniprise flexible tubing discussed in Section 3.3.5 so that the articulating tip extended beyond the end of the Uniprise tubing, allowing it to retain its full range of articulation. The Uniprise tubing was

used to position and steady the MC1 camera inside the camouflet as shown in Figure 3.10. The Uniprise tubing was rotated to pan the MC1 camera and obtain a video of the entire interior of a camouflet. A full recording of a camouflet required approximately 2 to 3 min.

Preliminary laboratory testing in the camouflet model indicated the MC1's lighting was insufficient to illuminate the inside of the camouflet. This was not unexpected since its use in this project differed considerably from its typical applications (i.e., small spaces, close-up viewing). In order to still use the MC1, a supplementary light source was utilized. A simple hanging work light with the protective guard removed (Figure 3.11) was chosen as a quick solution. While this would not be the ideal solution in everyday use, it was adequate for this project.

Figure 3.11. Supplementary light source used to illuminate camouflets for MC1.

3.3.3 Subsea video systems camera

A submersible camera manufactured by Subsea Video Systems Inc. (SVS) and attached to a load-bearing cable was also used for visual inspection and possibly photogrammetry. Figure 3.12 shows the camera, which was equipped with both a horizontal camera and a vertical nose camera, being lowered into a camouflet. For illumination, it was equipped with two LED light arrays, one on the side for the horizontal camera and one on the nose for the vertical camera. A small control unit, shown in Figure 3.12, was used to view the video feed as well as select the camera being viewed, control light intensity, and start or stop recording video. The SVS camera was tested only in the field with full-scale Camouflets 2 and 12; it was not available for laboratory testing.

Figure 3.12. SVS camera photographs.

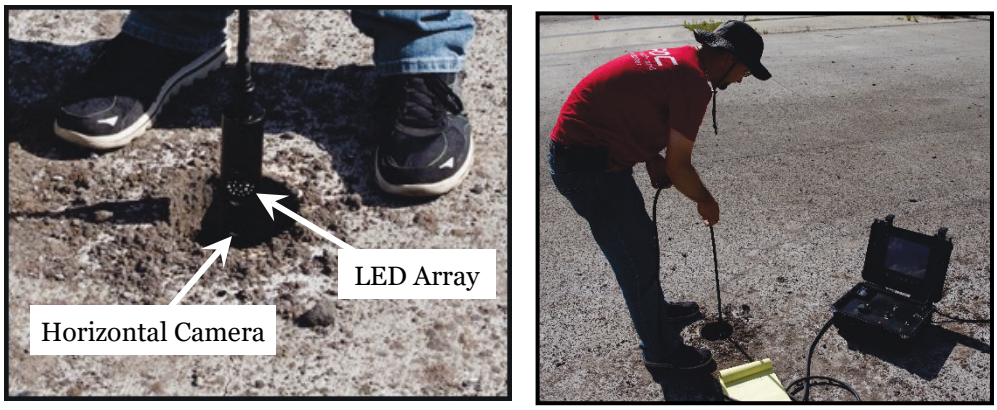

The general process was to suspend the camera near a camouflet OPE, begin the video recording, and then slowly lower the camera to the bottom of the camouflet. Then, the camera was raised to the camouflet OPE again, rotated slightly, and lowered again. This process was repeated until overlapping up-and-down shots had been obtained for the entire camouflet (i.e., full coverage of the interior of the camouflet). Approximately 2 min were required to fully record the interior of a camouflet.

Due to temperature and humidity differences between ambient surface conditions and conditions inside camouflets, a considerable amount of condensation was produced when the SVS camera was inserted into a camouflet and would remain for a long period of time. The camera's size (at least relative to the MC1 camera) likely affected this as well since it would take longer to equalize to the surrounding temperature. To combat this to the extent possible, the camera was lowered into a camouflet, left alone for several minutes, withdrawn briefly to wipe condensation off the camera lens, and then quickly reinserted into the camouflet for video recording. This approach mostly alleviated the issue but was much less efficient.

3.3.4 Modified laser range finder

A Bosch GLM 50c laser range finder (Figure 3.13) was modified with an extension handle so that the device could be inserted into a camouflet and take distance measurements. The extension handle included a plunger (Figure 3.14a) that allowed the user to, from the handle, press the button to record a measurement on the GLM 50c. It also included an adjustable collar (Figure 3.14b) that allowed a specific depth to be maintained as well as an adjustable pivot that allowed the GLM 50c to be positioned at either

90° (horizontal), 45°, or 0° (vertical) as shown in Figure 3.14c to Figure 3.14e, respectively. Together, this system is referred to herein as the modified laser range finder (MLRF). It was evaluated both in the laboratory model camouflet and in full-scale camouflets at Silver Flag. Appendix C provides detailed drawings for the MLRF for reproduction.

Figure 3.13. MLRF overview.

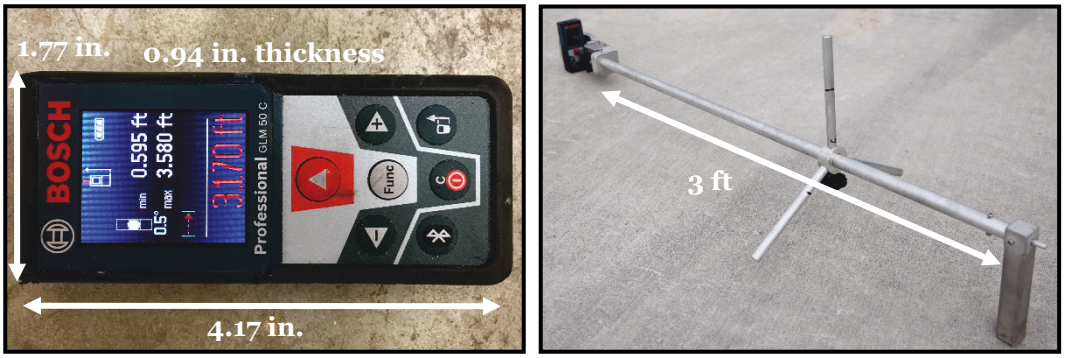

Figure 3.14. Key features of the MLRF extension handle.

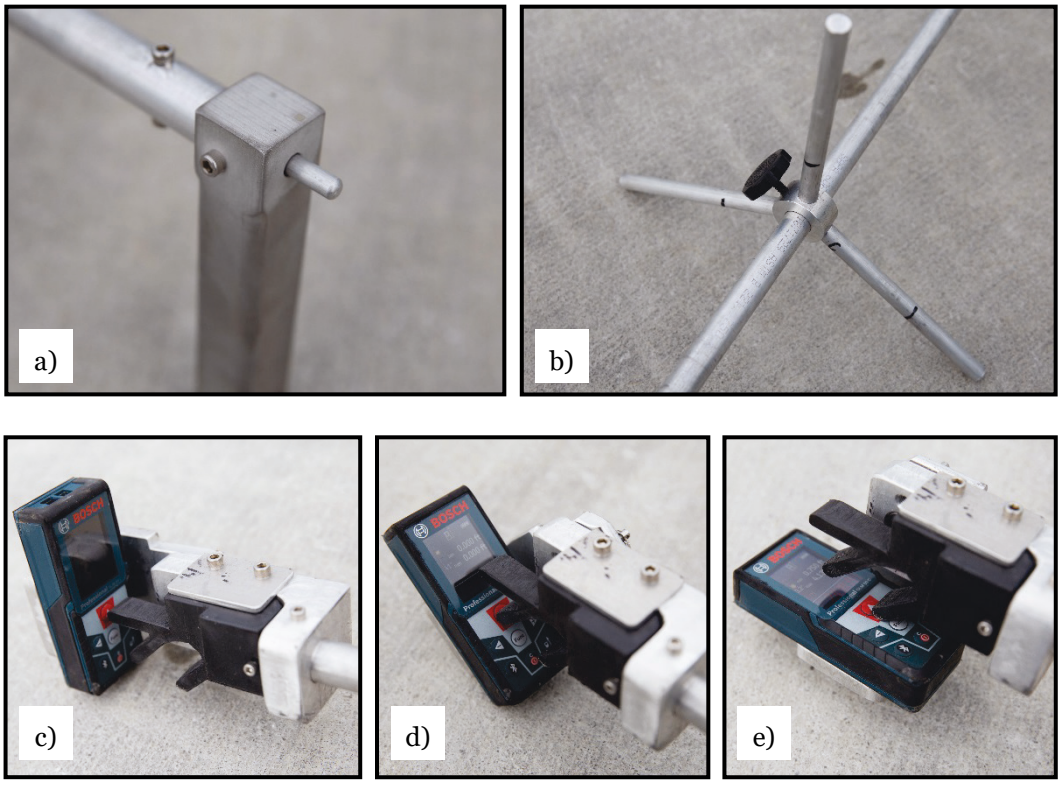

When the MLRF was inserted into a camouflet, data were obtained by several means. When the MLRF was positioned horizontally (Figure 3.14c), the screen was generally visible from the surface; thus, the operator could read the screen directly. Alternatively, the GLM 50c is equipped with

Bluetooth® and can connect with an Apple iOS or Android device running the Bosch GLM Measure & Document application. This allows the operator to simply depress the handle's plunger whenever a reading is desired and then view the result on a smartphone or tablet, ideal for when the GLM 50c screen is not visible.

The GLM 50c measures distance and also has a built-in inclinometer for angle measurements. Distance measurements can be taken from one of three reference points: (1) the front of the GLM 50c, (2) the back of the GLM 50c, or (3) the middle of the GLM 50c where the screw-thread mounting point was located. The middle was used as the primary reference point in this project since it was most closely in line with the extension handle's shaft. The GLM 50c was generally operated in a "live" measurement mode, which shows instantaneous distance and angle measurements as well as minimum and maximum distances measured as can be seen in Figure 3.13. At any time, the plunger could be depressed to record a distance measurement and send it to the paired Bluetooth device. When the MLRF was at 90° and the screen was visible, the live angle reading was helpful in confirming the MLRF was being held level.

Figure 3.15 illustrates the MLRF in use. Two measuring procedures were considered and are compared later in this report. The first procedure is referred to as the fixed-depth procedure, and the second is referred to as the fixed-angle procedure.

Figure 3.15. MLRF being used to measure camouflets.

In the fixed-depth procedure, the MLRF was first set at the 90° position (Figure 3.14c) and gradually lowered into a camouflet hole until the GLM 50c just entered the void. The collar was locked at this point so that the depth was maintained for all subsequent measurements. Horizontal distances were then recorded at various intervals from 22.5° to 90°. For example, in the field, the first measurement was taken with the MLRF pointing north (0°), then it was rotated 45° (northeast), another measurement was taken, and so on. Once all horizontal measurements were recorded, the MLRF was rotated to the 45° position (Figure 3.14d) and reinserted to the same depth, and then measurements were recorded at the previous intervals. Lastly, the MLRF was rotated to the 0° position (Figure 3.14e) and reinserted to the same depth, and a depth measurement was recorded. In this way, multiple measurements at various angles were recorded from a single fixed point near the top of the camouflet void.

In the fixed-angle procedure, the MLRF was set at the 90° position (Figure 3.14c) for all measurements except depth. The GLM 50c screen was monitored as the MLRF was slowly lowered into a camouflet, and the collar was set at the depth at which the greatest distance measurement was observed (i.e., the depth at maximum diameter). This depth generally corresponded to the approximate mid-depth of a camouflet. Horizontal measurements were taken at various intervals as in the fixed depth procedure. Then, the MLRF was raised approximately half the depth at maximum diameter, and horizontal measurements were again recorded. Lastly, depth was obtained similarly as in the fixed-depth procedure.

3.3.5 Uniprise tubing

A 4.5-ft section of flexible tubing (Figure 3.16) was purchased from Uniprise International Inc. to measure camouflet depth and approximate diameter. It was specified as 0.750-H tubing, which implies a 0.75-in. outer diameter and a stiffness category of heavy (light, medium, and heavy were available) and was clad in black vinyl with soft PVC caps on each end. This particular tubing had a minimum bend diameter of 7 in. It is referred to as the Uniprise tubing in this report and was evaluated in the laboratory camouflet model as well as full-scale camouflets at Silver Flag.

Figure 3.16. Photographs of Uniprise flexible tubing and its use.

The Uniprise tubing was selected because it was stiff enough to retain its shape when bent. Therefore, it could be partially inserted into a camouflet, gradually bent to a near 90° angle, and then inserted further until the side wall of a camouflet was contacted. The tubing was grasped at the interface of the concrete and base (i.e., near the opening into the camouflet void), removed from the hole, and measured as illustrated in Figure 3.16. This provided a general idea of camouflet width. Depth was also measured.

3.3.6 Loc-Line tubing

A 5-ft section of modular plastic Loc-Line tubing (Figure 3.17) manufactured by Lockwood Products Inc. was used to measure camouflet depth and approximate diameter similar to the Uniprise tubing. The tubing was specified by inner diameter, which was 0.50-in. inner diameter. It is referred to as the Loc-Line tubing in this report and was evaluated in the laboratory camouflet model as well as full-scale camouflets at Silver Flag.

Figure 3.17. Photographs of Loc-Line tubing and its use.

The Loc-Line tubing was selected for similar reasons as the Uniprise tubing in that it could be bent and then maintain its shape. The procedure used to measure camouflets was similar to the Uniprise tubing. It was

partially inserted into a camouflet, gradually worked into a near 90° bend, and further inserted to the camouflet side wall. The tubing was then grasped at the interface of the concrete and base, removed, and measured as illustrated in Figure 3.17. Depth was also measured.

3.3.7 Plumb bob

A plumb bob was the simplest technique used in this project and was used to obtain only depth with the idea that camouflet height and volume would be somewhat related. It was evaluated in the laboratory camouflet model as well as full-scale camouflets at Silver Flag.

Figure 3.18 illustrates the process of measuring depth with the plumb bob. It was lowered into a camouflet until it contacted the bottom of the camouflet. The plumb bob string was grasped level with the pavement surface and then measured. Concrete thickness was then subtracted to obtain the camouflet height.

Figure 3.18. Photographs of the plumb bob and its use.

3.3.8 Laboratory model camouflet

A model camouflet (Figure 3.19) was constructed in the laboratory at ERDC using ERDC's medium-scale test box in order to conduct trials with void characterization techniques discussed in the previous sections. A wooden frame was first built to support a plywood covering that was later laid over the top to simulate a concrete slab. The box was then filled with approximately 2 ft^3 of silty soil, which was chosen primarily because it was readily available and had some plasticity, helping it to hold its form when shaped. Once the soil was formed to the desired shape and leveled, reinforced 0.75-in. plywood with a 6-in. diameter hole in the center was laid across the model. An 18-in. section of 6-in. diameter pipe (not shown in Figure 3.19) was mounted over the plywood hole in order to approximate an 18-in. concrete slab (it would be more difficult, but more realistic, for inserting and operating void characterization tools).

Figure 3.19. Model camouflet construction.

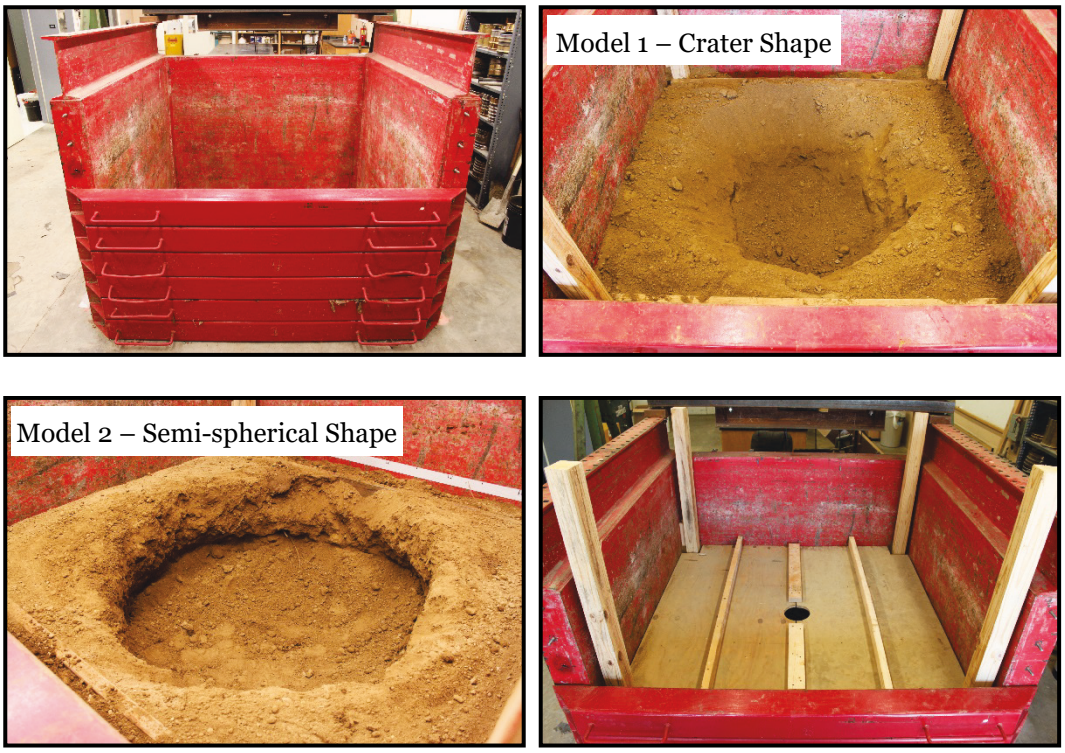

As shown in Figure 3.19, two different camouflet models were constructed primarily because it was not fully known what type of scenario might be encountered with actual camouflets at Silver Flag. Model 1 was built to resemble a basic crater shape with walls sloping up to the underside of the plywood covering (i.e., simulated concrete slab) and away from the camouflet hole.

Model 2 was built to resemble more of a spherical shape based on the suggestions of Bull and Woodford's works as in Figure 2.2. Constructing a fully spherical shape by hand that would not also collapse was not feasible. Walls were constructed which sloped towards the camouflet hole to the degree possible, which generally resulted in vertical to slightly sloped (toward the camouflet hole) walls. The bottom section of the model was formed in a bowl shape. Although Model 2 was not a sphere, the key aspect that was needed to differentiate from Model 1 was that the greatest diameter was at some depth within the camouflet versus at the top of the camouflet just below the plywood.

3.3.9 Destructive void characterization

During full-scale testing at Silver Flag, a single camouflet (Camouflet 12) was dedicated to destructive void characterization where all previously discussed void characterization techniques were conducted, and then the camouflet was deconstructed for direct measurements and visual inspection. This was conducted in order to physically observe an actual camouflet. Figure 3.20 illustrates the process of deconstructing the camouflet.

Figure 3.20. Unearthing camouflet for destructive void characterization.

After the camouflet was evaluated using all void characterization techniques, a 5-ft by 5-ft section of concrete centered over the camouflet OPE was removed. A Caterpillar 279D compact track loader (CTL) outfitted with a Caterpillar SW60 wheel saw (60-in. diameter) was used to cut through the approximately 16-in.-thick slab. The cuts were originally attempted with an SW45 wheel saw (45-in. diameter), but it was not large enough to cut through the entire thickness of the slab.

Anchor bolts were then installed to lift the slab off the camouflet. The slab was fractured into three pieces during the camouflet blast and, therefore, had to be removed in stages. A rotary hammer and 1.25-in. masonry bit were used to drill holes into which concrete expansion anchors (Simpson's Torq-Cut™ TCAP751458) were set. A Caterpillar TH514 telehandler was used to lift the slab portion out of the surrounding slab. Figure 3.20 shows the base material with the slab removed. In order to expose the camouflet, base material was gradually removed by hand. An effort was made to limit the amount of base material that fell into the camouflet, although this was not completely possible; any material that fell was removed carefully as to disturb the original camouflet surfaces as little as possible.

3.4 Field site description and camouflet generation

3.4.1 Field site description

Full-scale field testing was conducted in September 2016 at the Silver Flag Exercise Site (referred to as Silver Flag throughout this report) at Tyndall Air Force Base, FL. This site was selected for its ability to conduct the live blasting needed to generate camouflets. The site is located in a humid, temperate climate.

Work was conducted on the south end of the runway as shown in Figure 3.21, and the south connecting taxiway was used as a storage and staging area for equipment and materials. Figure 3.22 shows the south end of the Silver Flag runway (work was conducted both south of and under the rain system). Slabs in the area tested were 15 by 15 ft with thicknesses generally around 10 to 11 in. but approximately 16 in. at one location. Base materials ranged from a silty sand to a sandy gravel with a relatively high water table.

Figure 3.21. Overview of Silver Flag site for camouflet testing.

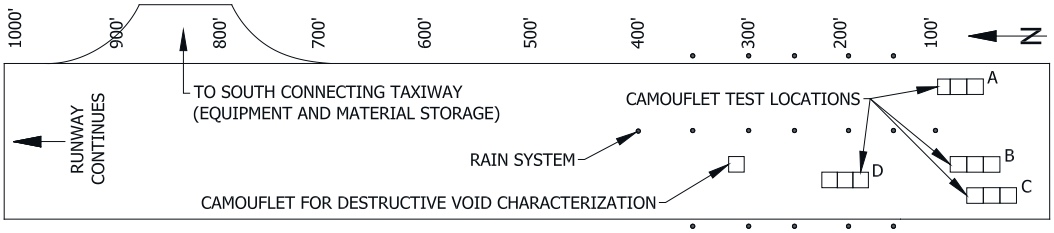

Figure 3.22. Photograph of the Silver Flag runway (south end looking north).

The initial test plan, discussed further in Section 3.5.1, included a total of 13 camouflets and was provided to AFCEC prior to field work. AFCEC used the information to select the specific test slabs at Silver Flag. The test plan called for four series (A, B, C, and D in Figure 3.21) of three adjacent slabs plus one additional slab that would be used for destructive void characterization. Sufficient room was required around each series to operate construction equipment as well as a C-17 load cart.

Originally, it was believed that concrete thicknesses were all approximately 11 in.; however, it was later discovered that thicknesses varied considerably as slabs had been placed in multiple pours with varying concrete strengths. Table 3.7 provides concrete slab and strength data obtained during field testing; therefore, this information was not available at the time test slabs were selected.

Table 3.7. Existing slab thickness and strength by camouflet series.

Series	Approx. Concrete Thickness (in.)	Approx. Concrete Strength (psi)
A	12 to 12.5	8,300
B	9 to 11	4,000
C	9 to 11	5,100
D	16 to 17	8,700

-- Compressive strengths obtained according to ASTM C39 on cylinders cored from slabs
-- Only 1 core tested from Series A and D since slabs were simultaneously constructed
-- 1 core from each slab in Series B and C was tested since slabs were individually constructed; average compressive strength for the series is shown

Series A and D were a part of larger pours that were placed continuously by a contractor and later saw-cut (as in more traditional concrete paving). Although these were placed at two different thicknesses, thicknesses among slabs in the same series were relatively consistent, and strengths between Series A and D were relatively similar. In contrast, slabs in Series B and C were poured individually one slab at a time by troops during Silver Flag training classes. Consequently, slab thickness varied considerably, and slab joints were not aligned. Strengths were also considerably different than the contractor-placed strengths. On average, Series B and C slabs exhibited 52% of Series A and D slab strengths.

3.4.2 Camouflet generation

AFCEC was responsible for coordinating the blast events required to generate camouflets according to the test plan provided by ERDC. AFCEC performed all preparation work needed prior to blasting. Blasting was to occur the day before testing began as there were concerns that camouflets may fill with water (the water table was particularly high at the time due to heavy rains leading up to the field testing).

To prepare a slab for a camouflet (Figure 3.23), a 6-in.-diameter core was first cut and removed from the center of a slab. Then, a 4-in.-diameter CTL auger attachment was used to auger approximately 4 ft deep. A section of 4-in.-diameter schedule 40 PVC pipe was cut to 43.5 in., capped on one end with a PVC end cap, and inserted (capped end first) into the auger hole until flush with the surrounding slab. The upper open end was covered temporarily with duct tape to prevent debris from falling into the PVC pipe. Sand and base material were swept back into the hole to fill most of it, and grout was used to fill the remainder (approximately the final few inches) as shown in Figure 3.24a. For blasting, the duct tape was removed, and one 1.25-lb block of C-4 (initially) was inserted and detonated. This produced little to no cracking within the slab and was the method typically used for other camouflet blasting exercises at Silver Flag.

Figure 3.23. Slab preparation process for camouflet blasting.

Figure 3.24. Comparison of PVC pipe installation methods.

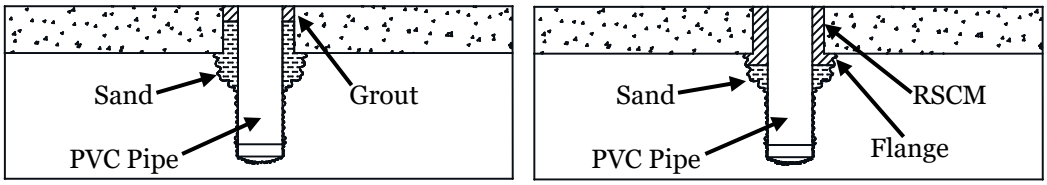

a) Typical PVC Pipe Installation

b) Modified PVC Pipe Installation

After the camouflets for this project were created, void characterization attempts revealed that the blasting method employed did not create a camouflet of any meaningful size. It appeared that most of the blast energy dissipated through the 6-in. hole in the surface of the concrete slab. For all camouflets attempted, this yielded an approximately 4-ft-deep shaft that was approximately 6 to 8 in. wide. Since this result was not representative of a camouflet, additional blasts were conducted.

For the second round of blasts, a slightly modified procedure was utilized. The follow-up blasts were conducted on the same slabs, i.e., the same 6-in. core holes were used. Each hole was re-bored with the auger and then implanted with new PVC pipe assemblies. Sandy base material was used to backfill the hole again; however, in this case, only to within an inch or so of the bottom surface of the concrete slab as illustrated by Figure 3.24b. RSCM (instead of grout) was used to cap the hole. Reducing the amount of sand backfill allowed the RSCM to spread out slightly underneath the existing slab (base material underneath the slab typically fell into the hole as shown in Figure 3.24) This created an RSCM flange that would aid in preventing the RSCM from being blown out during the blast and helped to contain more energy within the base layer. Unlike the grout that fully blew out during blasting, the RSCM approach often resulted in materials remaining lodged in the camouflet OPE after blasting as shown in Figure 3.25. This was removed primarily with a rotary hammer.

Figure 3.25. Removal of RSCM and PVC after blasting.

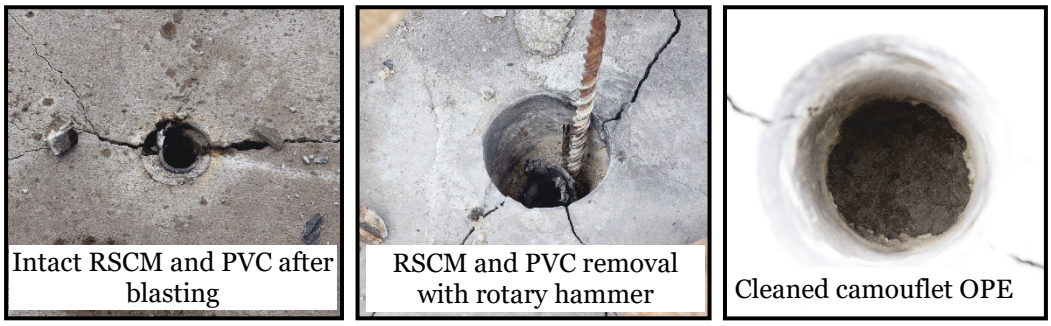

Also for the second round of blasts, C-4 charges were varied in order to determine the charge size that would create the largest camouflet possible without causing significant slab damage. An iterative approach was taken to select the final C-4 charge in which 2 to 4 blocks of C-4 were considered. Ultimately, 2 blocks of C-4 were used for all camouflets that remained after the trial-and-error testing with various C-4 charges. The test plan discussed in Section 3.5.1 provides details regarding specific charge sizes for each camouflet.

3.5 Camouflet repairs

3.5.1 Test plan

Table 3.8 provides a layout of the final test plan utilized for the camouflet repairs at Silver Flag, which differed from the original test plan. The original test plan included 13 camouflets (4 series of 3 camouflets each plus 1 camouflet for destructive void characterization (DVC)). This original test plan was provided to AFCEC to select the test slabs at Silver Flag. In the first round of camouflet blasts, all 13 camouflets were created; however, as stated in Section 3.4.2, the first blasting event used 1 block of C-4 per slab, which did not create suitable camouflets. Therefore, a second blasting event was conducted as described in Section 3.4.2. The test plan was truncated slightly (Table 3.8) due to the logistical burden of conducting a second blast as well as to alleviate pressure to the field work schedule caused by the blasting setback.

In the final test matrix shown in Table 3.8, Camouflets 9 and 13 were abandoned. This decision was made based on the loss of Camouflet 9 during the second round of blasting; too large of a C-4 charge (3 blocks) was used during trial-and-error blasting and produced a crater. The test plan was adjusted to where the 1-hr cure time camouflets were removed from Series C (because Camouflet 9 was lost) and D (because Camouflet 12 was reassigned to destructive void characterization). Series C and D were tested

at the 0.5- and 2-hr cure times only. Camouflet 13 was abandoned based on time and schedule considerations. Ultimately, the reorganized test plan still allowed both flowable fill products (of primary interest) to be tested at three cure times, RSCM and FI-10S (of secondary interest) were tested at two cure times, and the destructive void characterization was still conducted.

Table 3.8. Final Silver Flag camouflet repairs test matrix.

Series	Repair Material	Camouflet ID	Cure Time (hr)	Placement Method
A	FF-BU (Buzzi Unicem Flowable Fill)	1	0.5	SVM & Mini Hopper
		2	1	SVM & Mini Hopper
		3	2	SVM & Tremie Funnel
B	FF-CTS (CTS Cement Flowable Fill)	4	0.5	SVM & Mini Hopper
		5	1	SVM & Tremie Funnel
		6	2	SVM & Tremie Funnel
C	RSCM (Rapid Set® Concrete Mix)	7	0.5	SVM & Tremie Funnel
		8	2	SVM & Tremie Funnel
D	FI-10S (Foam-iT! 10 SLOW)	10	0.5	Hand
		11	2	Hand
Destructive Void Characterization (DVC)		12	—	—

-- Camouflets 1 to 8 were created using 2 blocks of C-4
-- Camouflet 9 (not in test plan) yielded a crater with 3 blocks of C-4
-- Camouflets 10, 11, and 12 were created using 3, 3.5, and 4 blocks of C-4
-- SVM is simplified volumetric mixer; Section 3.5.3 describes SVM, Mini Hopper, and Tremie Funnel

In slabs that were 9 to 12 in. thick (Series A, B, and C), 2 blocks of C-4 were used to create successful camouflets, and 3 to 4 blocks of C-4 were used for the 16-in.-thick slabs (Series D). Based on void characterization results, 3 blocks of C-4 were least optimal for the 16-in. concrete (i.e., the camouflet was still fairly small); 3.5 and 4 blocks of C-4 produced suitable camouflets that were similar in size. With these charge sizes, meaningful cracking and heaving was produced in the slabs (discussed further in Chapter 7), but slabs remained mostly intact. Given the limited number of blasting trials available to select the most ideal C-4 charge, this outcome was deemed the best balance between camouflet size and slab damage.

3.5.2 Weather

Weather data from the camouflet field testing were obtained from the BayfrontWX [KFLPANAM43] weather station located approximately 7.5 miles northwest of the test site at Silver Flag and are shown in Table 3.9. The temperature averaged 80°F overall and ranged from 69 to 93°F. Relative humidity averaged 81% and ranged from 42 to 100%. Being relatively close to the coastline, there was a fairly constant breeze with winds and gusts increasing up to 30 mph with the onset of Hurricane Hermine. Hurricane Hermine made landfall the night of 1 Sept

approximately 90 miles east of Silver Flag. Its overall width covered Silver Flag but only slightly. Silver Flag experienced high wind gusts and modest rain. As Hurricane Hermine moved further inland, heavy rain trailing it passed over Silver Flag on 4 Sept. From 5 Sept on, temperatures increased slightly, and no rain was observed.

Table 3.9. Weather data at Silver Flag for camouflet project.

Date	Temp (°F)			Humidity (%)			Wind (mph)		Max Gust (mph)	Daily Precip. (in.)	Weather Underground Events	On-Site Events
	Max	Avg	Min	Max	Avg	Min	Max	Avg				
Prior Month Avg	89	82	76	95	81	63	16	6	21	0.5	—	—
8/29/2016	93	84	76	92	75	47	17	7	25	0.0	Rain	—
8/30/2016	91	83	75	91	72	52	12	8		0.0	—	—
8/31/2016	88	81	74	94	80	58	17	7	17	0.2	Rain	—
9/1/2016	79	77	75	100	91	83	21	10	30	0.3	Rain	Hurricane Hermine approaching, Rain
9/2/2016	89	80	73	94	84	69	18	12	23	0.6	Rain-Thunderstorm	Hurricane Hermine made landfall night before, Hot, Sunny, Dry
9/3/2016	85	78	73	96	87	74	14	5	—	0.1	Rain-Thunderstorm	Hot/Warm, Cloudy
9/4/2016	78	76	73	100	95	89	12	5	—	4.0	Fog-Rain-Thunderstorm	Wet, Rainy, Thunderstorm during Camouflet 7 repair
9/5/2016	87	80	74	96	81	65	13	6	—	0.0	Rain	Hot, Dry, Partly cloudy
9/6/2016	89	80	72	92	72	42	9	5	—	0.0	—	Hot, Dry
9/7/2016	89	79	69	100	79	45	12	3	—	0.0	—	Hot, Dry
9/8/2016	88	78	69	97	76	52	12	3	—	0.0	—	Hot, Dry
9/9/2016	90	79	69	96	75	59	12	3	—	0.0	—	Hot, Dry
Avg	**87**	**80**	**73**	**96**	**81**	**61**	**14**	**6**	**24**	**0.4**	**—**	**—**
Min	**78**	**76**	**69**	**91**	**72**	**42**	**9**	**3**	**17**	**0.0**	**—**	**—**
Max	**93**	**84**	**76**	**100**	**95**	**89**	**21**	**12**	**30**	**4.0**	**—**	**—**

-- Data source: www.weatherunderground.com; Weather Underground events are those reported by Weather Underground which may or may not have coincided with weather events actually recorded on-site at Silver Flag.
-- Avg, min, and max values cover data from 8/29/2016 to 9/9/2016

3.5.3 Equipment

Numerous pieces of heavy equipment were used during the field testing at Silver Flag. Figure 3.26 shows examples of the types of equipment used, including a Caterpillar M318D wheeled excavator, a Caterpillar 279D CTL, a Caterpillar 277C CTL, a Caterpillar TH514C telehandler, and a 4,000-gal water truck. Most equipment was rented for general use material moving and handling. The 277C CTL was shipped from ERDC Vicksburg to Silver Flag for the work alongside multiple attachments: a set of pallet forks, a power broom, an SW45 wheel saw, and a bucket. Relative to other heavy equipment used in this project, CTLs and telehandlers were utilized specifically during actual camouflet repair processes.

Figure 3.26. Examples of general equipment used at Silver Flag.

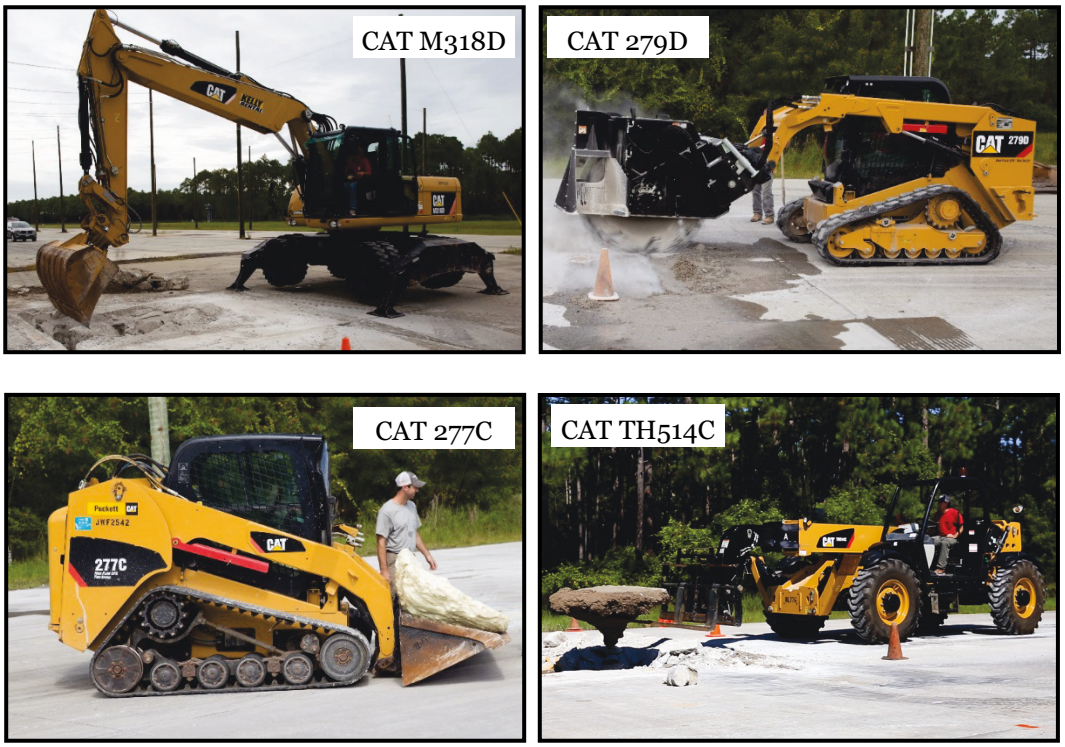

The CTLs, or skid steers, used at Silver Flag were rubber-tracked machines with high-flow hydraulics and quick-connect fittings. They are used extensively in modernized ADR processes as they are versatile and efficient for many purposes (e.g., quick-connect fittings allow attachments to be rapidly swapped without tools). Among other tasks, CTLs are often used for rapid cutting around crater upheaval using wheel saw attachments, debris removal and material handling with bucket attachments, and site cleanup with broom attachments. Table 3.10 provides specifications of the 277C (shipped from ERDC) and the 279D (borrowed from Silver Flag) CTLs.

Table 3.10. Caterpillar 277C and 279D CTL specifications.

Property	277C	279D
Net Power	82 hp	73 hp
Operating Weight	9,495 lb	9,893 lb
Rated Operating Capacity (at 50% tipping load)	3,200 lb	2,935 lb
Tipping Load	6,675 lb	5,870 lb
Breakout Force, Tilt Cylinder	7,308 lb	7,285 lb
Travel Speed	9.3 mph	7.0 mph
Maximum Loader Hydraulic Pressure	4,061 psi	4,061 psi
Maximum Loader Hydraulic Flow	33 gal/min	32 gal/min
Track Suspension System	Yes	No

-- Travel speed, maximum loader hydraulic pressure, and maximum loader hydraulic flow specifications are for high flow XPS models

A Caterpillar TH514C telehandler, or extendable boom forklift, was used to move the 3,000-lb supersacks of pre-blended cementitious materials as well as totes containing FI-10S components. It was primarily used to load supersacks of material into the simplified volumetric mixer, as shown in Figure 3.27, since the CTLs were not capable of doing so. The TH514C has a rated load capacity of 11,000 lb with a maximum forward reach of approximately 30 ft.

Figure 3.27. Telehandler loading supersack into SVM.

The simplified volumetric mixer (SVM) that was discussed in Chapter 2 was used for the camouflet repairs in this project. The SVM, shown in Figure 3.28, is a tow-behind mixer designed by CemenTech Inc. with input from ERDC and used in the modernized ADR program. It is pre-calibrated for both rapid-setting flowable fill and rapid-setting concrete.

Figure 3.28. Simplified volumetric mixer.

The SVM is towed with a vehicle capable of pulling at least 20 tons (typically a dump truck). Key components of the SVM are a single dry material hopper (approximately 7-yd^3 capacity), a conveyor belt feed

system, a water pump to meter mix water at a fixed pump speed, two 200-gal water tanks, a washout tank, and a replaceable mixing auger mounted in a discharge boom at the rear of the mixer. The SVM is also equipped with two retractable catwalk platforms, a bin entry platform, a replacement auger, and two supersack piercing points.

Material consistency (i.e., *w/s* ratio) is controlled by adjusting a strike-off gate that changes the thickness of dry material on the conveyer belt feeding the mixing auger. Gate settings range from 1 to 12. Raising the gate (i.e., increasing the gate setting) introduces more dry material to the mixing auger and, thus, lowers *w/s* ratio, and vice versa. Typical gate settings during production for rapid-setting flowable fill and rapid-setting concrete range from 4 to 8. Non-potable well water from Silver Flag was used in the mixer for all field work; Carruth and Howard (2016) presented a chemical analysis of the water and did not observe any adverse effects of using it to produce rapid-setting cementitious materials.

A relatively simple, but critical, consideration in this project relative to other ADR projects was the method used to transfer material from the SVM to the camouflet. For typical crater repairs, the discharge boom on the SVM is backed over the crater, and material is deposited directly into the crater (Figure 3.28 illustrates this with Camouflet 9, which was repaired as a crater due to the blasting issues encountered). For camouflets, a more controlled method was needed to properly place material. Two solutions were evaluated: a mini concrete tremie hopper and a large tremie funnel.

Figure 3.29 provides photographs of the mini concrete tremie hopper (referred to hereafter as the mini hopper) purchased from Deslauriers Inc. (part number TREMH-6) for approximately $100. It consists of a high-density polyethylene hopper with an attached 8-in.-diameter elephant trunk. The mini hopper was shipped with a 6-ft elephant trunk, which was shortened to 2 to 3 ft for the camouflet project. It also included a steel rod and chains for hanging from the end of a concrete chute as shown in Figure 3.29 (zip ties were also used for extra measure).

Figure 3.29. Photographs of the mini concrete hopper.

Figure 3.30 provides photographs of the tremie funnel purchased from Superchute Ltd. for approximately $350. It is made from high-density polyethylene and is approximately 36 in. square and 28 in. tall with a wall thickness of 0.25 in. The funnel features a stepped neck with diameters of 4, 6, 8, 10, and 12 in. so that the funnel can be cut for an outlet at the desired diameter. In this project, the simulated camouflet OPEs were just greater than 6-in. diameter; however, in the event smaller OPEs are ever encountered, the 4-in. diameter outlet was used to determine if material flow was fast enough to match the SVM's output.

Figure 3.30. Photographs of the tremie funnel and support frame.

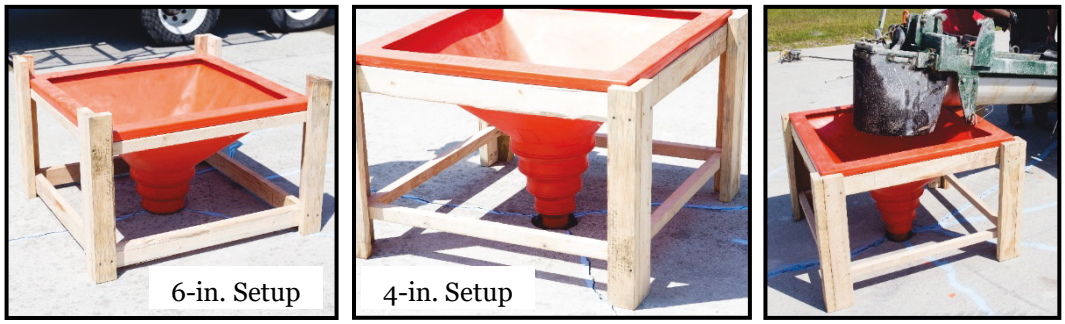

Superchute Ltd. also sells support frames designed specifically to pair with the tremie funnel; however, these were too large for the camouflet repairs. Alternatively, a similar wooden frame was built out of pine framing lumber for the camouflet project. It was built as a two-sided frame that held the funnel at two height positions: a greater height for using the 4-in. diameter outlet and a lower height for using the 6-in. outlet in the event flow through the 4-in. outlet was insufficient. The discharge boom on the SVM was backed over the top of the funnel and lowered to minimize splattering to the extent possible.

3.5.4 Processes

Prior to all repairs, standing water could be observed inside each camouflet due partly to the high water table present and rain that occurred. Therefore, before a series of camouflets was repaired, water was removed to the extent possible using a Honda Model WX10TA self-priming gasoline-powered water pump. For rapid-setting cementitious material repairs, any remaining water in the camouflet was relatively insignificant. For foam repairs, any remaining water could significantly affect foam reactions; therefore, a partial 5-gal bucket of dry cementitious material (flowable fill or concrete) was poured into each camouflet in attempts to absorb any local free water and mitigate moisture effects.

To begin the camouflet repair process using rapid-setting cementitious materials, the SVM was prepared for standard operation. Supersacks (typically six, though four were used in one case) were loaded into the dry material bin, the water tanks were filled (both mix water tanks and washout tank), and the mixing auger and discharge boom were sprayed with concrete release agent. The extension chute was attached to the discharge boom when the mini hopper was used for placement (shown in Figure 3.29) and was removed when the tremie funnel was used for placement (shown in Figure 3.30).

The water pump gear speed, which can be set for rapid-setting flowable fill or rapid-setting concrete, was selected based on the material being placed. These gear speeds correspond to the water flow rates calibrated for each material (approximately 70 gal per supersack at a gate setting of 6 for flowable fill and 50 gal per supersack for concrete). No chemical admixtures were used during this testing since admixtures are not typically used when rapid-setting flowable fill is used as a backfill material for crater repairs.

As discussed in Section 3.5.3, the SVM has an adjustable strike-off gate that controls the amount of dry material on the conveyer belt feeding the mix auger, adjusting the *w/s* ratio. Gate settings around 6 are typical and are adjusted as needed to produce the optimal material consistency for the repair application at hand. In this project, gate settings were set at 5.6 for FF-BU and RSCM and 6.5 for FF-CTS.

The first portion of material discharged from the SVM for each series of pours was predominantly water since there was initially no dry material on

the conveyer belt. This is usually not a large concern for craters as material consistency reaches a steady state within several seconds; thus, the amount of lean material placed is fairly insignificant relative to the size of the overall pour. Since it could have a greater effect for the smaller camouflets, the SVM was primed at the beginning of each series by discharging material into a CTL bucket until consistency equalized as shown in Figure 3.31a (this also allowed time for gate settings to be adjusted).

Figure 3.31. Camouflet repair procedures using rapid-setting cementitious materials.

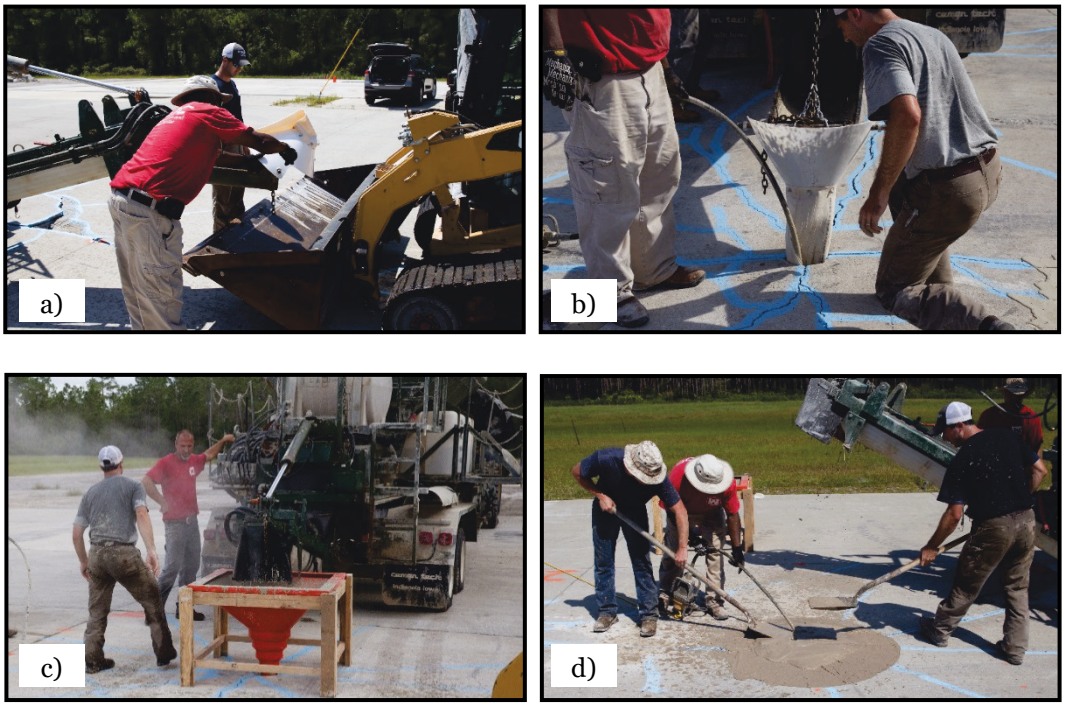

Figure 3.31b and Figure 3.31c illustrate the use of the mini hopper and tremie funnel during placement. In both cases, the discharge boom was lowered to an angle of 10 to 15°. Rapid-setting flowable fill or rapid-setting concrete was produced until each camouflet was filled. Tracking the fill level within the camouflet as it rose was not straightforward. The simplest, yet relatively effective, means of tracking fill level was for an engineer or technician to insert his hand into the camouflet OPE alongside the mini hopper or tremie funnel and feel for material as the level rose. This was the most effective (although maybe not the most practical long-term) solution to determine when to stop SVM production with minimal overflow.

Once filled, any excess material that overfilled the camouflet was cleaned up using flat shovels and push brooms. Simultaneously, a concrete vibrator for consolidating concrete was inserted into the camouflet to

assist the material in flowing into all cavities of the camouflet as shown in Figure 3.31d. This generally provided some additional consolidation; excess overflow material was shoveled into the camouflet to bring the fill level back to flush with the surrounding slab.

Each pour was relatively fast, requiring only 2 to 3 min. This left a considerable amount of time between pours in a series since cure times were planned for 0.5, 1, and 2 hr. To keep the SVM from seizing in between pours, it was towed away from the test site for cleaning after each camouflet. The auger and discharge boom were cleaned with a pressure washer, while dry materials were left in the bin for the next pour.

For polyurethane foam repairs, two totes containing FI-10S components A and B were placed to near the camouflet being repaired. Approximate volumes of the camouflet voids were calculated using void characterization data and then divided by 6 (FI-10S expansion ratio is typically 5.8) to determine the estimated volume of FI-10S liquid required. Individual batches of FI-10S were produced in metal 5-gal buckets at a 1:1 ratio of Component A and Component B by volume. Batch sizes were recorded, and enough batches were produced to fully fill the camouflet.

Each foam component was first batched to the appropriate volume in separate metal buckets and then combined and mixed in a third metal bucket. Figure 3.32a illustrates the process of mixing FI-10S with a large electric drill and a paddle mixing attachment. Each batch was mixed at a high speed for 1 min and then immediately poured into the camouflet as shown in Figure 3.32b. After pouring into the camouflet, each batch was given several minutes to fully react and expand before the next batch was mixed and poured. Batches continued to be mixed and poured into the camouflet until foam overfilled it as shown in Figure 3.32c. Excess foam was removed by scraping it off with a CTL bucket.

Figure 3.32. Camouflet repair procedures using rigid polyurethane foam.

3.6 Camouflet repair assessment

3.6.1 Material characterization

During field repair processes, cylinders were cast for strength testing (Figure 3.33), generally after all camouflet repairs in a particular series were completed. Nine cylinders were cast for each cementitious material (FF-BU, FF-CTS, and RSCM) for ASTM C39 (2016) compressive strength testing after 2 hr, 1 day, and 28 days of curing. Three cylinders were cast for FI-10S and were tested at approximately 9 days, though foam strengths are not greatly dependent on cure time beyond several hours of curing. A total of 30 cylinders were tested among the four cementitious and foam materials.

Figure 3.33. Example photographs of FF-CTS and FI-10S test cylinders.

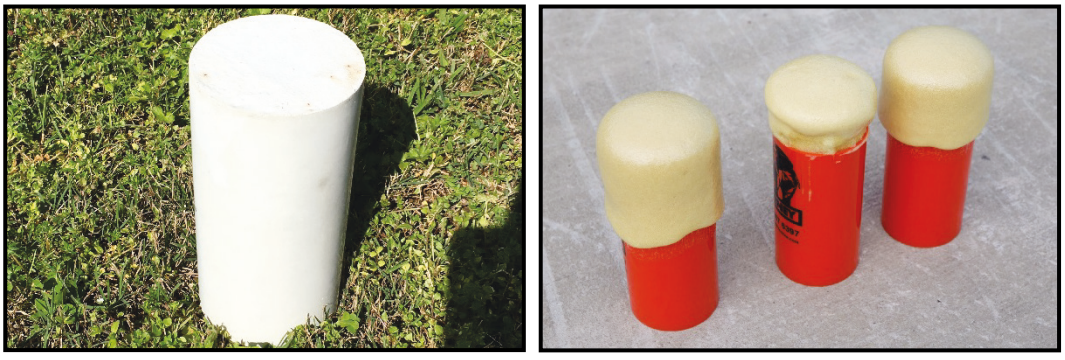

Flowable fill and concrete cylinders were cast using material sampled directly from the SVM with buckets. Because of the quick set times, cylinders were tamped around their exterior but not rodded as specified in ASTM C39 (2016); however, omission of this step does not typically result

in consolidation issues because the materials have relatively small aggregate sizes and are relatively flowable. Cylinders were struck off, capped, and placed on the Silver Flag runway to cure in close proximity to camouflet repairs. For 2-hr and 1-day cylinders, the entirety of their curing occurred in the field; 28-day cylinders were cured in the field for 5 to 7 days, in transit for 3 days, and in the laboratory according to ASTM C192 (2016) for the remaining cure period. The 2-hr and 1-day cylinders were tested at the Applied Research Associates (ARA) laboratory located several miles from Silver Flag using neoprene pad caps. The 28-day cylinders were tested by the Concrete and Materials Branch (CMB) at ERDC's Materials Testing Center (MTC); cylinders were end-ground and tested without pad caps.

Foam cylinders were cast using material mixed in 5-gal metal buckets as with the camouflet repairs. They were demolded, prepared, and tested for ASTM D1621 (2016) compressive strength following the procedures outlined in Section 3.2.2.

3.6.2 Load cart trafficking

A multiple wheel C-17 load cart (Figure 3.34) was designed to match the geometry and loading of one half of the main gear of a C-17 fully loaded to its maximum takeoff weight of approximately 586,000 lb. The weight of the load cart itself was approximately 269,560 lb; individual wheel loads were approximately 44,930 lb. The load cart contained six wheels arranged in a triple-wheel tandem configuration. The gear used 50-in.-diameter, 21-in.-wide, 20-ply tires maintained at a normal operating pressure of 138 to 144 psi.

Figure 3.34. C-17 load cart.

For all repairs, initial load cart trafficking was begun 2 hr after the first camouflet repair in a series was completed. During the time between repairs and trafficking, the traffic distribution pattern was established. Figure 3.35a illustrates the 28-pass approximated normal distribution

pattern used to approximate C-17 wheel wander. Six traffic lines spaced 18 in. apart were painted on the pavement (Figure 3.35b) and used as visual guides for the load cart operator during trafficking. Each 28-pass pattern is referred to herein as one pattern.

Figure 3.35. C-17 load cart traffic distribution pattern.

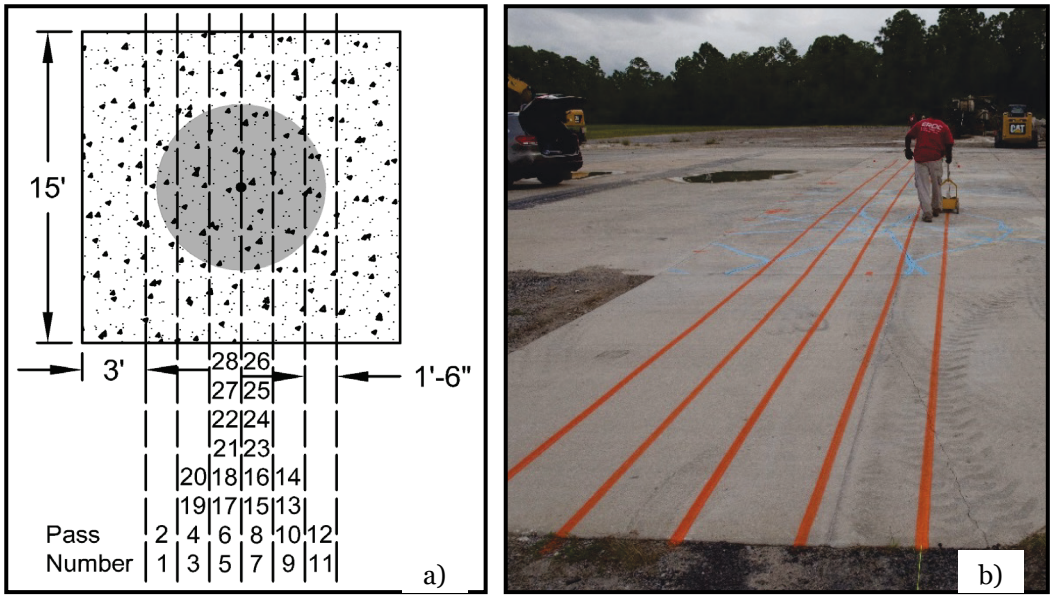

Initial load cart trafficking consisted of 112 passes (4 patterns) and was conducted at cure times of 30 min to 2 hr (depending on the camouflet in the series). Initial trafficking was to investigate each repairs' ability to support load at early cure times. Final trafficking was conducted later during the field work and was to investigate each repairs' overall structural capacity. Final trafficking was conducted to as many passes (in multiples of 28 passes) as achievable during the time available at Silver Flag or until degradation of the repair made it no longer safe to traffic. Ultimately, 112 passes were applied to Camouflet Series B and C, 1,192 passes were applied in all (initial and final trafficking) to Series A, and 1,568 passes were applied in all to Series D.

3.6.3 Visual assessment

For each slab repaired, cracks were mapped, as shown in Figure 3.36, with spray paint at various points during the field testing including at 0 passes (i.e., prior to repairs and trafficking) and after 112, 560, 1,008, 1,192, and 1,568 passes. Crack mapping allowed cracks occurring due to trafficking to be distinguished from those that were created during the camouflet blasts. It also allowed crack development and growth to be monitored throughout trafficking.

Figure 3.36. Crack mapping.

3.6.4 Surveys

Rod and level surveys were conducted (Figure 3.37) to measure elevation changes (upheaval, settlement, etc.) during field testing and trafficking. The roughness specification for fighter aircraft such as the F-15 is ±0.75 in. or less to ensure acceptable aircraft gear loads. This value was used as a benchmark value for analyzing camouflet upheaval due to blasting and settlement due to trafficking.

Figure 3.37. Conducting rod and level surveys.

Survey data collection was consistent for all camouflet slabs and included one longitudinal profile survey along the slab centerline and three transverse cross-section surveys at the mid-point and quarter-points of each slab (Figure 3.38). For each survey line, 20 measurements were taken. Four of these 20 were located on slabs adjacent to the camouflet slab. On each side of the camouflet slab, one measurement was 1 ft from the camouflet slab edge, and another was at the edge of the camouflet slab but still located on the adjacent slab. Within the camouflet slab, the remaining 16 measurements were spaced evenly at 1-ft intervals from one edge of the slab to the other. Survey measurement layout varied slightly

for Slab 3 which was 12 ft by 15 ft instead of 15-ft square. For Slab 3, the longitudinal profile survey consisted of only 17 measurements (still at 1-ft intervals with 4 measurements on the adjacent slabs).

Figure 3.38. Survey measurement layout.

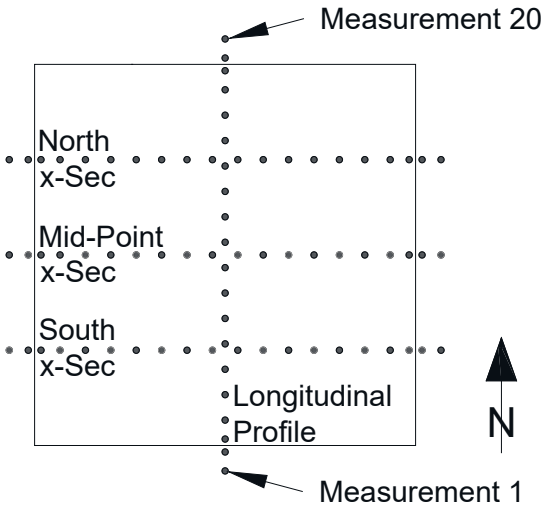

Survey data were collected at various intervals during field testing. Baseline measurements were taken after blasting and before trafficking (i.e., 0 passes). Additional measurements were taken at the same intervals as visual assessments (after 112, 560, 1,008, 1,192, and 1,568 passes). Note that no measurements were taken prior to blasting, which would have been helpful in data analysis. Measurements were not taken because prior experience with the original blasting process indicated effectively no upheaval would occur. Instead, the outside four measurements in each survey line (located on adjacent slabs) were used to approximate pre-blast baseline elevations.

3.6.5 Deflectometer testing

The heavy-weight deflectometer (HWD) shown in Figure 3.39 was used to assess the structural support of each camouflet slab at various points throughout testing. Measurements were taken prior to blasting, after blasting but before repair, after repair and curing but before trafficking (0 passes), and at the same pass intervals as visual assessments (112, 560, 1,008, 1,192, and 1,568 passes).

Figure 3.39. Heavyweight deflectometer.

The HWD consists primarily of an 11.8-in. diameter load plate to which an impulse load is applied and seven transducers that measure the corresponding deflections (Ds) at seven locations (D_1 to D_7). D_1 to D_7 locations relative to the center of the load plate were 0, 12, 24, 36, 48, 60, and 72 in., respectively. At each test location, the HWD was dropped, without relocation, 4 to 7 times at a range of loads depending on the general stiffness of the pavement. Loadings ranged from approximately 15 to 55 kips resulting in contact pressures of approximately 150 to 550 psi. Consecutive tests at various points throughout the field work occurred at essentially the same locations approximately 1 ft beside the camouflet OPE.

Camouflet characteristics were not well-suited for traditional HWD assessment. For example, slabs were considerably cracked, which would affect the stress transfer throughout the slab (and consequently affect deflection measurements). It is also important to note several other factors that could influence HWD measurements. All other factors being equal, (1) deflections would be expected to decrease (or perhaps remain approximately the same) as the camouflet repair gained strength over time, and (2) deflections would be expected to increase (or perhaps remain approximately the same) as trafficking continued (e.g., degradation of the repair, further cracking of the slab). Strength gain over time and traffic effects could not be decoupled since no un-trafficked control camouflet was repaired for comparison. Thus, HWD data was primarily useful for analysis of general trends rather than advanced characterization.

4 Laboratory Material Characterization Results

4.1 Cementitious materials

Results in this section focus primarily on FF-CTS since that material has not been previously evaluated in the laboratory. Comparisons to FF-BU and RSCM are provided where comparable data were available. Table 4.1 provides all results that are discussed further in the following paragraphs and figures. Results for FF-BU at the 0.11 *w/s* ratio were not included since they were intended to represent the dry placement method that was not a consideration of this project.

Table 4.1. Cementitious materials laboratory results.

		FF-CTS		FF-BU	RSCM
ASTM Property	Cure Time	0.21 *w/s*	0.25 *w/s*	0.21 *w/s*	
C39 Compressive Strength (psi)	1 hr	1,020	940	253	—
	2 hr	1,530	1,150	477	3,400 to 5,080
	1 d	1,960	1,720	1,035	4,510 to 6,610
	28 d	2,060	1,980	1,077	—
C78 Flexural Strength (psi)	2 hr	280	235	177	390 to 520
	1 d	440	295	302	580
	28 d	185	155	255	—
D6103 Flow (in. × in.)	n/a	9.5 × 9.5	13.0 × 13.0	16.0 × 16.0	—
D6023 Density (pcf)	n/a	119	113	119	—
C231 Air Content (%)	n/a	10	10	4	—
C403 Set Time (min)	Initial	21	24	24	— [a]
	Final	23	30	40	— [a]

a) RSCM set times were measured by ASTM C191 (Vicat needle method) instead of C403. Initial and final set times ranged from 18 to 22 min and 22 to 30 min, respectively.
-- Flowable fill results are the average of three replicates
-- The range of RSCM results from appendices in Priddy (2011) are reported

Figure 4.1 presents flowable fill compressive and flexural strength results graphically. The 0.21 and 0.25 numbers in parentheses refer to the *w/s* ratio. FF-CTS yielded compressive strengths approximately twice that or greater than FF-BU strengths at the same *w/s* ratio. At the 0.21 *w/s* ratio, FF-CTS flow consistency was noticeably less than that of FF-BU (9.5 in. vs. 16.0 in.). FF-CTS at the 0.25 *w/s* ratio provided a material closer to that of FF-BU in terms of workability; however, compressive strengths were still significantly greater. Both FF-BU and FF-CTS comfortably satisfied the minimum 750 psi requirement at 28 days in MIL-DTL-32537 (Table 3.1). For reference, RSCM was approximately 4,000 and 5,500 psi at 2 hr and 1 day, respectively (Priddy 2011).

Figure 4.1. Flowable fill laboratory compressive and flexural strengths.

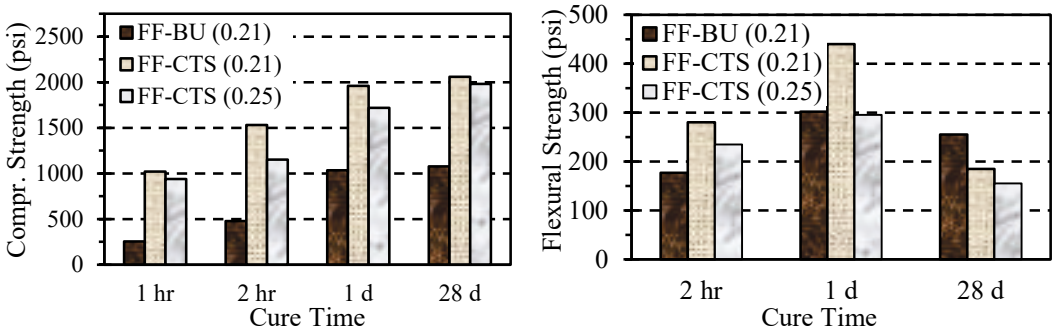

a) ASTM C39 Compressive Strength

b) ASTM C78 Flexural Strength

Differences between FF-CTS and FF-BU were smaller for flexural strength than compressive strength. With respect to FF-BU, flexural strength was considerably greater at 2 hr and 1 day for FF-CTS at the same 0.21 *w/s* ratio. FF-CTS at 0.25 *w/s* ratio yielded higher 2-hr flexural strength but effectively the same 1-day strength.

There are two key observations for 28-day flexural strengths. First, all materials exhibited a drop in flexural strength from 1 to 28 days, and, second, FF-CTS exhibited a much larger drop than FF-BU. Note that some retesting was conducted with FF-BU, and the 28-day strength drop occurred again. The mechanism responsible for this decrease in flexural strength is not currently known. Until the testing conducted in the FF-BU study and this project, flexural strength testing at cure times greater than 1 day had not been conducted for the rapid-setting cementitious materials in previous ERDC studies. In typical ADR processes, repairs conducted with RSCM or FF-BU are generally intended to be temporary; therefore, longer-term properties are of less concern. This finding is, however, unusual and unexpected and could perhaps be an area for further study.

Among the basic control parameters (flow, density, air content), flow consistency was perhaps the most interesting. At the 0.21 *w/s* ratio, workability was considerably lower (approximately half) for FF-CTS than FF-CU according to D6103 (2004). The 0.25 *w/s* ratio, which was selected to provide more favorable workability, provided a 13-in. spread according to D6103 (2004). Although this was more representative, it was still lower than the spread of FF-BU at the 0.21 *w/s* ratio. This finding is in disagreement with the field work conducted at Silver Flag and presented in Chapter 6 where *w/s* ratio was decreased for FF-CTS in order to maintain a similar consistency/workability relative to FF-BU. If interest exists with

respect to utilizing FF-CTS in normal ADR operations, this finding should perhaps be investigated further.

4.2 Foam materials

Results in this section focus primarily on RR401 and RR401G, which were tested to evaluate potential moisture insensitivity of RR401G. Ultimately, FI-10S was used in field testing; therefore, FI-10S results from a recent ERDC study on other foam materials (Gurtowski et al. 2016) are also summarized for convenience. Table 4.2 provides all results that are discussed in detail in the following paragraphs and figures.

Table 4.2. Polyurethane foam materials laboratory results.

Moisture			Material		
Condition	Property	Cure Time	RR401	RR401G	FI-10S
Dry	Pot Life (mm:ss)	n/a	~0:30	~0:30	~5:00
	Density (pcf)	1 day	6.3	6.5	12.4
	Expansion Ratio	1 day	11.5	11.1	5.8
	D1621 UCS at 2% ε (psi)	20 min	--	--	36
		30 min	--	--	121
		45 min	--	--	176
		1 hr	--	--	239
		2 hr	--	--	277
		1 day	105	109	321
Damp	Density (pcf)	1 day	5.5	5.3	--
	Expansion Ratio	1 day	13.0	13.5	--
	D1621 UCS at 2% ε (psi)	1 day	8	29	--
	UCS Reduction (%)	1 day	93	74	--
Wet	Density (pcf)	1 day	6.3	5.0	3.4
	Expansion Ratio	1 day	11.4	14.5	20.9
	D1621 UCS at 2% ε (psi)	1 day	9	13	15
	UCS Reduction (%)	1 day	91	89	95

-- Pot life refers to the time between mixing of Components A and B and beginning of expansion reaction.
-- Expansion ratio determined by comparing densities of liquid foam and expanded foam; liquid density was not measured for RR401 or RR401G; instead, 72.0 pcf was used based on Gurtowski et al. (2016).
-- FI-10S results from Gurtowski et al. (2016) are reported.

Recall that the RR401 and RR401G foams were tested solely to evaluate their moisture sensitivity. Otherwise, neither are ideal products for ADR operations. Compared to FI-10S in Table 4.2, they react very quickly (about 30 sec compared to 5 min), provide approximately half the density (and double the expansion ratio), and yield around 100 psi compressive strength instead of 300 psi. FI-10S has performed favorably primarily because it has a slower (approximately 5 min) reaction time that allows placement of large volumes of material in craters and also reasonable compressive strength. If RR401G was demonstrated to be moisture

insensitive, ERDC would attempt to work with HMI to apply the same gas-blown technology to a higher-density foam (i.e., higher compressive strength) with a slower reaction time.

Figure 4.2 presents RR401 and RR401G data graphically. The two products yielded similar UCS in both the dry or wet state. For the damp (wet sand) condition, RR401G provided slightly more than three times the UCS than RR401. However, as shown in Figure 4.2b, the reduction in UCS was still meaningful at essentially 75%. UCS reduction for the other three cases ranged from 89 to 93% (8 to 13 psi), which was on the order of the UCS reduction observed for FI-10S (95%).

Figure 4.2. HMI foam compressive strengths for various moisture conditions.

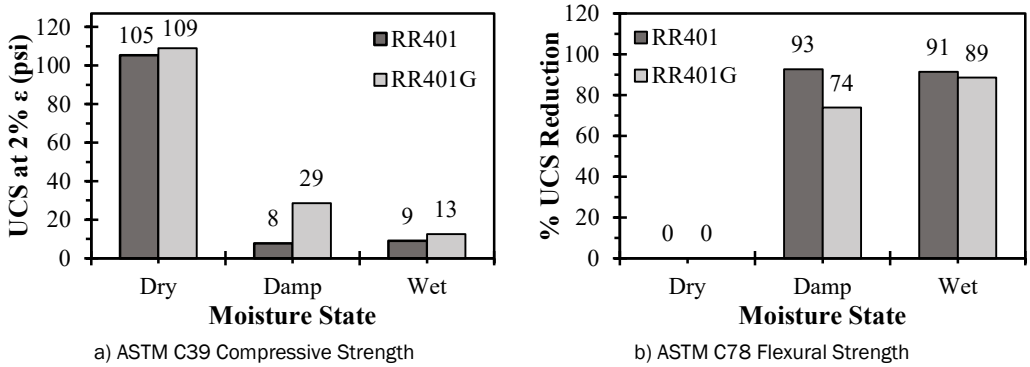

a) ASTM C39 Compressive Strength

b) ASTM C78 Flexural Strength

Based on these results, if a gas-blown formulation was produced for a higher-density foam targeting 300-psi strength, a 75% reduction in UCS would yield 75 psi compressive strength. While this is an improvement, a UCS value this low would still be of concern in terms of using it for repairs conducted to support aircraft. Ultimately, the investigation of the gas-blown foam did not lead to a viable alternative to FI-10S, which has become the primary foam for ADR.

5 Void Characterization Results

5.1 Laboratory void characterization

All void characterization tools were evaluated in the laboratory except for the C-ALS and the SVS Camera. Detailed measurements of Models 1 and 2 were recorded prior to placing the plywood covering over the models. These measurements were used to recreate the model in AutoCAD and AutoCAD Civil 3-D in order to obtain reliable estimates of void volume for comparison to the void characterization techniques presented in Section 3.3. Volumes from these renderings are referred to as true volumes in this report, but it should be acknowledged that these are still somewhat approximate. Figure 5.1 illustrates the renderings produced in AutoCAD for the two physical models. Other drawings were created as necessary to appropriately characterize the models.

Figure 5.1. Rendering of AutoCAD models relative to physical models.

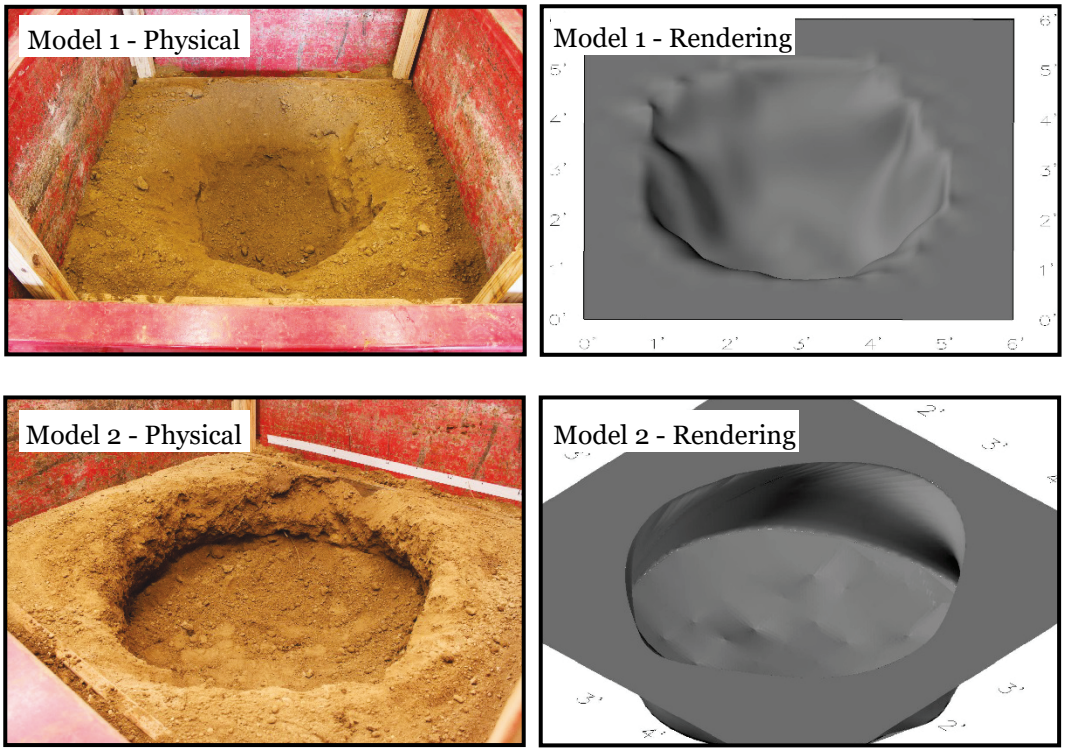

Recall that Models 1 and 2 were used to refine void characterization techniques prior to field testing and were constructed to have different profiles (crater vs. semi-spherical) since the actual camouflet shape that would be encountered was not known with any confidence. For this reason, the methods used to analyze void characterization data differ

between Models 1 and 2. The method believed to be most appropriate for each model was selected as discussed in the following two sections.

5.1.1 Model 1

For Model 1, most analysis was performed in AutoCAD Civil 3D using tools typical for creating contour surfaces and maps from survey points. This approach was selected because the profile of Model 1 was well-suited to be analyzed as a surveyed surface since, for any *x*-*y* coordinate, there was only one elevation (*z* coordinate). This is in contrast to Model 2 where there could be multiple elevations at a given *x*-*y* coordinate (such as in a wall-overhang area) as is discussed in Section 5.2. Analysis for MC1 borescope data was conducted in Agisoft PhotoScan (photogrammetry software). Table 5.1 provides Model 1 results. Model 1's true volume as estimated in AutoCAD Civil 3D was 12.4 ft^3. This number was used as the reference for other comparisons.

Table 5.1. Model 1 void characterization results.

Measurement Type	Measurement Details	Analysis Type	Analysis Details	Calculated Volume (ft^3)
True Volume	--	AutoCAD Civil 3D	--	12.4
MC1 Borescope	Recorded Video	PhotoScan	--	n/a
MLRF	Readings at 22.5° Intervals	AutoCAD Civil 3D	--	12.2
	Readings at 45° Intervals	AutoCAD Civil 3D	--	12.0
	Readings at 90° Intervals	AutoCAD Civil 3D	--	10.9
Uniprise Tubing	Readings at 90° Intervals	AutoCAD Civil 3D	Assumed horizontal dimensions were equal to diagonal readings	7.5
		AutoCAD Civil 3D	Assumed horizontal dimensions were 25% greater than diagonal readings	9.9
Loc-Line Tubing	Readings at 90° Intervals	AutoCAD Civil 3D	Assumed horizontal dimensions were equal to diagonal readings	8.9
		AutoCAD Civil 3D	Assumed horizontal dimensions were 25% greater than diagonal readings	11.7
Plumb Bob	--	Equation	Assumed shape is a half sphere	7.7
		Equation	Assumed shape is a spherical cap with radius 40% greater than depth	13.2

-- No volume was able to be calculated from MC1 borescope imagery using photogrammetry techniques.

Figure 5.2 shows the type of image quality the MC1 borescope provided. When the MC1's integrated LED light source was used, the MC1 probe tip had to be within a few inches of the surface it was viewing, and, even still, image quality was poor as shown in Figure 5.2a. With the supplementary light source (Figure 5.2b), images improved considerably, and the MC1 camera could view surfaces from farther away. However, contrast within the MC1's pictures was mediocre. While various large features could be observed, detail was lacking.

Figure 5.2. MC1 borescope photo of Model 1.

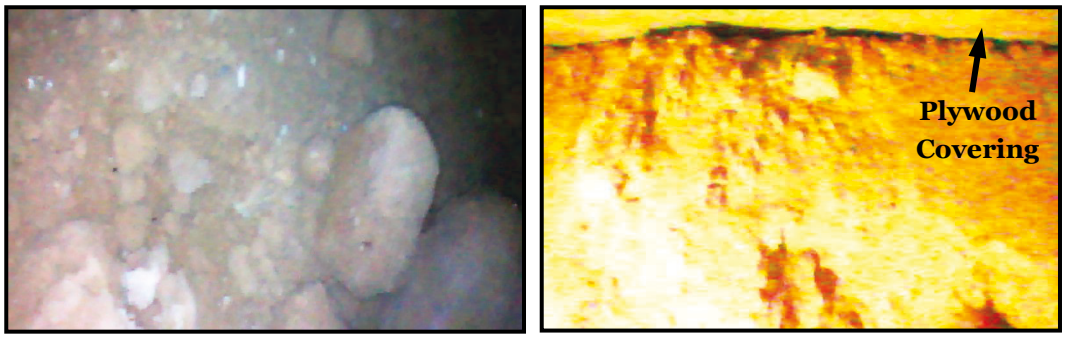

a) Using MC1 light source b) Using supplementary light source

Typically, video was recorded with the MC1, and still images were later extracted from the video with post-processing software. These images were loaded into PhotoScan and processed to investigate whether or not a point cloud could be constructed for determining volume given the image quality. Figure 5.3 displays the point cloud model developed by PhotoScan. Despite heavy image overlap, the MC1 camera simply was not able to provide images with the resolution and quality to fully distinguish features inside the camouflet so that PhotoScan could stitch the images into a logical point cloud. Most notably, it appeared as if PhotoScan did not detect the crater shape of Model 1 as the point cloud was effectively a flat surface; this is likely a result of the poor image quality. Overall, using the MC1 for photogrammetry with Model 1 was not successful; however, it was useful in a general sense for inspecting the camouflet visually so long as an additional light source was used.

Figure 5.3. PhotoScan point cloud of Model 1 with the MC1 borescope.

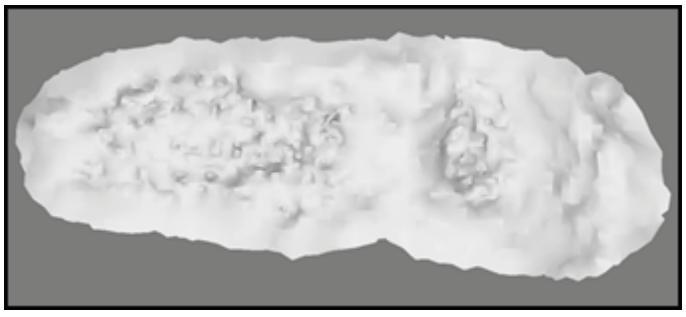

Figure 5.4 illustrates the analysis process for the MLRF using AutoCAD Civil 3D for radial measurement intervals of 22.5° (33 total measurements), 45° (17 total measurements), and 90° (9 total measurements). The MLRF analysis using all 33 measurements at 22.5° increments yielded a volume of 12.2 ft^3, which is nearly that of the true volume. As fewer measurements were considered, resolution decreased and details were lost as shown in Figure 5.4. Volume also decreased to as low as 10.9 ft^3.

Figure 5.4. Model 1 drawings based on the MLRF.

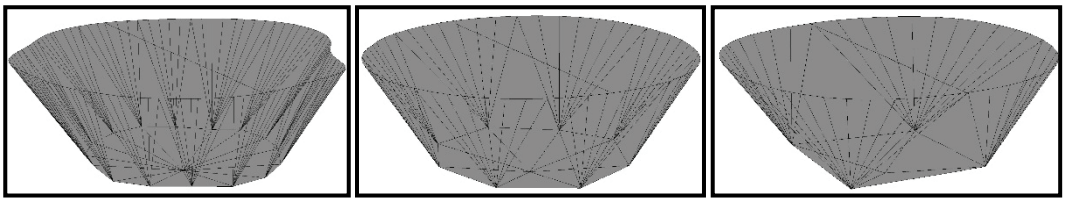

a) 22.5° radial intervals b) 45° radial intervals c) 90° radial intervals

Figure 5.5 illustrates the analysis process for the Uniprise tubing where 4 width measurements at 90° radial increments and 1 depth measurement were taken. The diagonal arrow "*a*" drawn in Figure 5.5 corresponds to the value measured with the Uniprise tubing. In the analysis, it was simplified and assumed that Uniprise measurements were at 45°. Two analyses were conducted where it was assumed that the horizontal radius of the camouflet was also equal to "*a*" or was some value larger than "*a*" (i.e., 1.25*a*). Both approaches were approximate. The 1.25 multiplication factor for "*a*" was determined by calculating the average ratio of horizontal (0°) to diagonal (45°) MLRF measurements. Volumes for the *a* and 1.25*a* analyses were 7.5 and 9.9 ft^3, respectively. Both were low relative to the true volume, but multiplying *a* by a factor was more appropriate than not.

Figure 5.5. Model 1 drawings based on the Uniprise tubing.

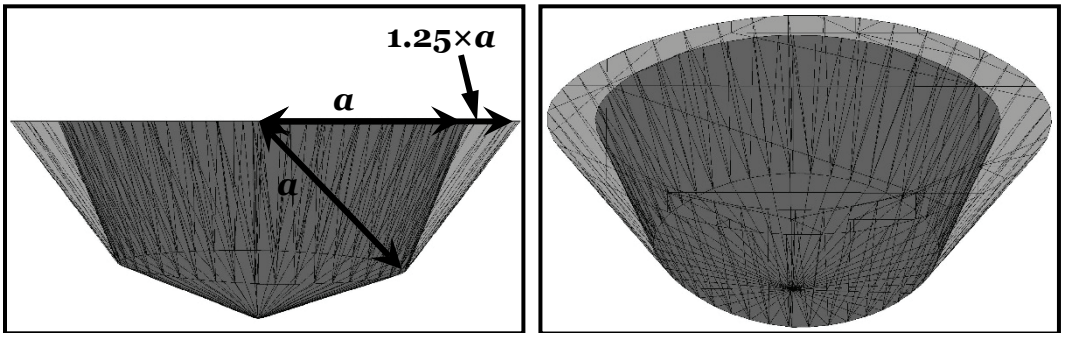

a) Side view b) Angled view

Figure 5.6 illustrates the analysis process for the Loc-Line tubing that was identical to that of the Uniprise tubing. Results were similar in that two variations were considered. In this case, the smaller analysis yielded 8.9 ft^3 while the larger variation, at 11.7 ft^3, yielded a volume much closer to the true volume.

Figure 5.6. Model 1 drawings based on the Loc-Line tubing.

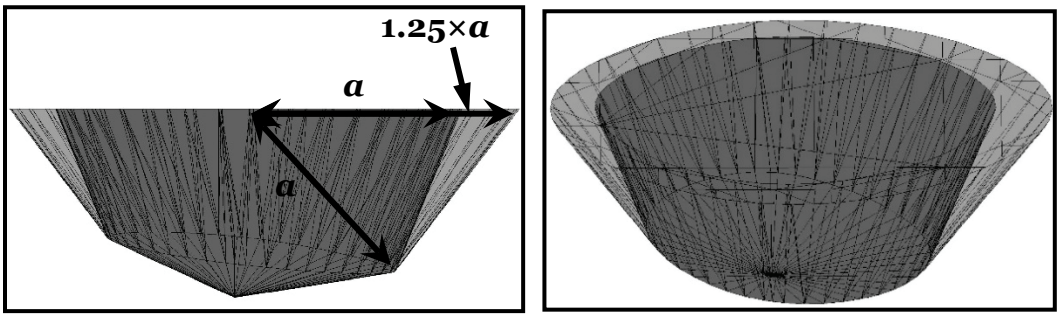

a) Side view b) Angled view

Figure 5.7 illustrates analysis conducted using depth obtained from a plumb bob. For comparison, volume was calculated two ways. First, it was assumed that the general shape of Model 1 could be characterized by a half sphere. This approach yielded a volume of 7.7 ft^3. Second, it was assumed that the general shape of Model 1 could be characterized by a spherical cap, which is a portion of a sphere (volume is calculated by Equation 5.1). The spherical cap radius was assumed to be 1.40 times the depth based on the ratio of radius to depth for MLRF measurements. This approach yielded a volume of 13.2 ft^3, which was more in line with the true volume but slightly larger (a more conservative estimate given the volume would be used to plan the amount of fill material required).

Figure 5.7. Differences between Model 1 Plumb Bob analysis methods.

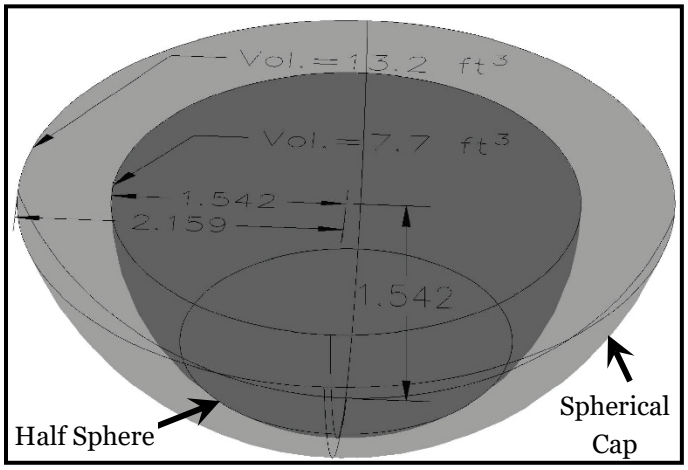

Overall, the MLRF yielded the best approximation of the true volume in a predictable way. While the enlarged Loc-Line volume and the plumb bob spherical cap volume were within reason compared to the true volume, their calculations relied on data that were known only because of the MLRF. The considerable difference between the Loc-Line and Uniprise tubing volumes was not expected since they are quite similar to each other

and the reason for this discrepancy is not known. Their difference in volume despite their similarity physically does raise some concern as to the repeatability of measurements with this type of tool. In summary, Model 1 demonstrated that the MLRF can, with many measurements, provide the most accurate volume estimate for a crater-shaped camouflet, the MC1 borescope uses are limited, and the more crude techniques (Loc-Line tubing, Uniprise tubing, and plumb bob) can, with additional assumptions, provide reasonable volumes in some cases.

$$V = \frac{\pi}{6} H\left(3A^2 + H^2\right) \tag{5.1}$$

Where

V = volume of a spherical cap (ft^3)
H = total depth of camouflet (ft)
A = radius at the base of spherical cap (i.e., widest radius) (ft)

5.1.2 Model 2

For Model 2, most of the analysis was performed in AutoCAD using 3-D modeling tools to create lofted surfaces, which are essentially best-fit surfaces with respect to several reference points (i.e., distance measurements in this case). This approach was selected because, for Model 2, there could be multiple elevations at a given *x*-*y* coordinate (such as in a wall overhang area). In that case, the contoured surface procedures in AutoCAD Civil 3D used for Model 1 are not applicable. As with Model 1, analysis for MC1 borescope data was attempted in Agisoft PhotoScan (photogrammetry software). Table 5.2 provides Model 2 results. Model 2's true volume was estimated to be 18.8 ft^3. This number was used as the reference for other comparisons.

MC1 borescope video was collected and processed following the same procedures as with Model 1. PhotoScan again had difficulty in stitching the extracted images together to form a full point cloud; images lacked the quality needed for PhotoScan to detect points on unique features for matching overlapping images. Figure 5.8 shows the resulting point cloud model, which was improved compared to Figure 5.3 but not complete.

Table 5.2. Model 2 void characterization results.

Measurement Type	Measurement Details	Analysis Type	Analysis Details	Calculated Volume (ft^3)
True Volume	--	AutoCAD (Loft Surfaces)	--	18.8
MC1 Borescope	Recorded Video	PhotoScan	--	n/a
MLRF	Readings at 22.5° Intervals	AutoCAD (Loft Surfaces)		15.8
	Readings at 45° Intervals	AutoCAD (Loft Surfaces)	--	15.7
	Readings at 90° Intervals	AutoCAD (Loft Surfaces)	--	14.5
Uniprise Tubing	Readings at 90° Intervals	AutoCAD (Loft Surfaces)	Used standard AutoCAD settings for the lofted surface	11.7
		AutoCAD (Loft Surfaces)	Added a bulge factor to the lofted surface	15.8
Loc-Line Tubing	Readings at 90° Intervals	AutoCAD (Loft Surfaces)	Used standard AutoCAD settings for the lofted surface	11.6
		AutoCAD (Loft Surfaces)	Added a bulge factor to the lofted surface	15.7
Plumb Bob	--	Equation	Assumed shape is a sphere	2.3
		Equation	Assumed shape is an ellipsoid with radius 25% greater than depth	14.4

-- No volume was able to be calculated from MC1 borescope imagery using photogrammetry techniques.
-- The bulge factor was added by setting the surface normal properties of the lofted surface to draft angles of 0° and draft magnitudes of 10.

Figure 5.8. PhotoScan point cloud of Model 2 with the MC1 borescope.

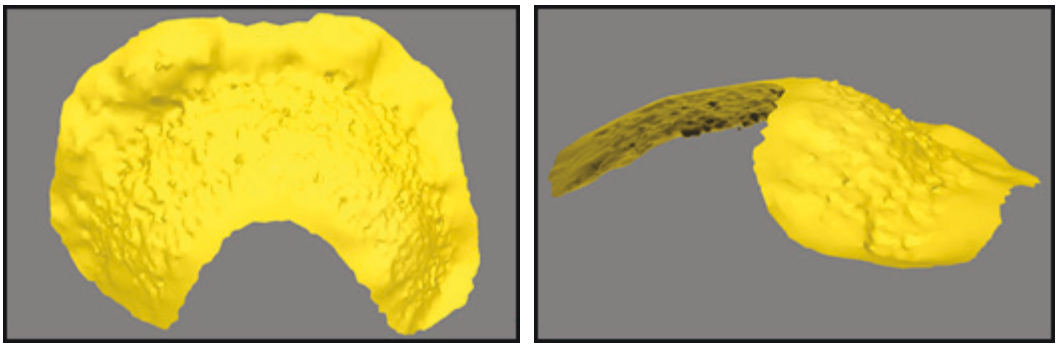

a) Top view b) Angled view

It was also interesting that PhotoScan, based on the lighting it gave the model, processed the images in an inverted fashion. Rather than portraying the model as a crater-like shape, PhotoScan assumed it was a mound-like shape as shown in Figure 5.8b. This is perhaps because PhotoScan was likely developed to process images under the assumption an item is being photographed from its exterior. With the camouflets, a camera is effectively being inserted into the item, and the item is being imaged from the inside, which confuses PhotoScan.

Figure 5.9 illustrates the resulting drawings based on the MLRF measurements for radial measurement intervals of 22.5° (33 total measurements), 45° (17 total measurements), and 90° (9 total measurements). The resulting shapes resemble a somewhat irregular ellipsoid. However, it does resemble the semi-spherical shape of Model 2.

Figure 5.9. Model 2 drawings based on the MLRF (top: side view, bottom: top view).

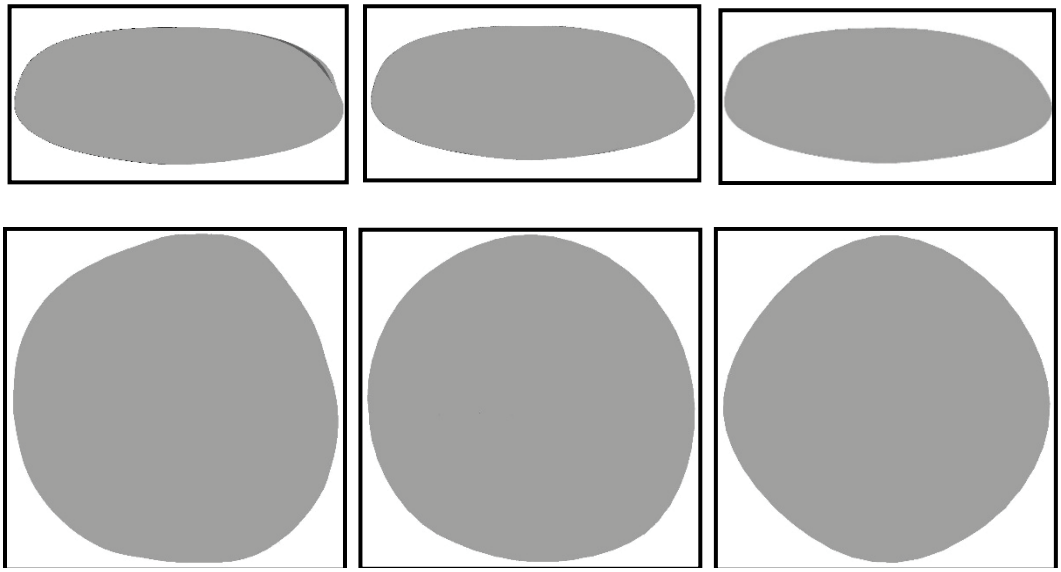

a) 22.5° radial intervals b) 45° radial intervals c) 90° radial intervals

As with Model 1 MLRF results, detail was lost as fewer measurements were considered. Volume was 15.8 ft^3 for the 22.5° interval drawing, and it decreased slightly with fewer MLRF measurements similarly to Model 1.

Note that the largest MLRF volume was 3 ft^3 less than the true volume, primarily because the roof of Model 2 was flat plywood and had no curvature like the top of the MLRF drawings. Additionally, the sidewalls of Model 2, although they had some overhang, were essentially vertical or sloped outward near the plywood covering. Figure 5.10 illustrates this error. The total estimate of volume error was 2.7 ft^3, which would nearly account for the 3 ft^3 difference between true and MLRF volumes. This type of error would likely be a smaller issue for an actual camouflet.

Figure 5.10. Illustration of Model 2 volume error.

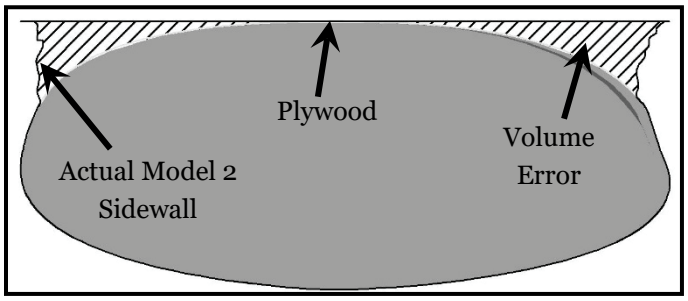

Figure 5.11 illustrates the analysis process for the Uniprise tubing. As with Model 1, one depth measurement and four width measurements were taken at 90° radial increments. Efforts were made when taking width measurements to measure the widest point in the camouflet. In terms of analyzing measurements in AutoCAD, all width measurements were assumed to have been located at the mid-depth of the model. As shown in Figure 5.11, the standard drawing does not seem to approximate Model 2 very well (i.e., the volume error in Figure 5.10 would be even larger). In contrast, adding the bulge factor as described in the footnote of Table 5.2 considerably improved the drawing, resulting in a volume of 15.8 ft^3 similar to the best MLRF value.

Figure 5.11. Model 2 drawings based on the Uniprise tubing.

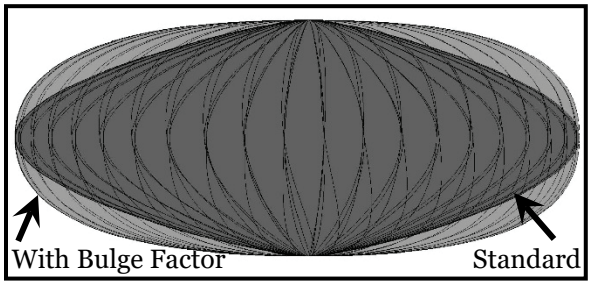

As with Model 1, Loc-Line tubing measurements and drawings were obtained exactly as they were with the Uniprise tubing. Figure 5.12 shows the final drawings of Model 2 using the Loc-Line tubing. Volumes for the standard and bulged drawings, at 11.6 and 15.7 ft^3, respectively, were effectively identical to those of the Uniprise tubing.

Figure 5.12. Model 2 drawings based on the Loc-Line tubing.

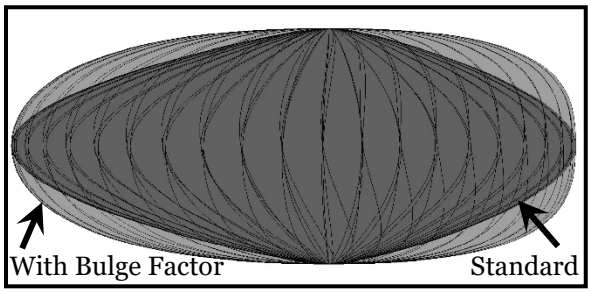

For the plumb bob, the only measurement is depth, meaning the only volume that can be calculated, if no other information is known and no other assumptions are made, is that of a sphere. Figure 5.13 shows how much error can be associated with assuming a sphere if the true shape is an ellipsoid like Model 2. The spherical volume was only 2.3 ft^3.

To calculate volume as an ellipsoid instead of a sphere, some information must be known about overall camouflet width. For Model 2, the ratio of radius to total depth was found to be about 1.25 from MLRF measurements. This was used to approximate a radius 25% greater than the measured plumb bob depth. This depth and radius were used in Equation 5.2 to calculate the volume of an ellipsoid, which was 14.4 ft^3 for Model 2.

Figure 5.13. Differences between Model 2 plumb bob analysis methods.

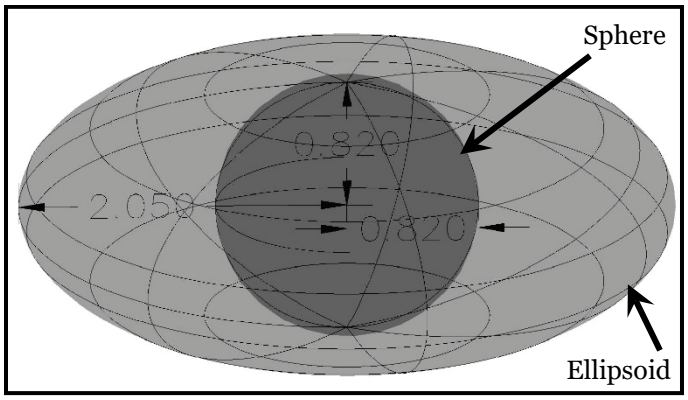

Considering the simplicity of the plumb bob and its single depth measurement, 14.4 ft^3 is not an unreasonable approximation when compared to the MLRF measurements, which required more time and analysis. If it was possible to determine some standard characteristics for actual camouflets (e.g., radius is generally 25% greater than depth) that either were similar to the general properties Bull and Woodford described or verified Bull and Woodfords' properties, the plumb bob could be a fairly useful and quick tool for estimating camouflet volumes.

$$V = \frac{4}{3}\pi\left(A^2 \frac{H}{2}\right) \quad (5.2)$$

Where

V = volume of an ellipsoid (ft^3)
H = total depth of camouflet (ft)
A = radius of camouflet (ft)

Overall, the MLRF provided the closest approximation to the true volume with no additional adjustments made, especially when the volume error was considered. When adjustments were made to the Uniprise and Loc-Line tubing estimates, they were as suitable as the MLRF estimate. When Model 2 was estimated as an ellipsoid, the plumb bob provided an adequate volume approximation considering how simple, quick, and inexpensive it is; however, this did require some assumption to be made about dimensional ratios of the camouflet. As with Model 1, the MC1 borescope was somewhat useful in terms of viewing the camouflet void, but it was not successfully used to estimate volume.

5.1.3 Summary of laboratory void characterization

It is useful to remember that the primary purpose of the laboratory void characterization trials was to begin to develop and refine measurement and analysis procedures for each technique using camouflet shapes that might be encountered in the field. The laboratory void characterization did not attempt to really compare one technique to another. It also did not investigate the possibility of determining scaling or correction factors to correct volumes from simpler techniques (e.g., plumb bob) to volumes from more robust techniques (e.g., MLRF at 22.5° measurement intervals). This was mostly for two reasons: (1) it was not known with any confidence prior to the field work what a typical camouflet shape might be, and (2) it was not known if actual camouflet shape characteristics would vary considerably or if all camouflets would have a fairly standard shape.

5.2 Field void characterization

At Silver Flag, all void characterization techniques discussed in Section 3.3 were used to assess camouflets. The field offered an advantage in the fact that considerable replication was available with 11 camouflets. The results for any given technique are discussed for all camouflets simultaneously

(rather than individually as was the case with the laboratory models). Discussion is organized as follows: C-ALS results, visual technique results (i.e., MC1 borescope and SVS camera), discrete technique results (e.g., MLRF and plumb bob), and, finally, a summary of all techniques in the context of Camouflet 12 that was used for destructive void characterization.

5.2.1 Cavity auto laser scanner results

Table 5.3 provides volumes for Camouflets 1 to 12 (excluding 9) for both horizontal and vertical scans. As discussed in Section 3.3.1, most scans were conducted at a 3° scan resolution, but additional scan resolution angles were also investigated for Camouflet 7 and 12. In general, the C-ALS data, specifically for the 3° scan resolution, was considered to provide the "true" volume of a camouflet similar to the detailed survey measurements for the laboratory Models 1 and 2. The C-ALS ultimately served two main purposes; it provided a detailed volume estimate and also a visual depiction of the camouflet shape.

Table 5.3. C-ALS volumes for Silver Flag camouflets.

		Horizontal Scans		Vertical Scans		Average Volume (ft^3)
Series	Camouflet	Resolution	Volume (ft^3)	Resolution	Volume (ft^3)	
A	1	3	7.1	3	8.9	8.0
	2	3	14.9	3	14.5	14.7
	3	3	14.3	3	14.6	14.4
B	4	3	13.7	3	13.6	13.7
	5	3	19.0	3	19.1	19.0
	6	3	20.3	3	20.6	20.4
C	7	3	10.1	3	10.4	10.2
		10	10.2	10	9.3	9.8
		20	8.4	20	9.1	8.7
		25	7.9	25	9.2	8.5
	8	3	11.5	3	12.2	11.8
D	10	3	11.0	3	11.6	11.3
	11	3	7.6	3	7.8	7.7
DVC	12	1	—	1	—	—
		3	1.7	3	2.3	2.0
		5	1.4	5	2.1	1.7
		10	1.3	10	2.1	1.7
		25	1.2	25	2.0	1.6

Figure 5.14 illustrates the difference between horizontal C-ALS scans and vertical scans (the point cloud coloring is by depth). Horizontal scans produce a series of rings, while vertical scans produce vertical pie slices. In

general, vertical scans required slightly more time because it took additional sweeps of the C-ALS head to complete a full coverage with the vertical pattern than with the horizontal pattern.

Both vertical and horizontal scans were always conducted for each camouflet because, although not very likely at higher scan resolutions (i.e., smaller scan resolution angles), one could detect a feature the other missed, and vice versa. As a result, Table 5.3 volumes for horizontal and vertical scans differed slightly although these differences were relatively minor. Figure 5.15 shows that, on average, vertical and horizontal scans yielded practically the same volume. For discussion purposes, the average volume was reported and is used as the reference.

Figure 5.14. Comparison of C-ALS horizontal and vertical scans for Camouflet 1.

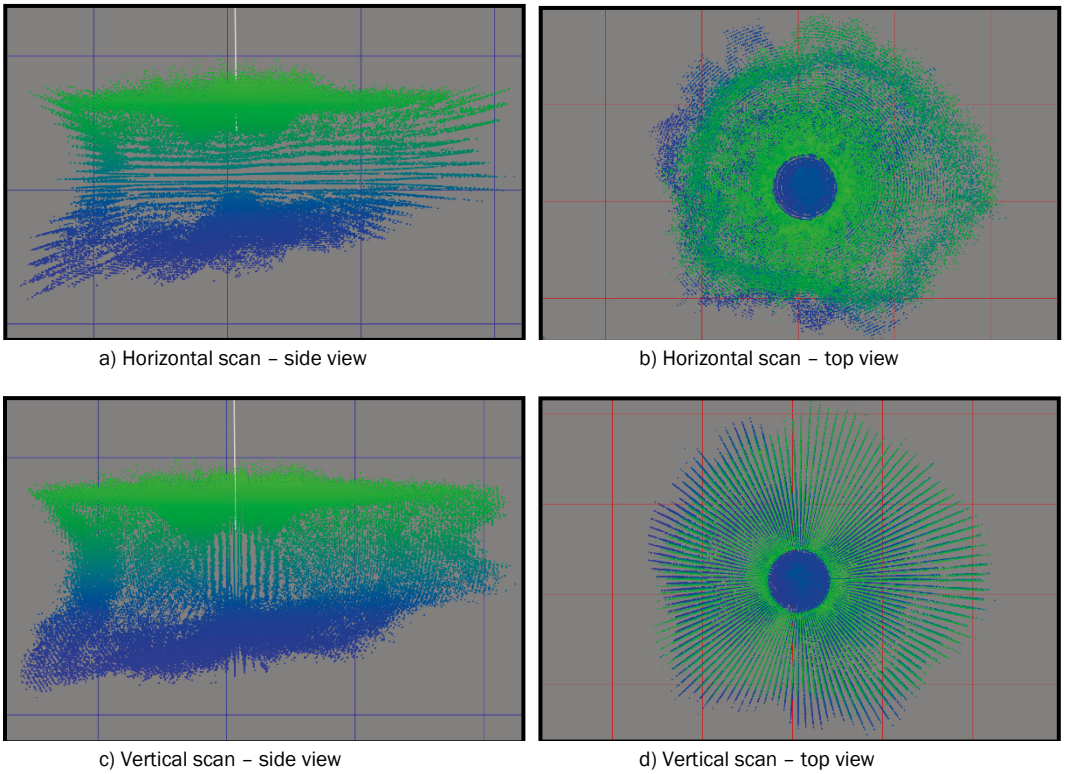

a) Horizontal scan – side view

b) Horizontal scan – top view

c) Vertical scan – side view

d) Vertical scan – top view

Figure 5.15. Equality plot comparing C-ALS horizontal and vertical scans.

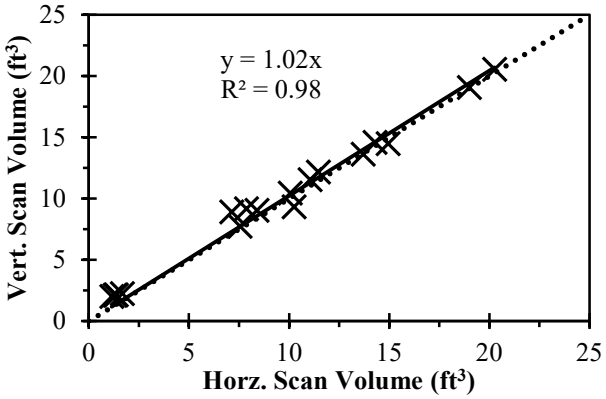

Table 5.3 volumes appeared to be within reason based on the general expectation of camouflet sizes. Camouflet 12 volume at 2.0 ft^3 was uniquely small relative to the other camouflets. This is thought to be partially due to the blasting issues encountered when creating the camouflets. Recall Section 3.4.2 where blasting procedures were described; in the iterative approach used to determine the final C-4 charge size, Camouflet 12 was blown in the first iteration with 3 blocks of C-4. Although 2 blocks were ultimately selected for most camouflets, Camouflets 10 to 12 were located in the 16-in. concrete section of the runway, and 3.5 and 4 blocks of C-4 were used for Camouflets 10 and 11. Thus, comparatively, the charge for Camouflet 12 was weaker. The fact that Camouflet 12 was so much smaller led to it being selected for DVC. Though ideally all camouflets, both those being repaired and the one used for DVC, would be similar in size, it was deemed of greater priority to have all camouflets slated for repairs be approximately the same size.

As scan resolution decreased (i.e., scan resolution angle increased) for Camouflets 7 and 12, the calculated volume decreased slightly, which was expected for the same reason that MLRF volumes in the laboratory trials decreased with increasing radial measurement increments. Figure 5.16 depicts volume decreasing (relative to the 3° scan resolution) as scan resolution angle increases. The overall trend is the same for both Camouflets 7 and 12. On average, the 10° scan resolution yielded around 90% of the 3° scan resolution volume, and the 20° scan resolution yielded around 85%.

Figure 5.16. Effect of C-ALS scan resolution on volume.

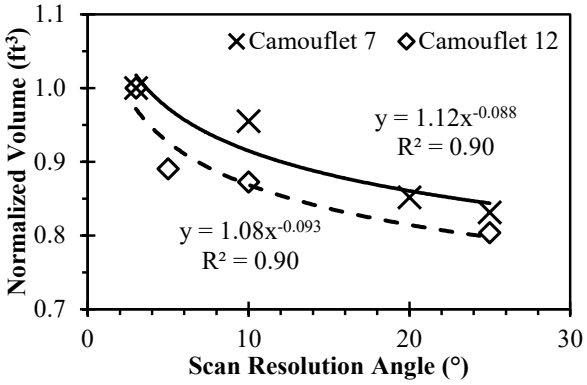

Despite the loss in accuracy with lower scan resolutions, time required to conduct scans also decreased, which is generally of importance. Table 5.4 provides scan time data for all scan resolutions tested. For the 1° scan resolution, scans were not conducted to completion, which is why estimated time is shown. Instead, the C-ALS software tracks the scan progress, so time to complete 50% of the scan was measured and then doubled. On average, scans at a 3° resolution took about 10 min each, while scans at a 25° resolution took about 2 min each. Given the fairly decent trend between volume accuracy and scan resolution, faster scans at a lower resolution could be conducted and scaled by a correction factor (if this device is used again in a more practice-oriented setting).

Table 5.4. C-ALS scan times for various scan resolutions.

Scan Resolution (°)	Scan Times for Camouflet 7 (mm:ss)		Scan Times for Camouflet 12 (mm:ss)		Average Scan Time (mm:ss)
	Horizontal	Vertical	Horizontal	Vertical	
1	--	--	~20:30	~40:00	~30:00
3	8:59	11:18	8:52	11:09	10:00
5	--	--	5:55	7:03	6:30
10	3:29	4:06	3:27	4:06	4:00
20	2:22	2:34	--	--	2:30
25	1:57	2:20	2:18	2:20	2:00

-- Average scan times rounded to nearest 30 second increment.

Figure 5.17 provides images of C-ALS scans for Camouflet Series A which have been surfaced for volume calculations. Three views are shown for each camouflet illustrating the considerable variations in shape between camouflets but also within a single camouflet. Camouflets created at Silver Flag in general exhibited more of an ellipsoidal shape than the almost spherical shape described by Bull and Woodford.

Figure 5.17. C-ALS surfaced scans for Camouflet Series A.

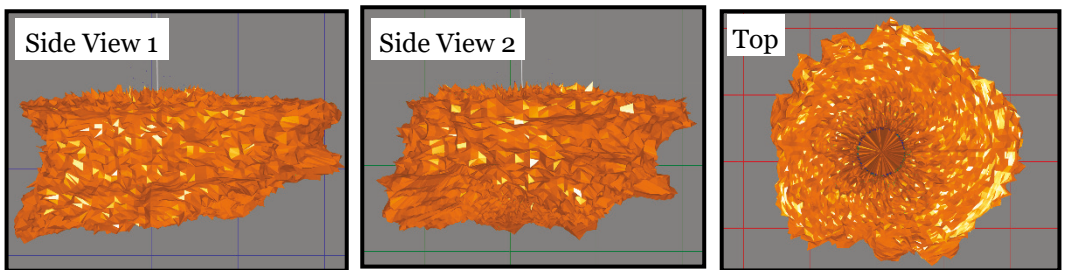

a) Camouflet 1

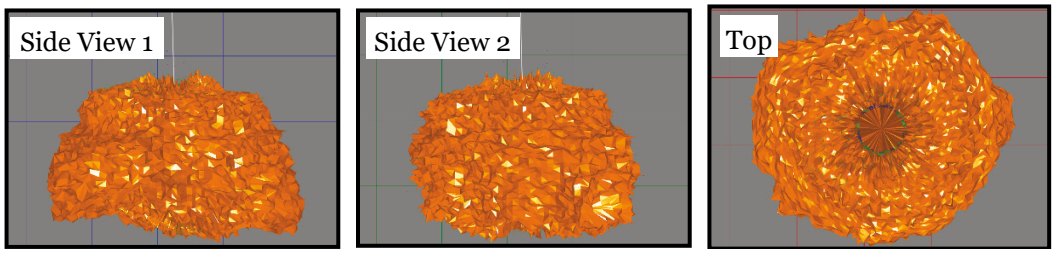

b) Camouflet 2

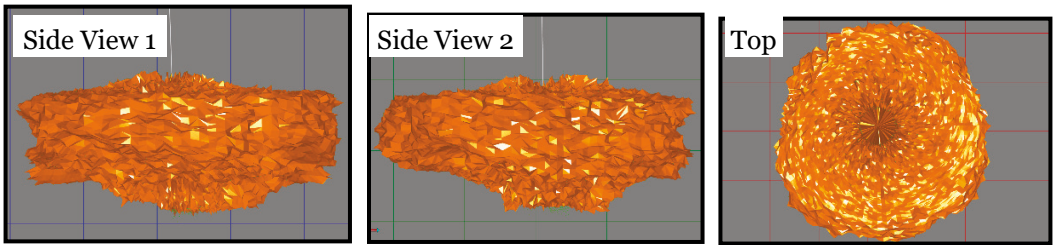

c) Camouflet 3

Figure 5.18 provides side-view images of C-ALS scans at a 3° scan resolution for all camouflets besides Camouflet 12 (i.e., all camouflets that were repaired). Both horizontal and vertical scans are turned on in Figure 5.18. For reference, the grid lines in Figure 5.18 are set to a 1-ft spacing.

Figure 5.18. C-ALS side view scans showing variability for Camouflet Series A to D.

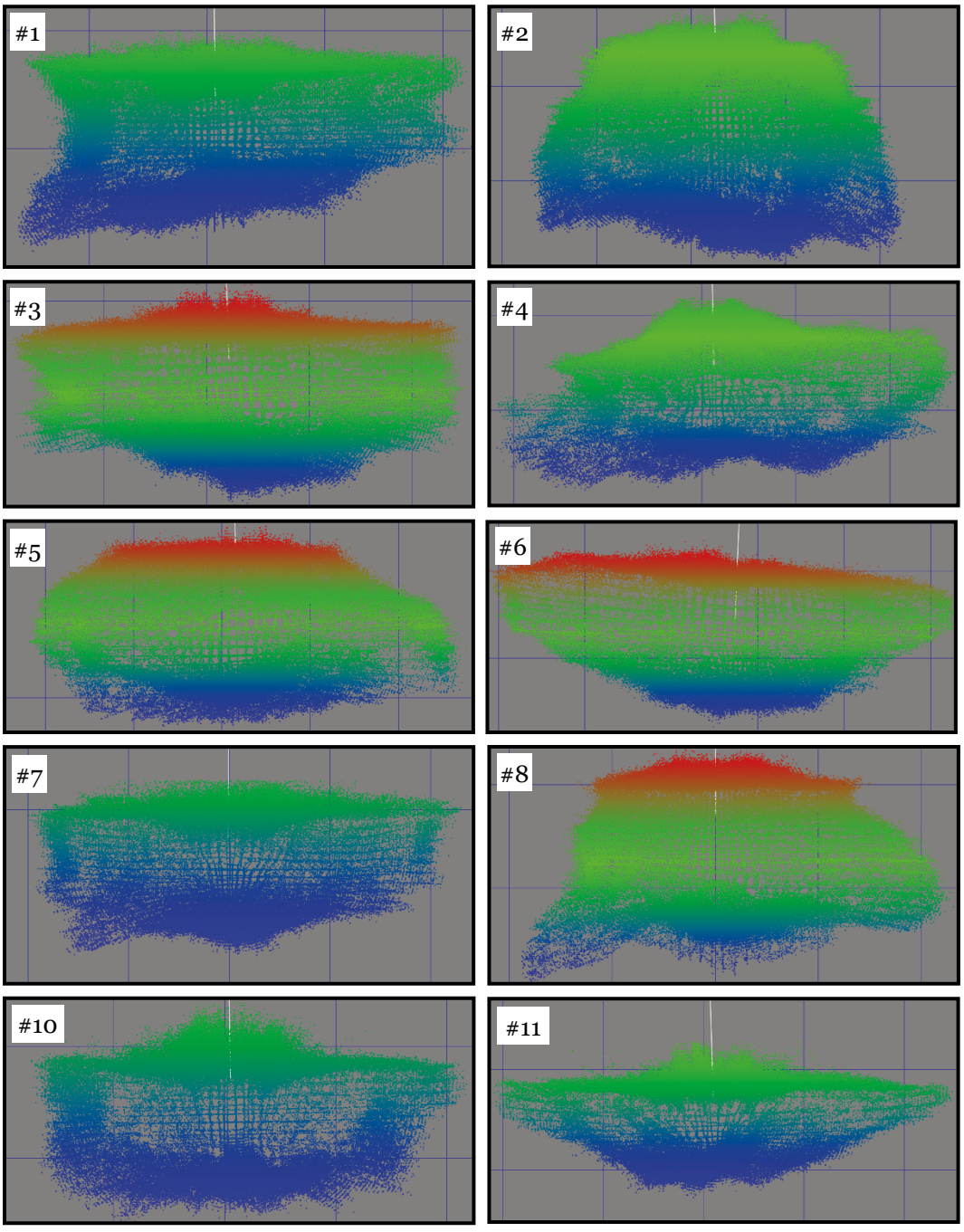

The primary purpose of Figure 5.18 is to further illustrate the variability in shapes between camouflets. In reality, both of the laboratory model shapes were observed in the Silver Flag camouflets. For example, Camouflets 6 and 11 resembled the crater-like shape of Model 1 while Camouflets 2, 5, and 8 resembled the spherical or ellipsoidal shape of Model 2. There was still a great deal of variation among these general classifications though; in

general, if one shape was to be selected, an ellipsoidal shape likely best represents the entire group of camouflets collectively.

Overall, the C-ALS appeared to work well for providing a visual depiction of each camouflet. It should be noted that these camouflets were very small with respect to the typical uses of the C-ALS. For example, Table 3.5 specifies the C-ALS laser range as 1.6 to 490 ft. Therefore, the C-ALS was operating at the very low end of its range, in which case noticeable scatter can be produced that is greater than the normal noise produced by the C-ALS. This is visible to an extent in Figures 5.15 and 5.18. In theory, the scatter should have minimal effects on volume calculations because it is being averaged in the surfacing process. This made the direct measurement of Camouflet 12 during DVC important for C-ALS verification purposes and is discussed in Section 5.2.4. Regardless of the accuracy of volume calculations, the C-ALS seemed suitable for visually characterizing camouflets.

5.2.2 Visual characterization technique results

Visual characterization techniques included the MC1 borescope and the SVS camera. These were techniques that provided video or still imagery as their only output data, which was then post-processed in attempts to extract camouflet volumes or other useful information.

The MC1 borescope was evaluated only on Camouflets 1 and 12. Based on laboratory testing with Models 1 and 2, it did not appear promising and was tested in the field in a limited manner. Figure 5.19 illustrates a typical photo taken by the MC1 in the Silver Flag camouflets. It is similar in quality to the laboratory model photo except more unique features exist. As with the laboratory testing, videos were recorded from which images were extracted and analyzed in Agisoft PhotoScan.

A point cloud was not able to be produced for Camouflet 1 using all of the images captured with the MC1 borescope largely because of the poor image quality. However, the analysis was attempted again with approximately 25% of the images, and PhotoScan was able to produce the point cloud model shown in Figure 5.20. This model represents the floor of the camouflet. Although the camouflet walls were not included, PhotoScan did show curvature to the camouflet floor. However, as with the laboratory MC1 testing shown in Figure 5.8, Figure 5.20 was also inverted.

Figure 5.19. MC1 borescope photo of Camouflet 1.

Figure 5.20. PhotoScan point cloud of part of Camouflet 1 with the MC1 borescope.

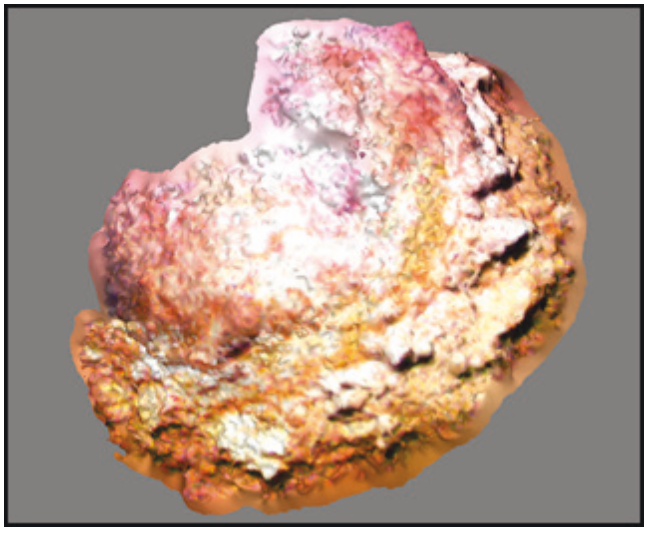

All images captured for Camouflet 12 were analyzed in PhotoScan, producing the point cloud model shown in Figure 5.21. The result was similar to that in Figure 5.8 where it seemed PhotoScan was not able to determine the location of each image and produced a horse shoe shaped model rather than a camouflet. As with Figure 5.8, PhotoScan also produced an inverted point cloud for Figure 5.21.

Overall, image quality in the field was similar to that in the laboratory except there were more unique identifying features in the field camouflets. In theory, this would have improved PhotoScan's ability to analyze the images and produce a point cloud. In general, this did not appear to be the case, most likely because of the poor overall image quality. As with the laboratory models, the MC1's primary use would be for visual void inspection over volume estimation, and, even so, it was still less than optimal.

Figure 5.21. PhotoScan point cloud of Camouflet 12 with the MC1 borescope.

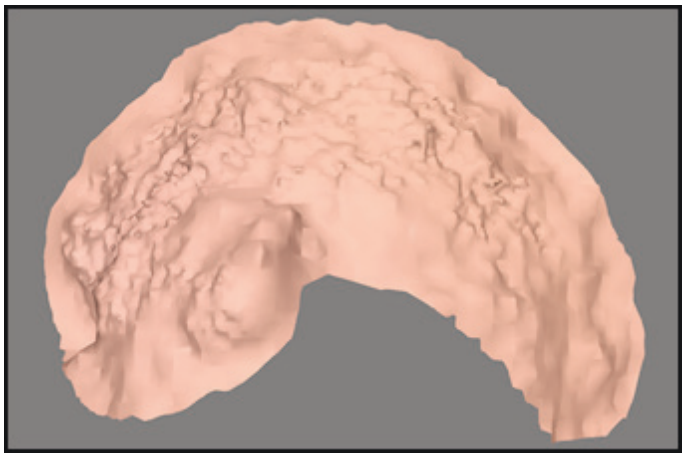

The SVS camera was evaluated only on Camouflets 2 and 12. Based on preliminary field tests, it did not appear promising and was tested in a limited manner similar to the MC1 borescope. Figure 5.22 illustrates a fair quality photo extracted from SVS video files. In comparison to the MC1 borescope, there was much greater definition, and the onboard light source was much better although it only illuminated part of the frame well. However, the overall SVS video quality was marginal, so most of the extracted images were blurred. SVS images were analyzed with PhotoScan identically to MC1 images.

Figure 5.22. SVS camera photo of Camouflet 2.

Figure 5.23 and Figure 5.24 show the point cloud models produced from SVS images for Camouflets 2 and 12, respectively. Effectively, no point cloud was able to be constructed for either camouflet. Only a few small blips of data were produced (note that Figure 5.23 and Figure 5.24 were zoomed in considerably).

Figure 5.23. PhotoScan point cloud of Camouflet 2 with the SVS camera.

Figure 5.24. PhotoScan point cloud of Camouflet 12 with the SVS camera.

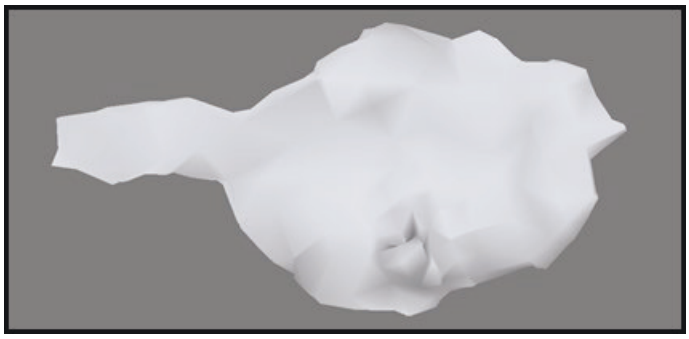

Overall, more in-depth analysis with the SVS camera was not feasible, and it was not successfully used for volume estimations. The image quality was, at its best, better than the MC1 borescope's image quality. However, the camera had to be held steady and moved quite slowly to obtain steady footage; if not, the resulting video footage was not very useful. Nonetheless, with the proper care, the SVS was somewhat useful for visual void inspections but not volume calculations.

5.2.3 Discrete characterization technique results

The four discrete characterization techniques included the MLRF, Uniprise tubing, Loc-Line tubing, and plumb bob. These were techniques that provided a limited number of measurements (i.e., discrete) of the inside of a camouflet that were then used to estimate camouflet volumes.

For the MLRF, the laboratory component demonstrated that, for a controlled scenario, the MLRF could approximate the true volume fairly well with 22.5° measurement intervals if volume error was considered. Field measurements were "practice oriented" in that they were intended to be simple and quick; therefore, MLRF measurements were taken only at 90° measurement intervals. Additionally, field camouflets, while generally ellipsoidal on average, were much more irregular than the controlled laboratory camouflets. These factors meant that the field camouflets did

not lend themselves well to producing the same type of AutoCAD models as produced for the laboratory camouflets (nor would this advanced level of analysis be desired in a practical setting). Since the capabilities of the MLRF were already demonstrated in the laboratory, the field investigation focused on simpler analysis methods. Ultimately, although multiple analysis methods were considered, only the most promising method considered is presented herein for brevity. This same approach (i.e., prioritizing simplicity) was applied to the other techniques as well.

Table 5.5 provides volume results for the four discrete characterization techniques. To compare these techniques, C-ALS volumes were used as the reference. Figure 5.25 shows the relationship between C-ALS volumes and Table 5.5 volumes for the four discrete techniques. Details regarding volume calculations for each technique are discussed in the following paragraphs.

Table 5.5. Discrete characterization technique volumes for Silver Flag camouflets.

Series	Camouflet	Volume (ft^3)						Volume Difference with respect to C-ALS (ft^3)			
		C-ALS	MLRF	Uniprise	Loc-Line	Plumb Bob		MLRF	Uniprise	Loc-Line	Plumb Bob
A	1	8.0	8.6	11.0	9.7	13.6		-0.6	-3.0	-1.7	-5.6
	2	14.7	10.3	16.6	15.3	18.6		4.4	-1.9	-0.6	-3.9
	3	14.4	8.0	16.9	14.7	30.5		6.4	-2.5	-0.3	-16.1
B	4	13.7	11.0	12.7	11.3	17.1		2.7	1.0	2.4	-3.4
	5	19.0	15.4	10.5	8.1	13.9		3.6	8.5	10.9	5.1
	6	20.4	17.1	16.4	14.5	6.8		3.3	4.0	5.9	13.6
C	7	10.2	10.0	10.3	10.7	5.3		0.2	-0.1	-0.5	4.9
	8	11.8	9.6	8.6	6.3	11.2		2.2	3.2	5.5	0.6
D	10	11.3	8.7	8.2	10.0	5.6		2.6	3.1	1.3	5.7
	11	7.7	6.6	6.6	5.4	3.2		1.1	1.1	2.3	4.5
DVC	12	2.0	2.9	7.4	7.0	11.7		-0.9	-5.4	-5.0	-9.7
Avg	**—**	**12.1**	**9.8**	**11.4**	**10.3**	**12.5**		**2.3**	**0.7**	**1.8**	**-0.4**
St. Dev.	**—**	**5.2**	**3.9**	**3.8**	**3.5**	**7.8**		**2.2**	**3.9**	**4.4**	**8.4**
COV (%)	**—**	**43**	**40**	**33**	**34**	**62**		**18**	**32**	**36**	**69**

-- MLRF volumes obtained using Equation 5.2 (ellipsoid), fixed angle mid-depth measurements, and plumb bob depth
-- Uniprise and Loc-Line volumes obtained using Equation 5.2 (ellipsoid) and plumb bob depth
-- Plumb bob volumes obtained using Equation 5.2 (ellipsoid) where radius (A) was 1.1 times the depth (H)
-- COV for volume differences with respect to C-ALS obtained by dividing St. Dev. by average C-ALS volume (12.1 ft^3)

MLRF volumes were calculated under the generalization that the camouflets were ellipsoids (Equation 5.2). Mid-depth measurements from the fixed-angle procedure were averaged and used as the ellipsoid radius, A, while the depth measured by the plumb bob was used as the ellipsoid depth, H. Measurements from the fixed-angle procedure were used because the fixed-depth procedure was deemed less appropriate. Even for camouflets that exhibited the Model 1 crater-type shape (e.g., Camouflet 11

in Figure 5.18), the ceiling of the camouflet was not necessarily level nor perfectly flat like the plywood in Model 1, which meant that the horizontal MLRF measurements usually reported a distance corresponding to a point somewhere on the camouflet ceiling rather than the full radius. This resulted in errors calculating the volume. This aspect of the camouflets also made the MLRF depth more difficult to determine, which is why plumb bob depths (minus the concrete thickness) were used for the depth measurement for all four characterization techniques. The average MLRF volume for all camouflets was 9.8 ft^3, which, compared to the C-ALS volume of 12.1 ft^3, was 2.3 ft^3 less.

Figure 5.25. Relationship between C-ALS and discrete technique volumes.

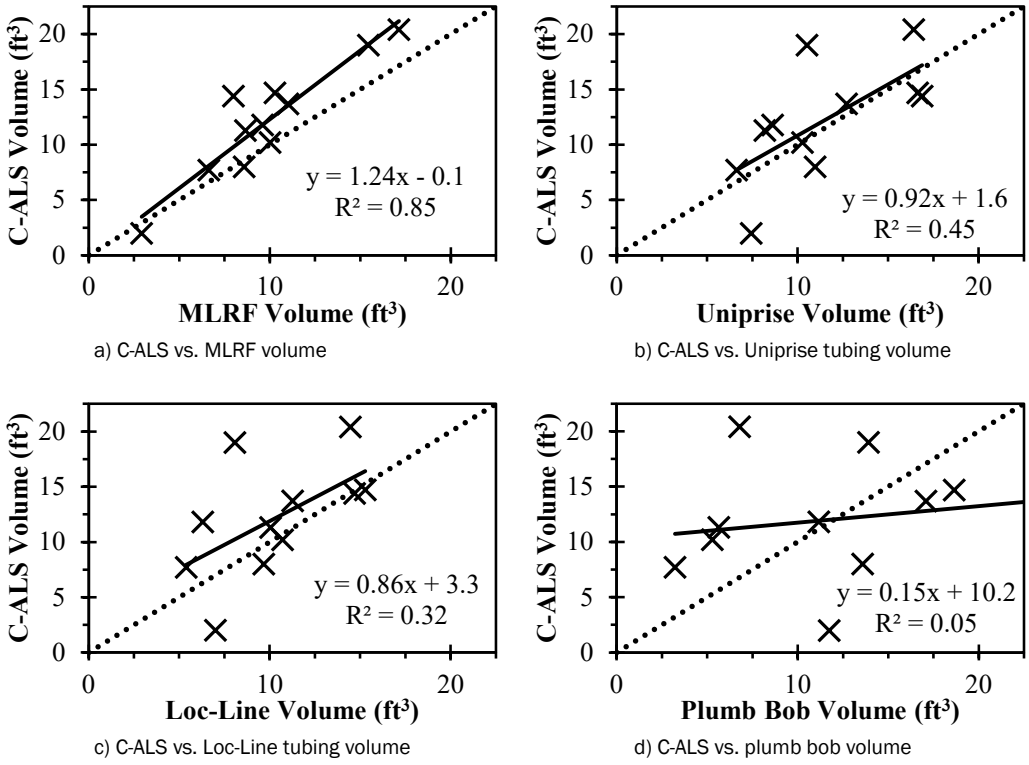

a) C-ALS vs. MLRF volume

b) C-ALS vs. Uniprise tubing volume

c) C-ALS vs. Loc-Line tubing volume

d) C-ALS vs. plumb bob volume

Similarly, Uniprise and Loc-Line tubing volumes were calculated assuming camouflets were ellipsoids. For either method, the four approximately horizontal measurements were averaged and used as the ellipsoid radius, A. Plumb bob depth was used for ellipsoid depth as discussed previously. The average Uniprise and Loc-Line tubing volumes were 11.4 and 10.3 ft^3, respectively, which was 0.7 and 1.8 ft^3 less than the average C-ALS volume. Thus, on average and considering the crudeness of these two techniques, the error in volume relative to the C-ALS was surprisingly low.

For the plumb bob, volumes could not be directly calculated without making additional assumptions (i.e., the radius was some multiple of the depth). In Model 2, the radius was about 25% greater than the depth on average. If this same adjustment factor of 1.25 was used for the Silver Flag camouflets, the average volume for all camouflets would be 16.1 ft^3, which is considerably larger than the C-ALS average volume. However, using Silver Flag MLRF data, the average adjustment factor was 1.1 instead of 1.25. Using 1.1 as shown in Table 5.5 yielded an average plumb bob volume of 12.5 ft^3, which is essentially equivalent to the C-ALS average volume. On average, the plumb bob volume most closely approximated the C-ALS volume, although this did require the use of the MLRF to determine the radius-to-depth adjustment factor.

On average, results are contrary to expectations. It would be expected that the MLRF would best approximate volume trending towards the plumb bob as the worst approximation, which was not the case. However, it is important to consider more than just the average comparisons. The right side of Table 5.5 shows the C-ALS volume minus the volume for a given technique and camouflet. As before, the MLRF exhibits the highest average difference relative to the C-ALS. However, it exhibits the lowest standard deviation (St. Dev.) and coefficient of variation (COV), implying it is the least variable of the techniques.

Figure 5.25 plots C-ALS volumes against volumes from each discrete technique and illustrates the concept discussed in the previous paragraph well. The MLRF, which had the lowest COV relative to the C-ALS in Table 5.5, also has the highest R^2 and demonstrates the best relationship to the C-ALS, even though its volume is, on average, less than that of the C-ALS. In contrast, with the plumb bob, the average volume is essentially equivalent to the C-ALS, but there is almost no relationship, meaning that for any one camouflet, the plumb bob may yield significant error.

Going back to the MLRF, it is not necessarily surprising that the MLRF yields a smaller volume than the C-ALS because the measurement resolution is significantly less. At a 3° scan resolution, the C-ALS produces thousands of measurement points; whereas, four measurements from the MLRF were used. Thus, the MLRF is more likely to misrepresent any notable features within the camouflet (recall this principle is similar to that discussed for Figures 5.4 and 5.9 in the laboratory models). However, because of the fairly reasonable relationship (i.e., R^2 of 0.85) and the y-

intercept of nearly zero, it can be generalized that the C-ALS volume is, on average, 1.25 times the MLRF volume.

5.2.4 Destructive void characterization

Destructive void characterization was conducted primarily to validate void measurement techniques, specifically the C-ALS since it was used as the reference for other measurements. Figure 5.26 shows the OPE for Camouflet 12 at the surface of the base material after the PCC slab was removed as well as the camouflet void once base material was removed.

Figure 5.26. Camouflet 12 destructive void characterization.

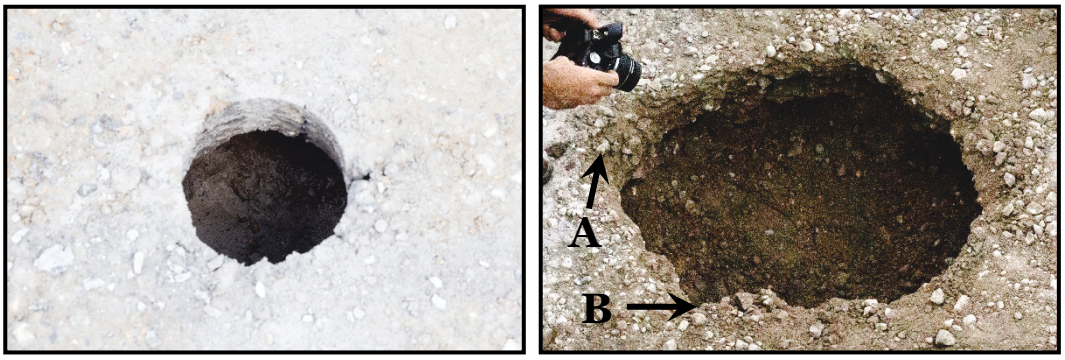

a) Camouflet 12 OPE at interface of PCC and base

b) Camouflet 12 after removing base material

Figure 5.26b also shows a photograph being taken of the Camouflet 12 void. Approximately 100 photographs were taken from various angles and positions around the circumference of the camouflet to perform a photogrammetry analysis in PhotoScan. Figure 5.27 shows the resulting point cloud model, which, as a side note, illustrates the quality gap between typical photogrammetry and that attempted with the MC1 borescope and the SVS camera. For ease of comparison, points A and B were marked in both Figure 5.26b and Figure 5.27.

Figure 5.27. Photogrammetry point cloud of DVC Camouflet 12.

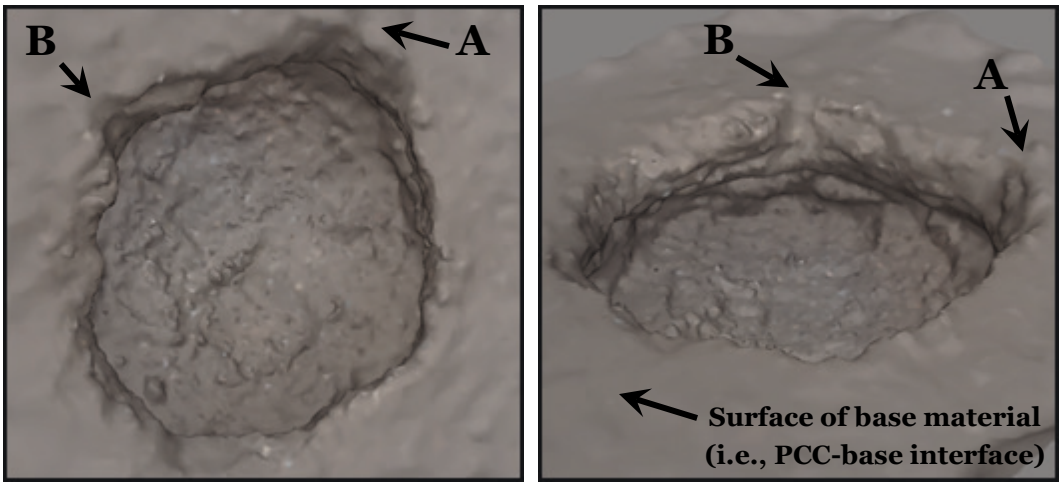

The PhotoScan point cloud was exported to AutoCAD for further analysis. First, points representing the PCC-base material interface were trimmed to leave only the camouflet (Figure 5.28a). As a result of removing the base material covering the camouflet (Figure 5.26b), the ceiling of the camouflet was damaged and had to be estimated. To do this, it was assumed that the dashed line in Figure 5.28a represented the depth to which base material was disturbed by excavation. Points above this dashed line were removed, and an approximate ceiling was put in its place.

Figure 5.28. AutoCAD model developed from Camouflet 12 point cloud.

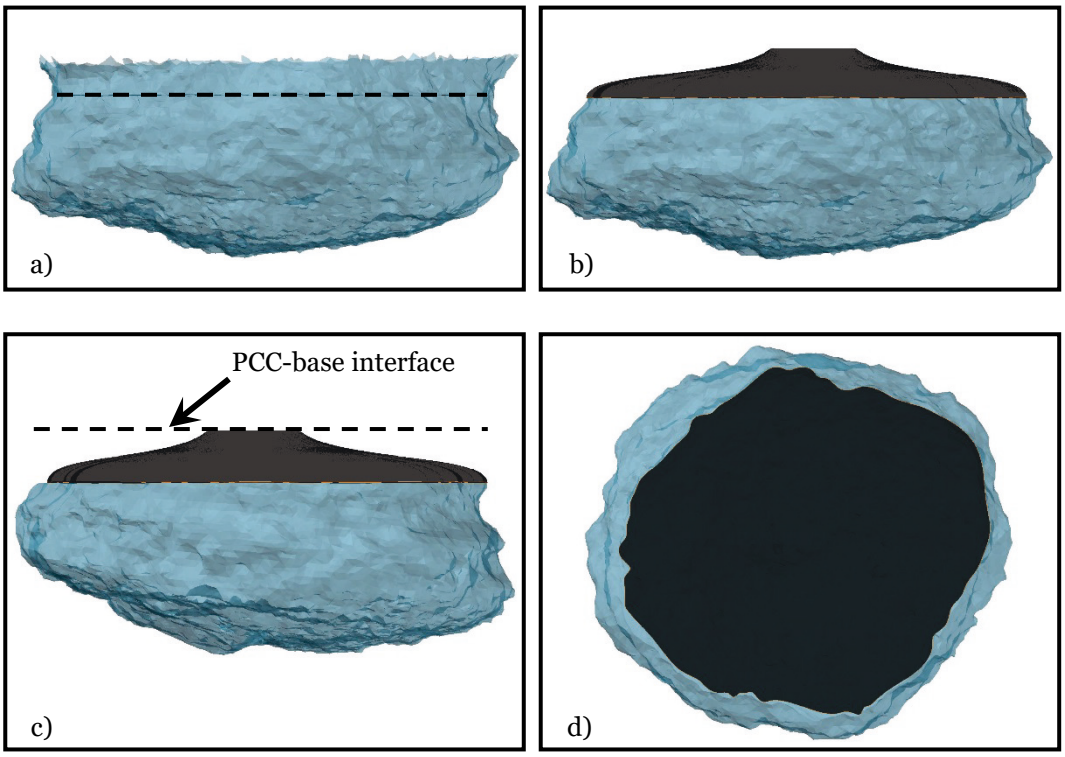

The approximate ceiling was produced as a lofted surface that attempted to match the slopes of the camouflet walls where they met (Figure 5.28b and Figure 5.28c). Its overall height was set based on measured camouflet dimensions. Lastly, it was tapered near the OPE to represent the thickness of base material present between the camouflet void and the PCC-base interface at the OPE as shown in Figure 5.26a.

In order to use this model to determine volume, it needed to be scaled to the correct size since point clouds are not inherently scaled. Physical measurements of the open camouflet's diameter were taken at multiple points and used to resize the model appropriately. This was a reasonable, but still somewhat approximate, process. After scaling, the volume of the Camouflet 12 photogrammetry model was 3.6 ft^3.

In contrast, the Camouflet 12 C-ALS volume was only 2.0 ft^3. At first glance, it appears the C-ALS is less accurate than specified; however, that issue may mostly be for Camouflet 12 alone. Figure 5.29 shows the Camouflet 12 C-ALS scan where points exist that essentially follow the entire circular path of the C-ALS head as indicated by the dotted line. Why this happened is not known; however, it likely has to do with the fact that the camouflet was too small relative to the 1.6 ft minimum range of the C-ALS (Table 3.5). The depth was 1.7 ft, and the diameter was 2.7 ft. If the C-ALS was positioned exactly in the center of the camouflet, the maximum distance to a camouflet wall would be 1.35 ft, which is less than its specified minimum range.

Figure 5.29. C-ALS scan of Camouflet 12.

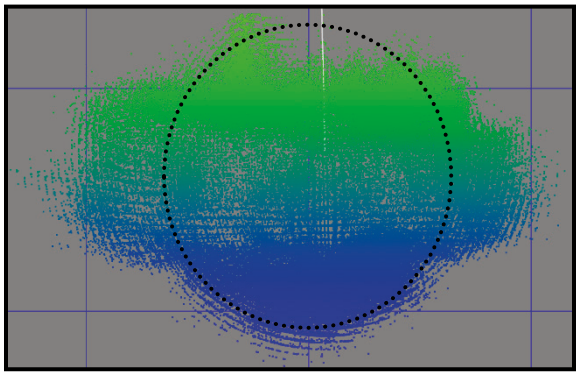

It should be noted that other camouflets generally exhibited radii greater than, but not much greater than, 1.6 ft. While this resulted in some scatter as discussed at the end of Section 5.2.1 and did likely lend to some volume errors, this did not seem to have as great of an impact on all other

camouflets as it did for Camouflet 12 (i.e., other camouflet scans did not exhibit the circular pattern that Camouflet 12 did).

Because Camouflet 12 was so small, it was not the ideal camouflet for destructive void characterization and likely did not accurately represent the C-ALS's capabilities. Unfortunately, this also prevented firm statements from being made as to the C-ALS's accuracy for other camouflets. However, it is of interest to note that 1.25 times the MLRF volume for Camouflet 12 (i.e., 1.25 times 2.9) yields 3.6 ft^3, which is equivalent to the volume determined from the photogrammetry model. In an indirect way, this perhaps gives some credibility to the C-ALS as far as it pertains to the other larger camouflets.

5.3 Development of practical void characterization method

In terms of a practical method for quickly assessing the general size of a camouflet and volume of repair material required, the C-ALS is most likely too expensive, time consuming, and delicate for normal repair operations. The C-ALS could be useful in more critical cases, but for most cases, the value added by the C-ALS relative to a simpler tool like the MLRF is likely not worth the additional cost, training, and care. Additionally, the MC1 borescope and the SVS camera were of no benefit, especially when considering their approximately $10,000 cost. Conversely, while the Uniprise tubing, Loc-Line tubing, and plumb bob were very cost effective, they were too simplistic to consistently provide reliable results.

In order to obtain a reasonable volume estimate, the field characterization results indicated radius measurements were necessary. These could be obtained with the Uniprise or Loc-Line tubing; however, the process was relatively cumbersome. If the radius-to-depth ratio was somewhat of a constant, the plumb bob depth could be used to estimate radius, but this was not the case. Ultimately, the most reliable and easiest to obtain radius measurements were those obtained with the MLRF.

Although only four radius measurements were taken per camouflet in the field, the MLRF, with both its onboard memory and ability to transfer data via Bluetooth, can easily collect many more measurements per camouflet with little additional effort, especially if only horizontal measurements (i.e., 0° measurements) are being collected. While the MLRF was used in this project to collect depth, 45°-angled measurements, quarter-depth measurements, etc., the simple horizontal measurements at the greatest diameter (approximately mid-depth) proved to be sufficiently useful.

Depth can be measured with a plumb bob, or more preferably a tape measure or folding rule, in less time than the MLRF can be repositioned to measure depth.

The best tradeoff between cost, complexity, and accuracy seems to entail measuring the radius with MLRF mid-depth measurements and the depth with the plumb bob (or tape measure or equivalent). Volume can then be calculated using Equation 5.2, and the result can be corrected for camouflet shape variations that the ellipsoid assumption may overlook by multiplying by the 1.25 adjustment factor. In this way, the entire method for determining camouflet volume would be as follows:

1. Determine camouflet depth.
    a. Measure the total depth from the pavement surface to the bottom of the camouflet with a plumb bob, tape measure, folding rule, or equivalent.
    b. Measure the thickness of the concrete and any observable base material present between the concrete and the camouflet.
    c. Subtract the pavement thickness from the total depth to obtain the camouflet depth, H.
2. Determine the average camouflet radius.
    a. Lower the MLRF into the camouflet and monitor the real-time distance on the display. Find the depth at maximum radius by adjusting the height of the MLRF until the distance on the display is at its maximum. Lock the MLRF collar to maintain this depth.
    b. Rotate the MLRF taking a minimum of 4 measurements at 90° intervals. More densely spaced measurements can be taken and are preferred. Since measurements are saved in the MLRF memory or sent to a Bluetooth-enabled device, little additional effort is required to process a greater number of measurements.
    c. Average the recorded radius measurements to obtain the average camouflet radius, A.
3. Calculate the ellipsoidal volume using Equation 5.2.
4. Calculate the corrected volume by multiplying ellipsoidal volume by an adjustment factor of 1.25.

This method appears to be a reasonable starting point. Additional experience with the method and with camouflets in general would be beneficial in terms of refining the method and the 1.25 adjustment factor. A larger or additional adjustment factor may be desirable solely for the purpose of conservatively estimating repair material quantities.

6 Camouflet Repair and Trafficking Results

6.1 Repair process results

The following two sections provide discussion on the camouflet repairs conducted including notable considerations, lessons learned, etc.

6.1.1 Cementitious repairs

Table 6.1 provides information from the cementitious repairs on Camouflet Series A, B, and C. As stated in Section 3.5.4, gate settings on the SVM were set at either 5.6 or 6.5 depending on the material as shown in Table 6.1. The decision to increase the gate setting to 6.5 for FF-CTS was based on the initial material consistency observed when priming the SVM. The initial FF-CTS consistency appeared much more fluid than typical flowable fills when placed; increasing the gate setting (i.e., reducing the *w/s* ratio) yielded a more typical flowable fill consistency similar to that of the FF-BU placed in Camouflet Series A. It is interesting to note that this behavior contradicts the laboratory results in Section 4.1 where FF-CTS required a greater *w/s* ratio to yield representative flowability. The reason for this is not known and should be investigated further if future efforts desire to fully evaluate FF-CTS as an approved product.

Table 6.1. Cementitious camouflet repair data.

Camouflet Series	Repair Material	SVM Gate Setting	Camouflet ID	Placement Method	Target Cure Time (h:mm)	Actual Cure Time (h:mm) until:	
						HWD Testing	C-17 Trafficking
A	FF-BU	5.6	1	Tremie Funnel	0:30	0:33	0:42
			2	Mini Hopper	1:00	1:04	1:12
			3	Mini Hopper	2:00	2:05	2:12
B	FF-CTS	6.5	4	Tremie Funnel	0:30	0:30	0:40
			5	Tremie Funnel	1:00	1:01	1:10
			6	Mini Hopper	2:00	2:02	2:10
C	RSCM	5.6	7	Tremie Funnel	0:30	0:30	0:45
			8	Tremie Funnel	2:00	2:01	2:15

Placement times for each camouflet were quite fast at 2 to 3 min each. With the exception of priming the SVM for the first camouflet in a series (which only required a couple minutes but did require one man to operate the CTL), set up time prior to production was almost negligible. One operator was required to pull or back the SVM to the camouflet while another gave instructions. SVM placement did not have to be exact since the swinging discharge boom provided side-to-side tolerance and both the

tremie funnel and mini hopper provided front-to-back tolerance. Note that priming of the SVM could also be conducted to the side in a designated washout area.

The greatest difficulty during repairs was tracking the fill level of material inside the camouflet and knowing when to stop production of the SVM. If the SVM operator waited to stop the SVM until the camouflet was visibly full (i.e., material at the surface), the camouflet would be overfilled as the remaining material in the SVM auger was discharged, creating a spill as shown in Figure 6.1a. This material was cleaned up to prevent creating a foreign object debris (FOD) issue (feathering of material has been noted as a FOD concern in multiple previous reports (Priddy et al. 2011a; 2011b).

Figure 6.1. Photographs of camouflet pours using the mini hopper.

a) Overfilling camouflet with the mini hopper

b) Cleaning excess material from surface

c) Final cleaned surface

d) Example of good mini hopper pour

Figure 6.1b shows the excess material being shoveled and swept into a CTL bucket shortly after it was placed and once it was set enough to shovel. Aside from requiring a few minutes post-pour, this clean-up was not a major burden. It was also fairly effective, leaving sand-sized or smaller particles. It was not the most ideal solution aesthetically (Figure 6.1c), but it did not seem to pose a FOD threat.

Figure 6.1d shows the end of the Camouflet 6 pour (third and final use of the mini hopper). In this case, an adequate amount of material was produced, and a spill was avoided. The key difference between the Camouflet 6 pour and the earlier pours was that one man was dedicated to monitoring the fill level. This required him to insert his arm into the camouflet OPE alongside the mini hopper trunk as material was also being poured. For a long-term solution, this is not practical; during the field work, however, it was the most obtainable solution given the options at hand.

Figure 6.2 illustrates the same overfilling issue but with the tremie funnel. Spills with the tremie funnel were generally cleaner, however, because the material was able to flow freely out of the bottom of the funnel rather than creating back pressure and spewing out as in Figure 6.1a. Therefore, tremie funnel spills produced clean circular spills that were generally easier to clean. Additionally, some spillage was beneficial because the spilled material could be used to fill in the camouflet as the fill level dropped under vibration (Figure 6.2a and Figure 6.2b). Tremie funnel spills usually cleaned up better than mini hopper spills.

Figure 6.2. Photographs of camouflet pours using the tremie funnel.

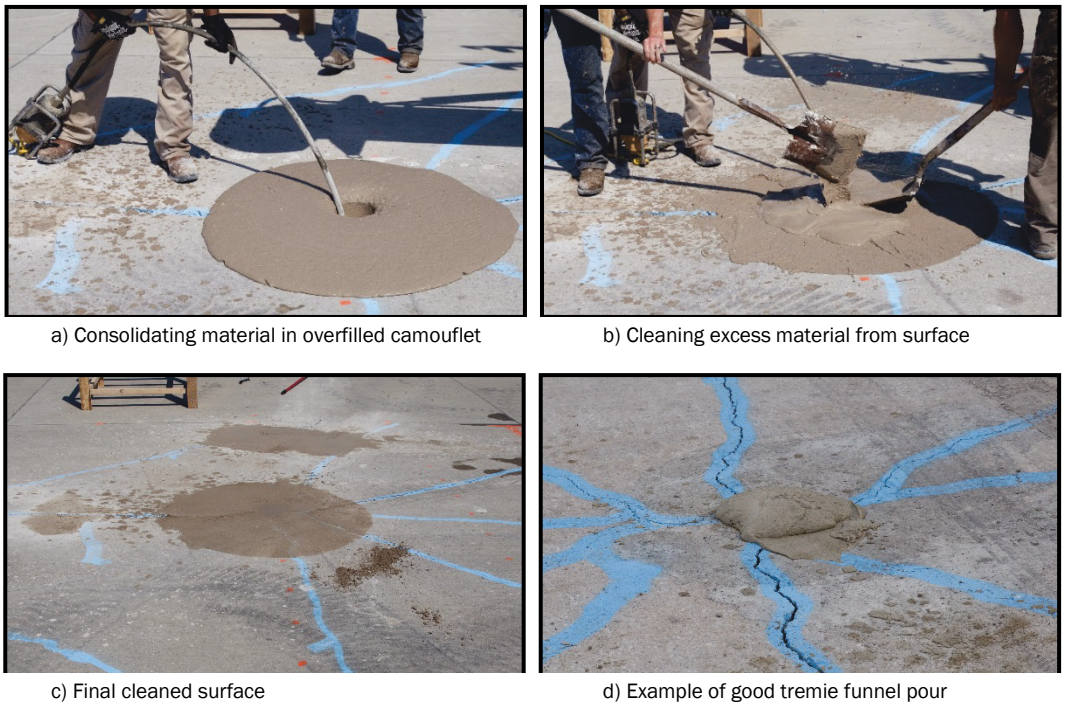

a) Consolidating material in overfilled camouflet

b) Cleaning excess material from surface

c) Final cleaned surface

d) Example of good tremie funnel pour

With practice and with the manual method of monitoring fill level inside the camouflet, the team improved tremie funnel pours as well so that an appropriate, but not excessive, amount of spillage was produced (Figure 6.2d). This provided enough material to fill in the camouflet as material was consolidated but required minimal clean-up at the end. While the manual fill level monitoring undoubtedly improved operations, two operators timing the filling of a camouflet and the shutoff of the SVM was still an art that had to be refined with practice.

Between the mini hopper and the tremie funnel, the tremie funnel was the preferred material transfer solution. Though bulkier, it was sturdier, more durable, and more efficient in terms of allowing material to flow. It was also easy to clean and yielded neater spills when they occurred.

In terms of placement, the greatest remaining need for smooth camouflet repair operations remains with tracking the fill level and producing a proper amount of material. After the fact, several potential solutions were discussed, including proactive monitoring ideas such as a floating level indicator and reactive ideas such as adding a valve to the tremie funnel outlet that could be closed quickly as soon as material began to overfill the camouflet.

Given the testing potentially required to develop a floating level indicator that works properly, using a valve on the tremie funnel would be the most promising solution absent further testing and evaluation. A 4-in.-diameter pull-handle gate value, such as the one shown in Figure 6.3, could be installed at the outlet of the tremie funnel, providing a quick flow shutoff solution.

Figure 6.3. Pull-handle gate valve.

The tremie funnel is also large enough that it could serve as a temporary holding reservoir, providing enough buffer to contain the remaining discharge from the SVM once the gate valve is closed and the SVM is stopped. This could also provide a surplus of material in case more is needed after material settles in the camouflet under vibration. A more robust (i.e., steel) tremie funnel stand should be fabricated if the tremie funnel was to be fielded. Some type of lifting mechanism should also be considered for a new stand for moving the tremie funnel to the washout area or to a subsequent camouflet. This could be in the form of handles for lifting by hand or supports or pockets for lifting with a forklift or both.

Table 6.1 also provides the actual cure times each camouflet experienced prior to being subjected to HWD testing or C-17 load cart trafficking. HWD testing generally occurred within 5 min of the intended cure time. There was typically some lag (about 7 to 14 min) between completion of HWD testing and the beginning of trafficking. This delay with respect to the target cure times was largely unavoidable.

6.1.2 Foam repairs

Table 6.2 provides information from the FI-10S repairs on Camouflet Series D. In the field, volume data from the C-ALS, although collected, had not yet been provided by Renishaw to ERDC. Therefore, MLRF radius measurements were averaged and used alongside depth to estimate the required volume of liquid FI-10S. Note that the specific calculation method described in Section 5.3 was not followed as it had not yet been developed; data analysis used to finalize the Section 5.3 method was performed after field testing. The field volume estimates for Camouflets 10 and 11 were 20.5 and 10.5 ft^3, respectively, which differed quite significantly from C-ALS volumes in Table 5.3. These volumes corresponded to 26.5 and 13.5 gal of mixed liquid foam.

Ultimately, Camouflets 10 and 11 required only 4.5 and 10.5 gal of mixed liquid foam (approximately) to be fully filled. Note that recalculating estimated foam quantities using Table 5.3 C-ALS volumes would require 14.6 and 9.9 gal, respectively. This estimate would have been within reason for the actual quantity needed for Camouflet 11 but still excessive for Camouflet 10, which had to do with moisture exposure in Camouflet 11 as discussed subsequently.

Table 6.2. Foam camouflet repair data for FI-10S.

Camouflet Series	Camouflet ID	No. Batches of Foam	Liquid Foam Quantities (gal)		Target Cure Time (h:mm)	Actual Cure Time (h:mm) until:	
			Estimated	Actual		HWD Testing	C-17 Trafficking
D	10	1	26.5	~4.5	0:30	0:35	0:45
	11	3	13.5	~10.5	2:00	2:06	2:15

– *Average scan times rounded to nearest 30 second increment.*

Placement times for foam repairs were longer than for cementitious repairs, partially because time was given in between each foam batch for the batch to fully react and expand. Without more exact volume estimates, the expansive characteristics of the foam actually slow the repair process since time for expansion must be accommodated between each batch to avoid excessive overfilling or possible, in a severe case, slab upheaval. Overall, repairs took about 20 to 30 min.

Although there was no guaranteed way of knowing, the combination of the pump and dry cement used to remove water seemed to be largely effective for Camouflet 11. Figure 6.4a shows the excess foam overfilling the camouflet; it appeared similar to the normal consistency of FI-10S as it expands. One crack or split was created; this is somewhat typical and likely due to the exothermic reaction and possibly, to some extent, residual moisture in the camouflet.

Figure 6.4. Photographs of polyurethane foam repairs.

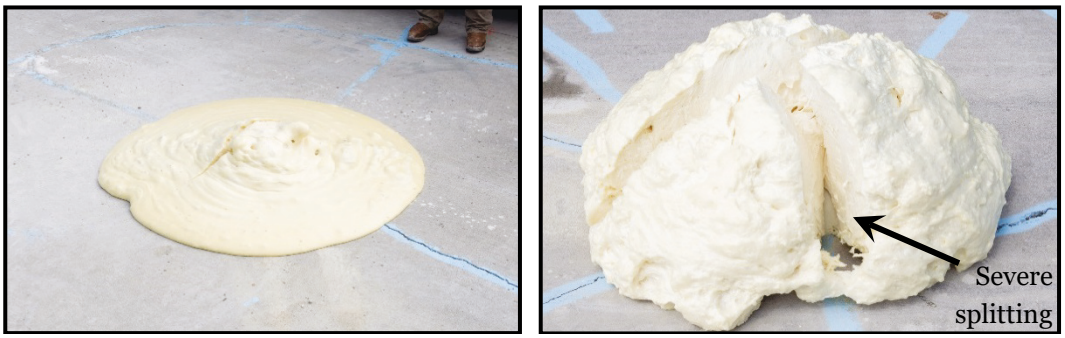

a) Camouflet 11 – no major moisture effects observed b) Camouflet 10 – major moisture effects observed

In contrast, Figure 6.4b shows the excess foam for Camouflet 10 which expanded and split to a much greater degree as is typical of FI-10S when exposed to even fairly small amounts of moisture. The increased expansion is also evidenced in the fact that only 1 batch of approximately 4.5 gal was required despite the larger volume of Camouflet 10. This foam was extremely soft and compressible when fully reacted. The same level of care was given to each camouflet when trying to remove water, but the pumping then drying method was not effective for Camouflet 10.

Unfortunately, there was no way to determine the source of the moisture (e.g., standing water on camouflet floor, sidewall moisture, condensation on camouflet roof, etc.) that caused the foam to behave erratically.

As with Camouflet Series A, B, and C, actual cure times differed slightly from the target cure times. Similarly, HWD testing differed by about 5 min, and initiation of load cart trafficking differed by 15 min.

6.2 Material strength results

Figure 6.5 provides compressive strength results from the field concrete cylinders produced during Camouflet Series A, B, and C. As with the laboratory results, FF-CTS strengths were on the order of twice the FF-BU strengths at corresponding cure times. As expected, RSCM strengths were in excess of 5,000 psi at 28 days and were significantly higher at all cure times than flowable fill materials (about twice that of FF-CTS). For discussion, FF-BU, FF-CTS, and RSCM 2-hr compressive strengths were, in roundabout numbers, 1,000, 2,000, and 4,000 psi, respectively. In contrast, FI-10S UCS (at 2% ε) measured at ERDC on field cylinders averaged 200 psi.

Figure 6.5. Field cementitious material compressive strengths.

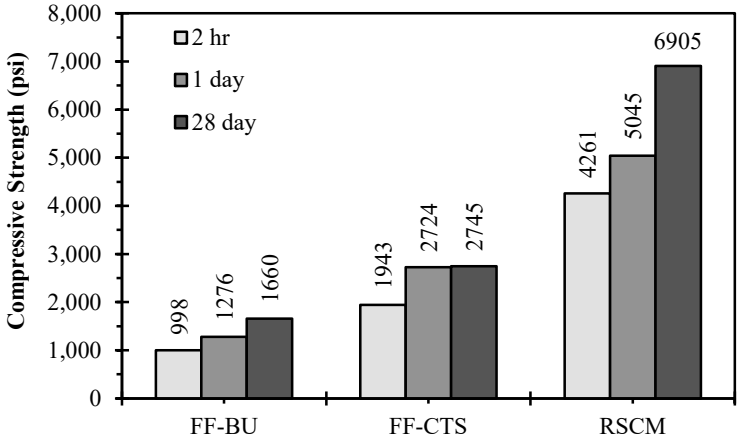

6.3 Visual assessments

Throughout field testing, cracks were marked on each slab as shown in Figure 6.6 and mapped. In contrast to most ADR repairs (which pour a new concrete cap as part of the repair), the camouflet slabs exhibited a great deal of cracking even before trafficking as a result of the camouflet blasts. Existing cracks (i.e., post-blast, pre-repair) were marked in blue, and cracks due to trafficking were marked in yellow. Photographs of all other camouflet slabs before and after trafficking are provided in Appendix A.

Figure 6.6. Example crack map photograph showing Camouflet 1.

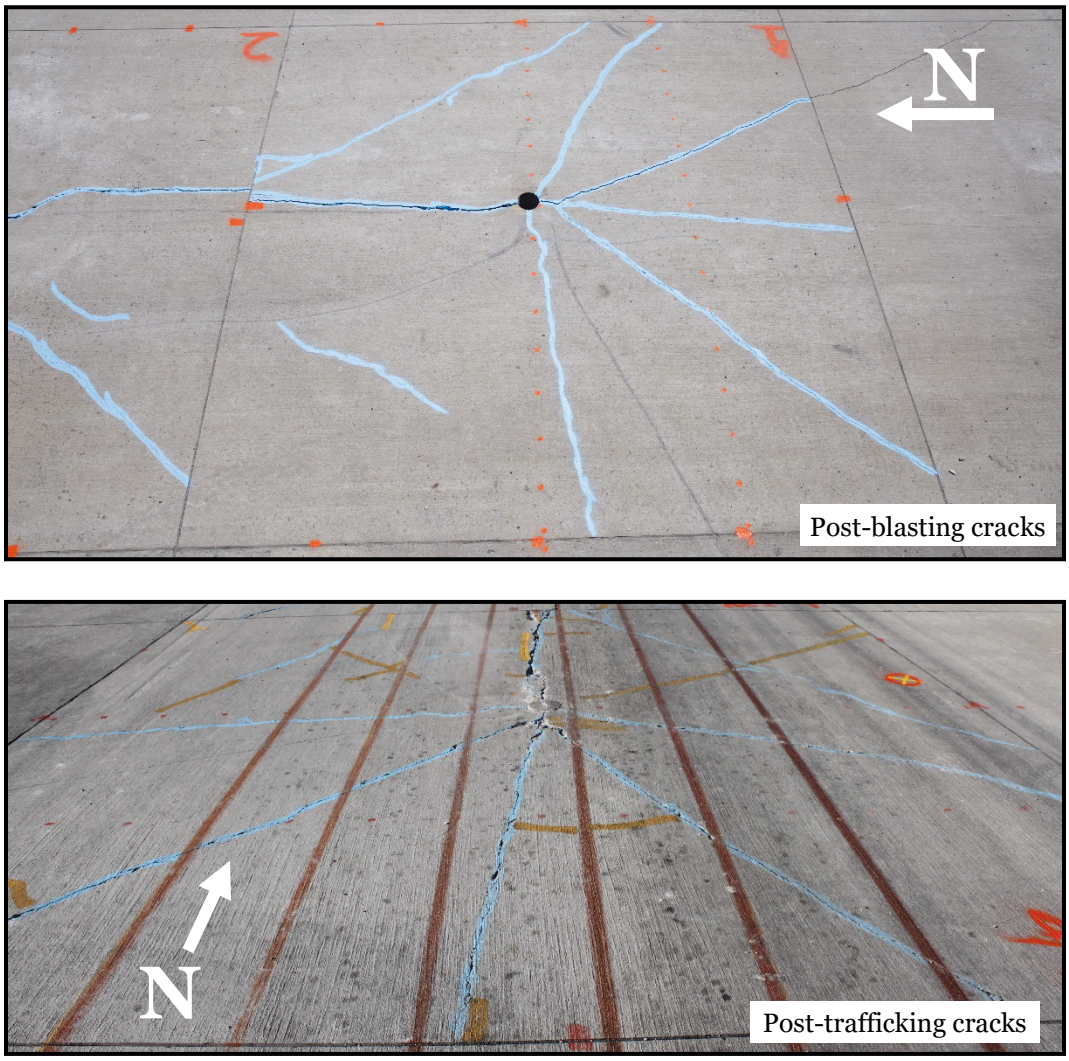

Sketches of each slab were made and used to produce the crack maps shown in Figure 6.7 and Figure 6.8. Crack severity was rated according to the Pavement Condition Index (PCI) system (i.e., low = <1/8 in. and low FOD potential, medium = 1/8 to 1 in. and/or some FOD potential, and high = >1 in. and/or definite FOD potential). In Figure 6.7 and Figure 6.8, crack severity is illustrated with light, medium, and heavy line weights; colors represent trafficking pass levels from blue at 0 passes (post-blast) to red at 1,192 or 1,568 passes. Note that Camouflet 3's slab was 12 by 15 ft.

Figure 6.7. Crack maps for Camouflet Series A and B by pass level and crack severity.

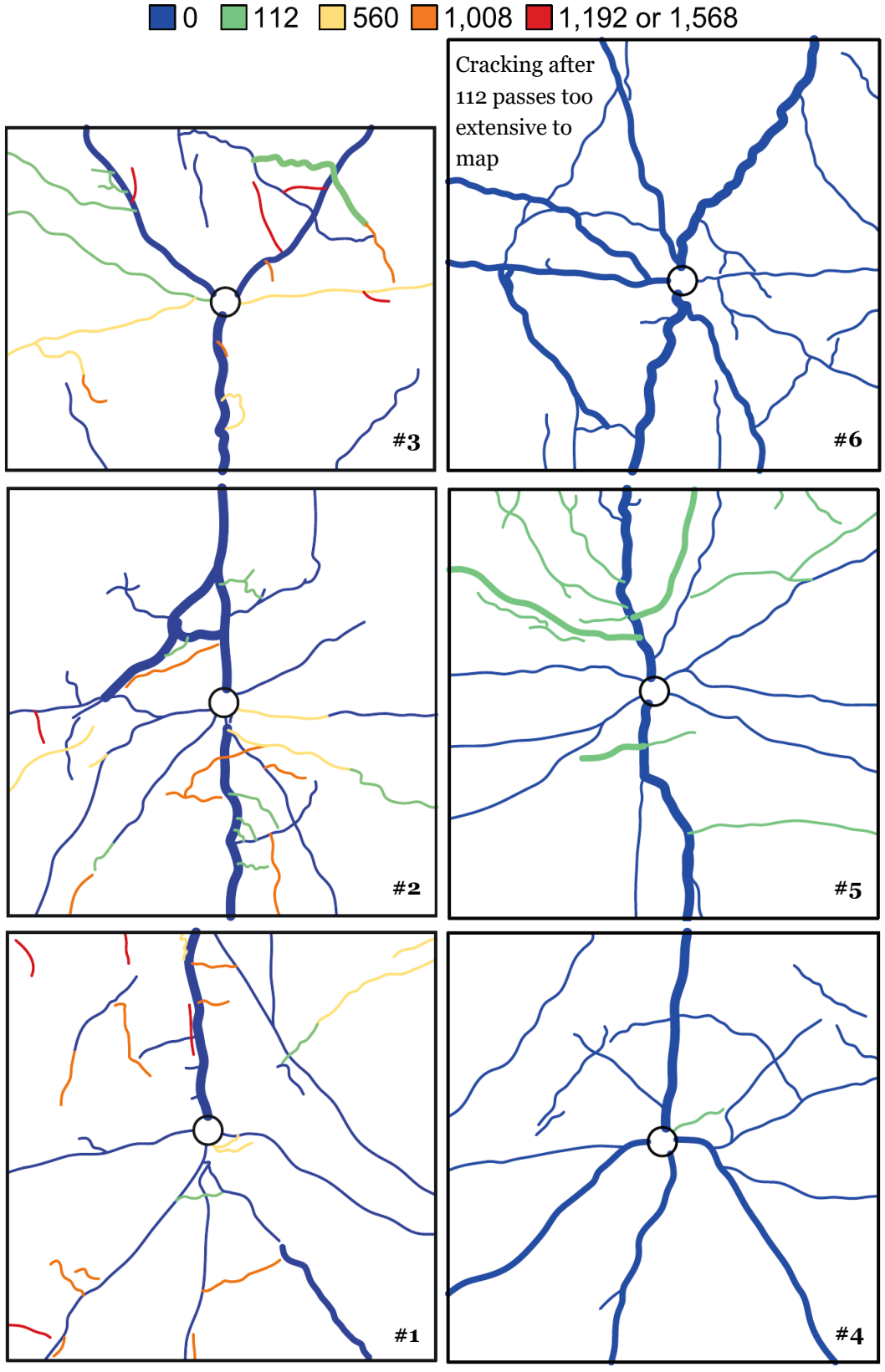

a) Camouflet Series A – 1,192 total passes

b) Camouflet Series B – 112 total passes

Figure 6.8. Crack maps for Camouflet Series C and D by pass level and crack severity.

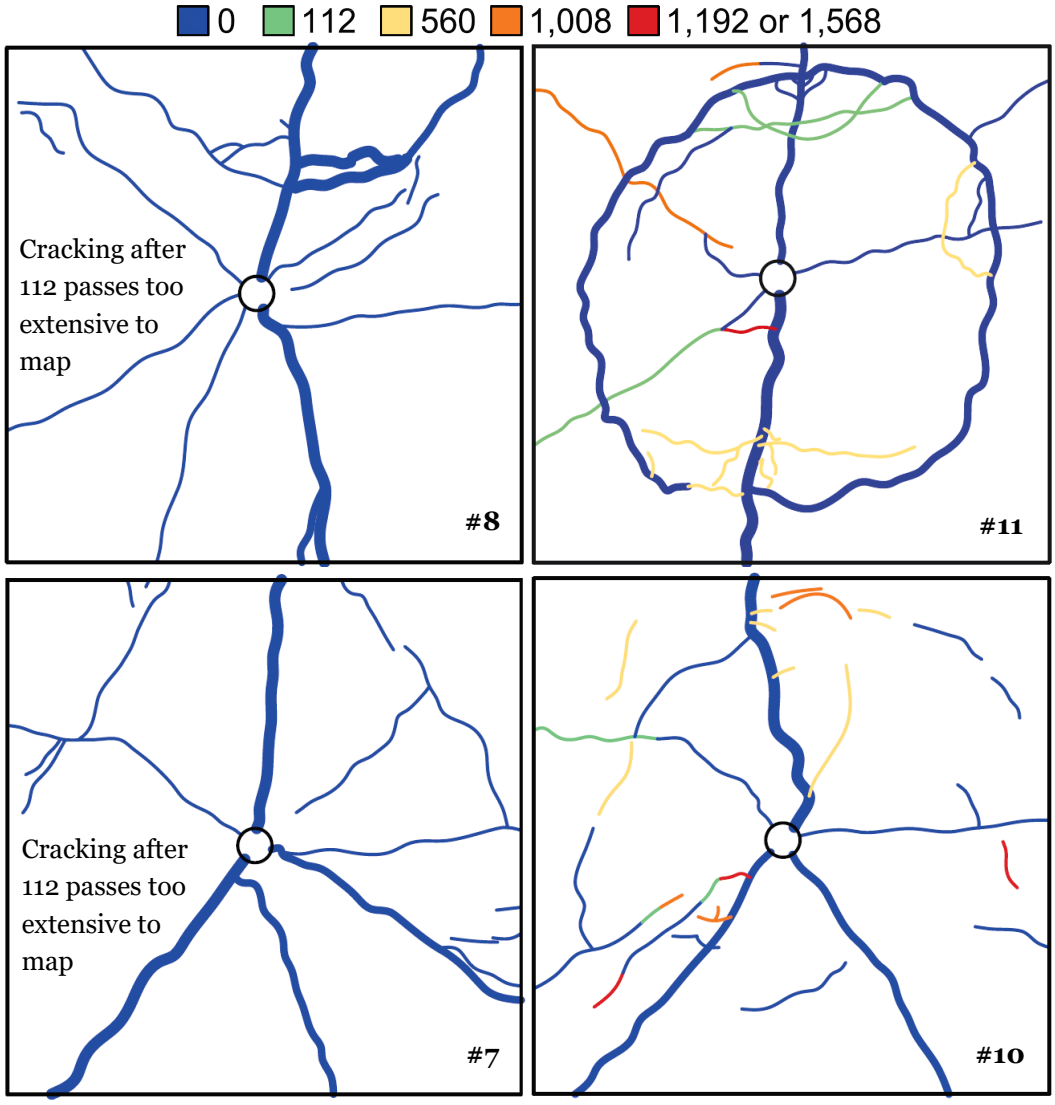

a) Camouflet Series C – 1,568 total passes b) Camouflet Series D – 112 total passes

Figure 6.7 and Figure 6.8 are also arranged by camouflet series meaning the figures are laid out similarly to the Silver Flag slabs in that they are adjacent to other slabs in the same series. Doing so illustrates the combined effects of blasting three camouflets in adjacent slabs in that a high-severity crack can be observed down the centerline of each camouflet series. These high-severity centerline cracks were also associated with slab upheaval that is discussed in more detail in Section 6.4.

Every slab tested in this project would be considered a shattered slab by PCI definitions just as a result of the blasting alone. By typical trafficking criteria, all slabs were considered failed before a single C-17 pass was ever

applied. The camouflets were repaired and trafficked despite being shattered, and trafficking continued, not until failure (since they were already failed), but until they were deemed no longer trafficable as a safety hazard to the load cart (or until the field testing schedule no longer accommodated it). In all, Camouflet Series A was subjected to 1,192 passes, Camouflet Series B and C were subjected to 112 passes, and Camouflet Series D was subjected to 1,568 passes.

For Camouflet Series A and D, nearly all crack development that occurred as a result of load cart trafficking was classified as low severity. This was an interesting finding considering the extensive cracking that existed before the camouflets were subjected to any traffic. While new cracks did develop and existing cracks grew in length, cracks did not noticeably increase in severity. Trafficking was continued through the end of the Silver Flag work (1,192 and 1,568 passes) at which point all slabs were still fully trafficable despite being shattered from the beginning. Series A and D were considered successful camouflet repairs for emergency situations.

Camouflet Series B and C did not perform as well under load cart trafficking. While Camouflet 4 exhibited almost no change after 112 passes, Camouflet 5 developed several medium-severity cracks, and all other camouflet slabs developed such severe cracking that it could not be reasonably represented in a map sketch.

Figure 6.9 shows several overall and close-up photographs of Camouflet 6. Part way to 112 passes, slab 6 broke into multiple small pieces that visibly and independently moved as the load cart passed over them. This kneading action began pumping water to the surface. As part of the trafficking pattern, the load cart also drove over the slab adjacent to Camouflet 6 on the north side, which broke into numerous small pieces as well. One factor that may have contributed to this was the unpaved area bordering the slab; base course moisture levels could have been considerably different than other areas, resulting in a weaker pavement structure.

Figure 6.9. Severe load cart damage on Camouflet 6.

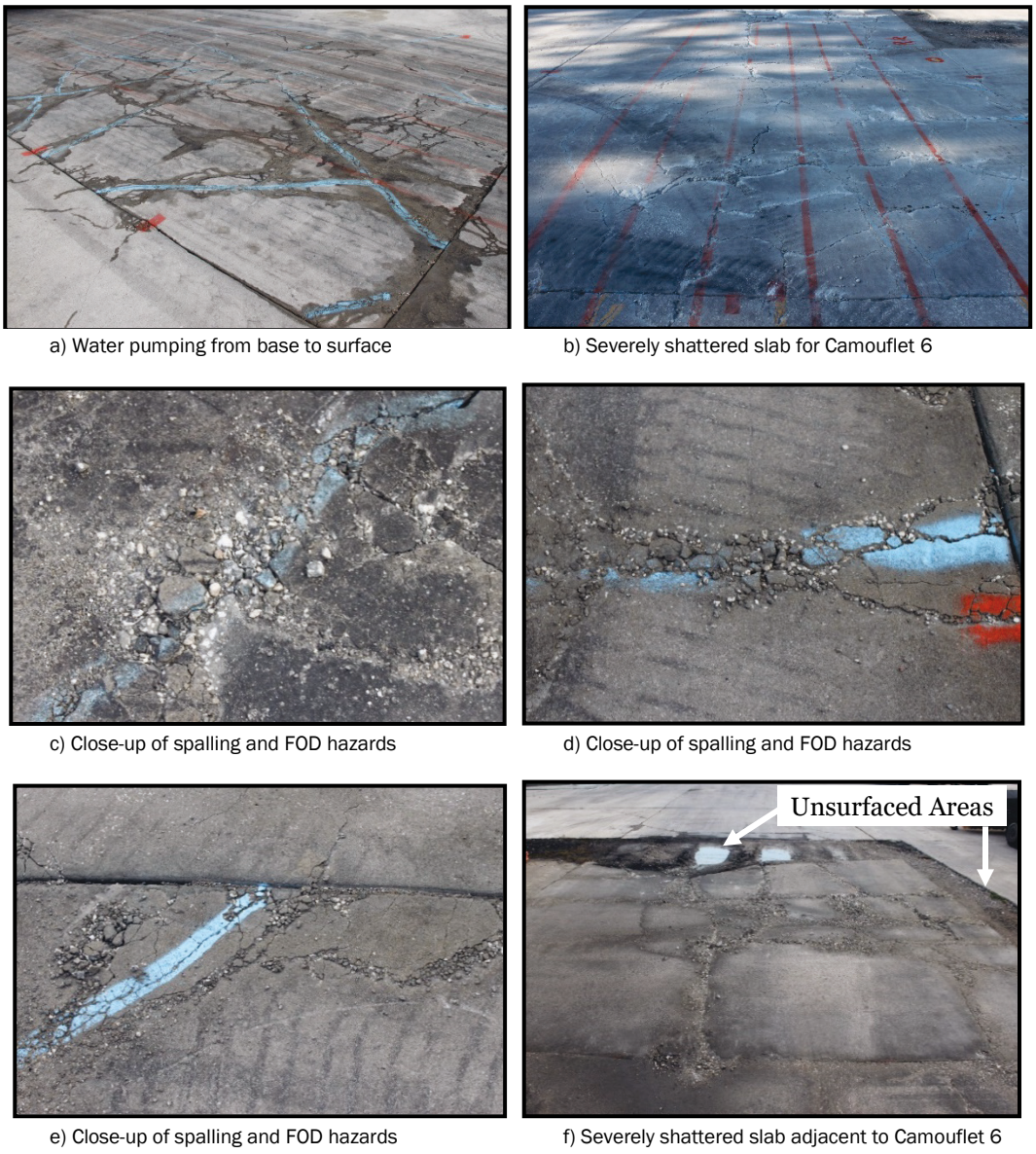

a) Water pumping from base to surface

b) Severely shattered slab for Camouflet 6

c) Close-up of spalling and FOD hazards

d) Close-up of spalling and FOD hazards

e) Close-up of spalling and FOD hazards

f) Severely shattered slab adjacent to Camouflet 6

Similarly, Figure 6.10 shows extensive damage to Camouflets 7 and 8 after only 112 passes. In this case, the blue paint used to mark pre-existing cracks was not dry when rain moved into the Silver Flag area, and the paint was washed away. All new cracks that occurred due to trafficking were marked in yellow paint to illustrate the extent of cracking. Despite being as severely cracked as Camouflet 6, Camouflets 7 and 8 did not exhibit noticeable movement under the load cart like Camouflet 6. This supported the idea that a saturated base may have had some influence on Camouflet 6.

Figure 6.10. Severe load cart damage on Camouflets 7 and 8.

Overall, crack development and growth was not related to the repair material, and cure time did not have a noticeable impact on cracking either. The two camouflet series with the lowest-strength repair materials (Series A and D with compressive strengths of 1,000 and 200 psi, respectively) endured a significantly greater number of passes than Series B and C which had repair material compressive strengths of 2,000 and 4,000 psi at 2 hr, respectively. For Camouflet Series B (FF-CTS), Camouflet 6 exhibited the most cracking despite being cured for 2 hr compared to 1 hr and 30 min. Its proximity to the unsurfaced area where moisture could be introduced may have had an effect on this. However, for all other camouflet series, there were no distinguishable cracking differences with respect to cure time.

Recall Table 3.7 that provides concrete thickness and strength for the slabs that were tested in the camouflet project. Slabs in Camouflet Series B and C were individually placed as part of training exercises, were 2 to 6 in. thinner than other slabs, and exhibited approximately half the compressive strength of Series A and D slabs. These factors seemed to control cracking behaviors more than repair material or cure time. This concept is discussed further in Chapter 7.

6.4 Survey results

Survey measurements are commonly recorded to determine elevation changes (e.g., rutting and settlement, with respect to the pre-traffic baseline elevation. Figure 6.11a illustrates how the resulting slab cross-section elevations would appear if the data were analyzed using the 0-pass elevation as the baseline reference. It is misleading in that it seems the slab settled 1.5 in. with respect to the surrounding slabs since that is usually how these data are interpreted. This approach does not take into account the upheaval that occurred during blasting.

Instead, elevations taken 1 ft into the adjacent slabs on either side at 0 passes were averaged and used as the 0-pass baseline elevation as discussed in Section 3.6.4. This analysis approach, shown in Figure 6.11b, more appropriately accounted for the slab upheaval present and also was useful in determining slab upheaval magnitudes.

Figure 6.11. Comparison of survey rutting measurements for Camouflet 1.

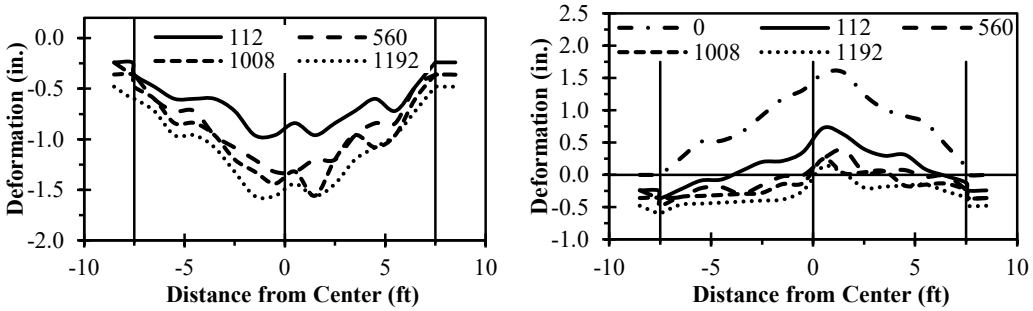

a) Baseline reference was post-blast elevations

b) Baseline reference was pre-blast elevations

Figure 6.12 and Figure 6.13 show mid-point cross-section elevations for all camouflet series at each load cart pass interval. Note that north and south cross sections did not provide any additional insight and were not shown for brevity. Overall, slab upheaval due to blasting ranged from 0.5 to 0.75 in. for Camouflet Series D (16-in. thick concrete) and was in the 1.5- to 2.0-in. range for all other slabs.

This amount of upheaval exceeded the 0.75-in. fighter aircraft criteria discussed in Section 3.6.4. As with the excessive blasting-related cracking discussed in the previous section, these slabs would also classify as failed based on the amount of upheaval and should be removed and replaced with more traditional methods. Again, however, that was not a part of this project, and the camouflet repairs were conducted anyway.

In attempts to alleviate the upheaval issue, attempts were made to seat the slabs in Camouflet Series C using the 4,000-gal water truck with a full tank. Six total passes (i.e., three back-and-forth cycles) were applied to the slabs, and post-seating survey measurements were taken along the centerline. The maximum elevation change at any point along the centerline profile of Series C was 0.1 in., which was not meaningful relative to the total magnitude of upheaval. As anticipated, the seating was not effective, most likely due to sand, debris, and incompressible materials that found its way into the cracks, preventing them from closing.

Figure 6.12. Cross-section rutting measurements for Camouflet Series A and B.

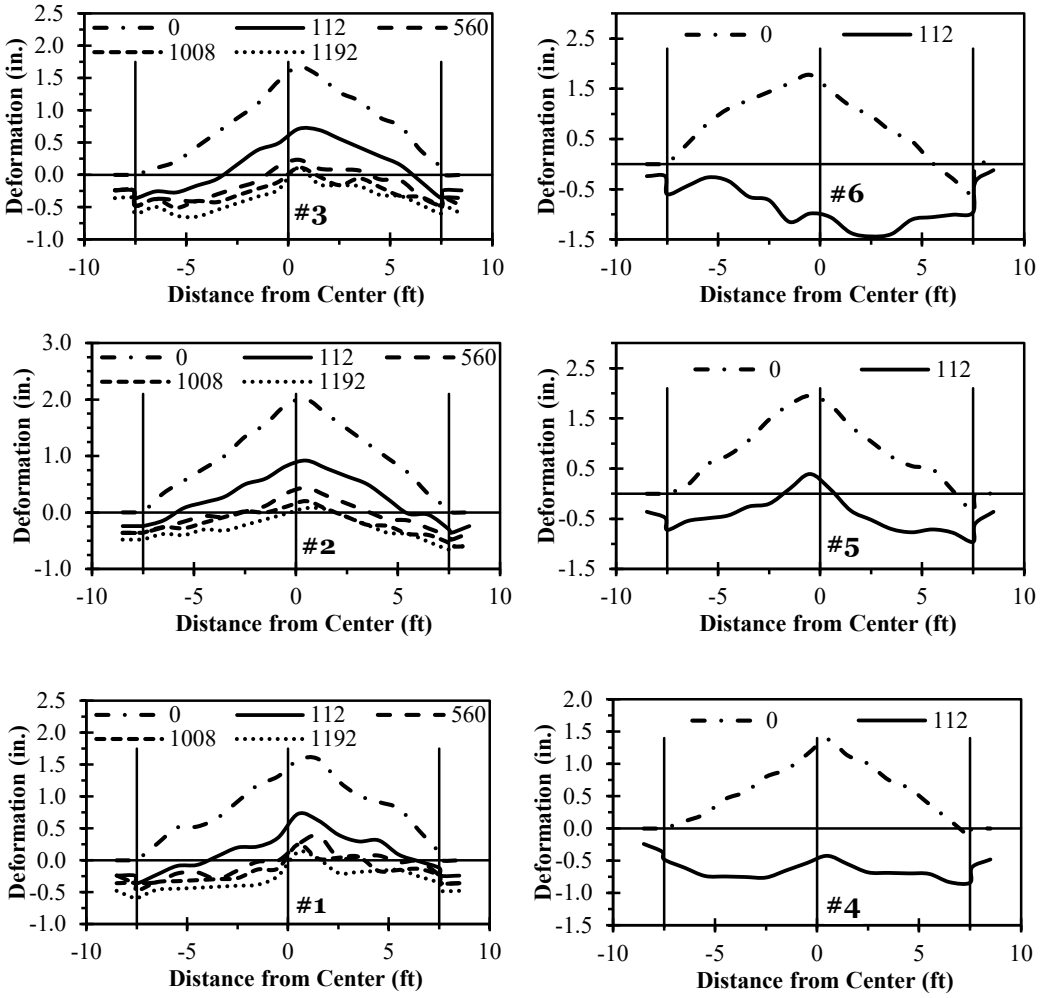

a) Camouflet Series A b) Camouflet Series B

For most camouflets, the load cart trafficking slowly caused the slabs to settle back to near their original elevations. Not only did the elevations decrease, trafficking also had the effect of closing up the main crack running along the centerline of a camouflet series (normally a high-severity crack as shown in Figure 6.7 and Figure 6.8) and removing the accompanying ridge out of the centerline.

Slabs in Camouflet Series B and C exhibited more overall settlement with respect to the surrounding slabs. As seen in Series A and D, a camouflet slab may have settled some but generally so did the adjacent slabs on each side of the camouflet. For Series B and C, slabs often settled more than the adjacent slabs. This settlement likely had to do with the fact that Series B and C slabs were individually poured, probably without dowel bars, meaning there would be relatively little friction in the joint between two

slabs. On the other hand, the Series A and D slabs were poured collectively, meaning joints were partial-depth saw-cut joints (i.e., controlled crack). This would impart at least some load transfer benefit to the camouflet slab (for it to settle, so would the adjacent slabs) that Series C and D slabs would not have.

Figure 6.13. Cross-section rutting measurements for Camouflet Series C and D.

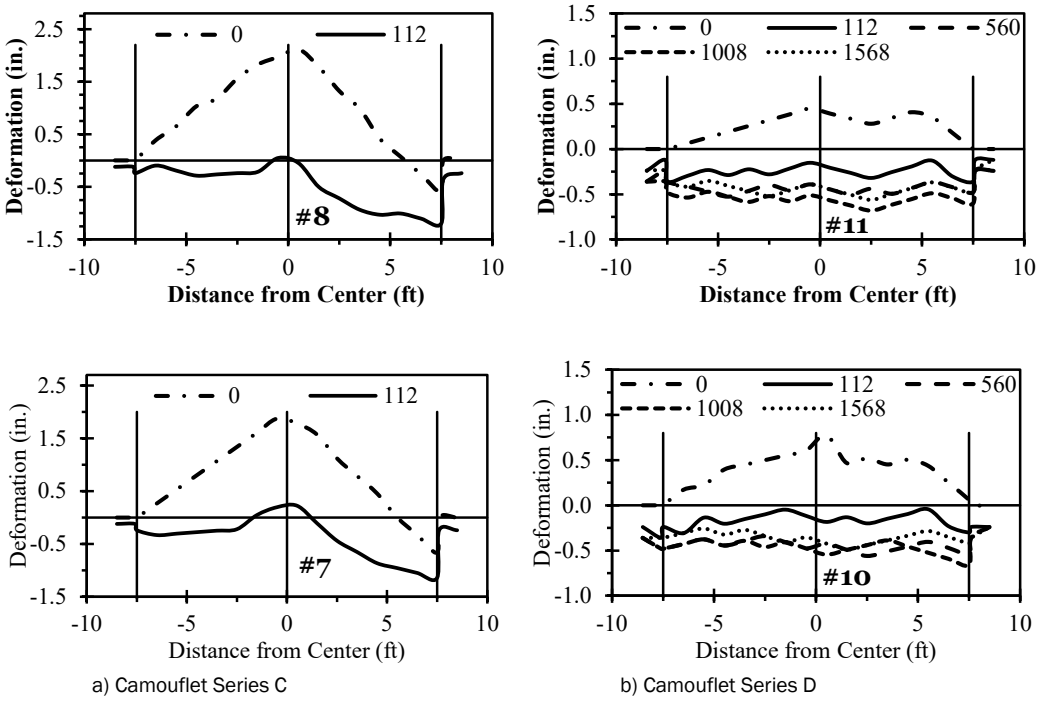

a) Camouflet Series C b) Camouflet Series D

Lastly, Figure 6.14 provides elevations along the profile of each camouflet series. It is necessary to view that data in this format (i.e., as an entire series) because of the upheaval. When it is viewed this way, the combined effect of blasting three camouflets side by side is immediately apparent. As with the cross-section survey measurements, the profile measurements show the slab elevations decreasing under traffic.

Figure 6.14 also suggests all slabs in a series settle a noticeable amount. What Figure 6.14 does not show that must be considered is the fact that Figure 6.14 assumes the elevations of adjacent slabs on either end of a camouflet series were not affected by the blasting. It is likely that these adjacent slabs also exhibited some upheaval, the degree to which is not known. By not taking this into account, Figure 6.14 makes it seem as though an entire series is settling below its initial elevation. This may or may not be the case. It is likely that the entire series did not settle to the degree Figure 6.14 indicates, which would be evident if Figure 6.14 accounted for upheaval of slabs adjacent to the camouflet series.

Figure 6.14. Profile survey rutting measurements for each camouflet series.

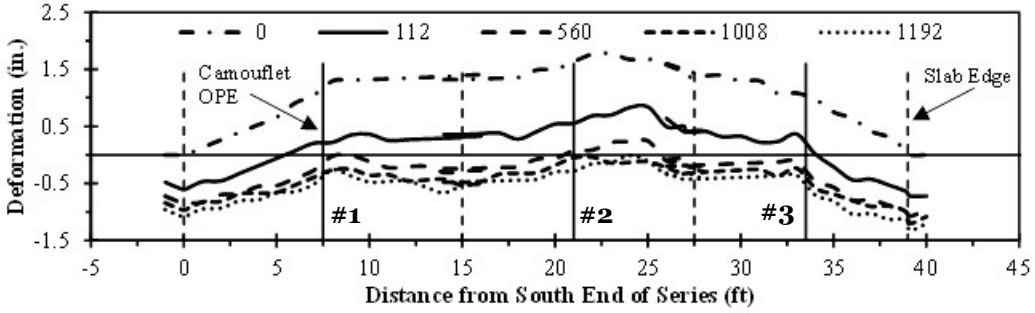

a) Camouflet Series A – 0 to 1,192 passes

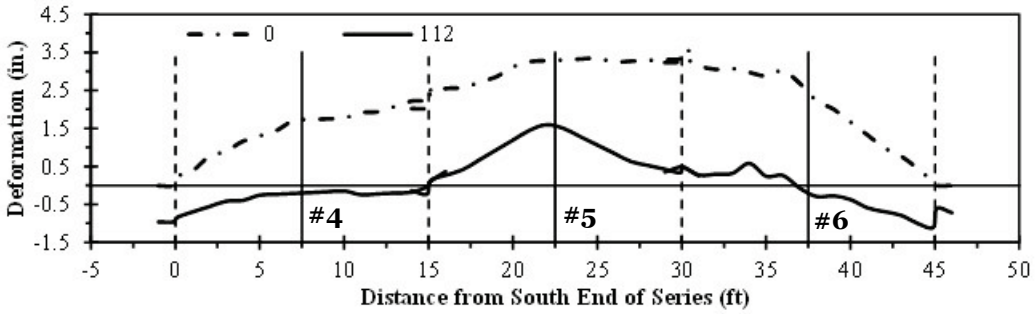

b) Camouflet Series B – 0 to 112 passes

c) Camouflet Series C – 0 to 112 passes

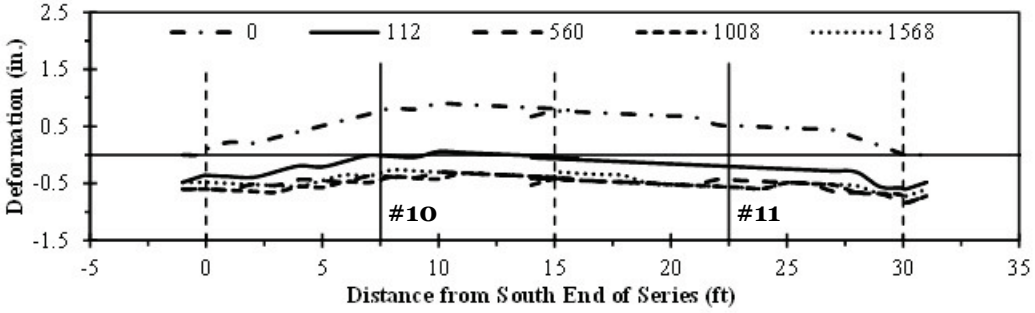

d) Camouflet Series D – 0 to 1,568 passes

6.5 Heavy-weight deflectometer results

All results from HWD testing are presented in Figure 6.15. Though more sophisticated analysis was considered, impulse stiffness modulus (ISM), which is the impulse load (kips) divided by the D_1 deflection (in.), was ultimately reported. Because of the extensive slab cracking present, there were uncertainties regarding the validity of the total deflection basin (i.e., D_1 to D_7) for a given test. It was felt that the most robust analysis that could, not only be reported, but reported with confidence was simply an evaluation of ISM trends.

Figure 6.15. Instantaneous stiffness modulus values for Silver Flag camouflets.

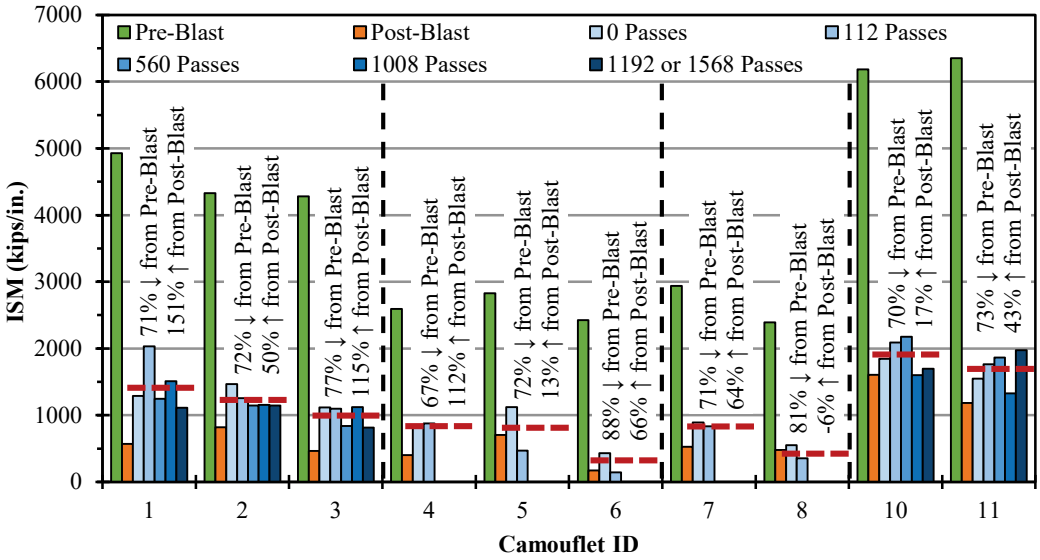

ISM values obtained prior to blasting camouflets appear logical in the sense that Camouflets 10 and 11, where concrete thickness was 16 in., exhibited the highest ISMs (above 6,000 kips/in.), followed by Camouflets 1 to 3 where concrete thickness was about 12 in. and ISMs ranged from 4,000 to 5,000 kips/in. Where concrete thickness was the least (9 to 10 in.) and compressive strengths were approximately half that of the other slabs (consequently, modulus would be much lower, too), ISMs for Camouflets 4 to 8 ranged from 2,000 to 3,000 kips/in.

ISM was drastically affected by the camouflet blasts. Interestingly, the percent reduction in ISM was mostly constant regardless of any one slab's initial ISM value. On average, post-blast ISMs decreased approximately 75% relative to pre-blast values. Percent decrease values ranged from 67% to 88%.

Prior to trafficking, repairs increased ISMs in all cases with varying degrees of effectiveness. For example, ISM increased considerably from post-blast to 0 pass measurements for Camouflet Series A (1, 2, and 3; FF-BU) but only increased slightly for Camouflet Series D (10 and 11; FI-10S).

There did not necessarily appear to be any particular trends in ISM with respect to pass level from 0 to 1,568 passes. Differences observed seemed to be simply variability in the measurements, which is completely probable considering the extent of cracking present and the fact that HWD load plate locations may have varied slightly. Camouflets 5, 6, and 8 are the few exceptions where it is believed the decrease in ISM from 0 to 112 passes was more likely a result of deterioration under traffic rather than variability. Overall, however, the slabs were already too damaged from the blasting to show any meaningful ISM trends with traffic.

For simplicity, the average of all post-repair (i.e., 0 to 1,568 passes) ISMs is shown as a red bar in Figure 6.15. The average post-repair ISMs for Camouflets 1 to 3 and 10 to 11 were all between 1,000 and 2,000 kips/in., while the Camouflet 4 to 8 ISMs were below 1,000 kips/in. Percent increases relative to post-blast conditions were calculated for the average post-repair ISMs. Percent increase ranged from 50 to 151% for Camouflets 1 to 3, from 13 to 112% for Camouflets 4 to 6, from -6 to 64% for Camouflets 7 and 8, and from 17 to 43% for Camouflets 10 and 11.

Overall, HWD testing, as measured by ISM, did indicate the repairs improved the structural support of the slabs with camouflets. As discussed previously in Section 6.4, the extent to which a slab was affected seemed to be less dependent on the repair material or cure time than might be expected. The existing pavement structure (thickness and strength) appeared to be more dominant factors.

6.6 Post-trafficking forensics

After trafficking, one camouflet was selected for excavation to visually evaluate the quality of the repair in a similar manner to which Camouflet 12 was excavated for destructive void characterization. Camouflet 8 was selected for two primary reasons. First, it was one of the worst performers despite being repaired with RSCM, the highest strength repair material evaluated. Second, of all the materials tested, RSCM would be the least likely to flow well into all portions of the camouflet, potentially leaving

voids and pockets. It was reasoned that uncovering the repair may be able to provide some insight to the questions surrounding these reasons.

Figure 6.16 shows the process of unearthing the Camouflet 8 repair. A single cut was made on the north side of the Camouflet 8 slab with the SW45 wheel saw. The slab was already shattered enough from trafficking that the one cut was sufficient to allow the slab to be pulled out in pieces using the CAT M318D bucket. Care was taken to pry pieces of the slab away from the camouflet repair gently to avoid damaging the repair itself.

Figure 6.16. Excavating Camouflet 8 repair.

Figure 6.16b shows a closer view of the repair when it was partially uncovered. Visually, the RSCM appeared to have flowed well and made

good contact with the underside of the overlying concrete slab. There were no visible voids that could be seen. The repair was fully surrounded by base material, which was dug out from around the repair by hand.

The repair itself was approximately 4 ft in diameter and generally resembled the shape of the model that the C-ALS produced (Figure A.11), including the protrusion extending off the lower side of the camouflet. Overall, the repair seemed to have flowed well into the camouflet; the repair seemed sound and did not, by itself, necessarily seem to have been the cause of the camouflet slab's poor performance under traffic.

7 Discussion of Results

This discussion of results focuses primarily on camouflet repair processes and performance. It does not directly discuss repair materials or void characterization since general discussion was provided on these topics in their respective chapters.

The first key step in the camouflet repair process is preparation, which includes estimating the amount of raw repair materials required. In order to do so, some estimate of the total volume of all camouflets to be repaired is needed. Thus, there is some value in being able to appropriately estimate the volume of a camouflet. For a foam repair material such as FI-10S, the accuracy of this volume estimate is likely very important on a per camouflet basis as well as an overall material quantity basis. For cementitious repair materials, an overall material quantity estimate is more important than determining the amount of material required for each individual camouflet.

Under this premise, and with the understanding that FI-10S may not be the most ideal camouflet repair material due to its moisture sensitivity, accurate measurements of camouflet shapes and volumes, such as those the C-ALS provides, are likely unnecessary, especially considering the C-ALS's cost and complexity. Instead, a simpler, quicker solution that provides a more general volume estimate appears to be a more suitable approach. For example, depth from a tape measure alongside a scan with the MLRF to obtain an average radius can be used to calculate an approximate volume quickly. The purpose of this would be to gauge how large the camouflet is on a big picture scale (e.g., the repair requires 1 supersack of FF-BU or 5).

Beyond big picture material quantity estimates, there appears to be little value in accurate per-camouflet volume estimates. It would be more beneficial from a simplicity and time savings perspective to be reactive when filling the camouflet and simply clean up any excess overfilled material. This could be accomplished relatively easily with the tremie funnel adapted with a shutoff valve that would help minimize overfilling.

Regarding the performance of camouflet repairs, results must first be evaluated with discretion simply because the repairs in this project were conducted on slabs that would likely not be suitable candidates for

camouflet repair. The blasting processes used to generate the camouflets resulted in shattered slabs as classified by the PCI system as well as slab upheaval generally in excess of the 0.75-in. criteria for fighter aircraft. Cracking and upheaval would be expected to occur in tandem, meaning attempts to mitigate the upheaval would most likely be countered by particles filling the cracks, as was the case when seating was attempted in this project. With this in mind, repairs in this report were conducted on non-ideal slabs, which may have affected repair performance.

Performance with respect to C-17 load cart trafficking was easily grouped into two categories: Series A and D that sustained over 1,000 passes and Series B and C that sustained only 112 passes. All repair assessment methods (e.g., cracking, HWD testing) supported this finding. Performance trends were not intuitive with respect to repair materials as the two highest-strength materials (FF-CTS and RSCM were on the order of 2 to 20 times stronger than FF-BU and FI-10S) sustained not only fewer passes but significantly fewer passes than the other two materials.

While it is not impossible that weaker materials could withstand more passes, the fact that the weaker materials were so much weaker yet withstood so many more passes is intriguing. Figure 7.1a plots the relationship between load cart passes and strength of the repair material and shows there is a clear inverse relationship. An inverse relationship to this strong of a degree seems unreasonable and is almost certainly being affected by other factors.

Two notable factors that were thought to influence load cart performance were the concrete strength of the existing slabs as well as slab thickness. In contrast to Figure 7.1a, Figure 7.1b and Figure 7.1c show there are clear direct relationships between load cart passes and concrete strength and thickness. It is not surprising that these factors would have some effect on performance, but it is surprising that they controlled performance to the extent that repair material strength had no perceivable impact.

Note that Figure 7.1a should be interpreted in this way. Figure 7.1a should not be taken to mean that a stronger repair material will yield lower performance if all other factors were equal. To illustrate this point, consider the scenario in which the repair materials were assigned to different slabs. For example, if FI-10S was placed in the Series B slabs that were approximately 10 in. thick and 4,000 psi (and likewise for the other

materials), Figure 7.1a would more than likely show a direct relationship rather than an inverse one. Although this assumption cannot be fully vetted without further testing, it is expected that, all other factors being equal, a stronger repair material would provide, if not better, at least more reliable and consistent performance.

Figure 7.1. Relationships between C-17 passes and various project parameters.

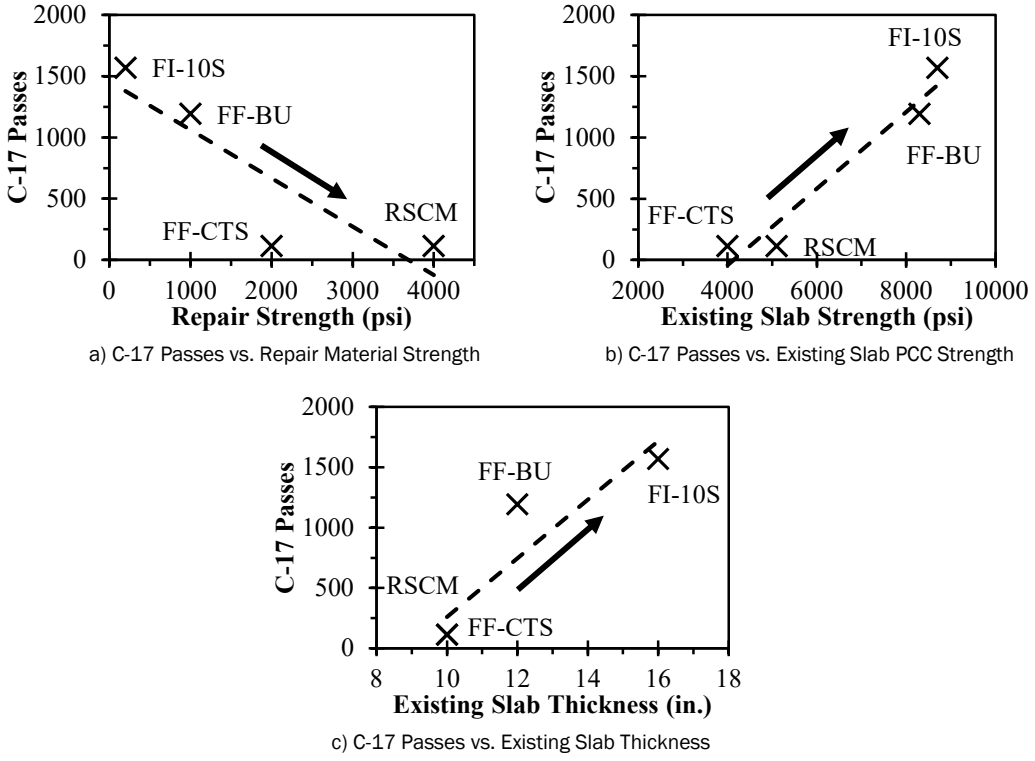

a) C-17 Passes vs. Repair Material Strength

b) C-17 Passes vs. Existing Slab PCC Strength

c) C-17 Passes vs. Existing Slab Thickness

Good repair performance appears possible with any of the tested materials. Though FI-10S exhibited much lower strengths compared to the cementitious materials, it performed well under thick (16 in.) and strong (>8,000 psi) concrete slabs that were not severely heaved (0.5 to 0.75 in.). This thicker, stronger pavement structure is more typical of a conventional concrete airfield than the 10-in. slabs consisting of 4,000 psi concrete. Further, FI-10S is already approved for traditional ADR crater repair with RSCM caps of 10 in. or greater (though these caps would not be classified as shattered slabs like the camouflet slabs). Therefore, FI-10S should be suitable for camouflet repairs so long as the void appears reasonably dry and the existing slabs are not excessively shattered. If FI-10S appears suitable from a strength standpoint, all other materials tested are also suitable.

Cure time was another factor of interest in this project. For typical crater repairs utilizing flowable fill backfill, the flowable fill is given 30 min to cure in order to support construction activities such as the placement of RSCM caps, which are then given 2 hr to cure. For camouflet repairs, because a slab (or cap) is already present and fully cured, the 2.5 hr of total cure time the backfill material receives may be overly conservative.

In this project, there were no noticeable differences between cure times of 30 min, 1 hr, or 2 hr (i.e., all camouflets in a series performed similarly). The only case in which camouflets did not perform similarly throughout the series was for Series B, where the longer cure times fared worse than the shorter cure times and all individuals involved were agreeable that this was more likely due to saturated base conditions than any other factor. As a result, all findings in this project indicate that camouflet repairs could be opened for use after 30 min of curing.

In a typical ADR scenario where a runway was damaged with a mixture of craters and camouflets, the shorter cure time could be of benefit as it would more easily nest within the currently established crater repair staging operation. In a simplified ADR example, after backfilling or capping of the last crater has taken place, the SVM is available for use repairing camouflets, and there are at least 1.5 hr to perform those repairs without affecting the runway opening time (i.e., 2 hr cure time after last crater cap placed minus the 30-min camouflet repair cure time). For camouflets the size of those in this report, each camouflet can be repaired in just a few minutes if repaired one after another. Essentially, crater repairs could be conducted largely as normal, camouflet repairs would follow, and all repairs (craters and camouflets) could be completed in approximately the same amount of time.

8 Conclusions and Recommendations

The objectives of this project were to better characterize attributes of camouflet subsurface voids, to evaluate the suitability of different camouflet repair materials to support cargo aircraft operations, and to evaluate proper construction practices for effectively and efficiently repairing camouflets. These objectives were accomplished through laboratory and full-scale field testing. The following sections provides a list of conclusions developed from testing as well as accompanying recommendations. Appendix B provides a summary of the camouflet repair process recommended as a result of this work for use in an engineering technical letter.

8.1 Conclusions

8.1.1 Repair materials

- In both the laboratory and field, FF-CTS exhibited compressive strengths approximately twice that of FF-BU (approximately 2,000 psi vs. 1,000 psi). FF-CTS exhibited lower workability than FF-BU in the laboratory but greater workability in the field. Flexural strengths decreased for both flowable fills between 1- and 28-day cure times.
- The evaluation of gas-blown foam (i.e., HMI RR401G) did not lead to a viable alternative to FI-10S with respect to moisture insensitivity. Relative to dry-prepared foam, UCS reduction for RR401G was 74% when prepared in a damp state and 89% when prepared in a wet state. Respectively, this was not a meaningful improvement relative to RR401's 93 and 91% UCS reductions for the same preparation states.

8.1.2 Void characterization

- The C-ALS worked well for mapping camouflet voids to visually depict their shapes as well as determine their volumes. For the camouflets tested herein, the C-ALS was generally operating near the lower limit of the laser's distance range, which caused some scatter in the data. This did not appear to be a detrimental factor with the exception of Camouflet 12 where the C-ALS laser was below its lower range limit. The C-ALS is expensive (~$100,000), complex, and delicate.
- Among all tools investigated to characterize camouflet voids (namely, estimate volume), the MLRF was the most reliable tool to measure

camouflet radius, and the plumb bob (or tape measure or similar) was the most efficient to measure camouflet depth.
- Volumes were most appropriately estimated when camouflets were generalized as an ellipsoid whose volume was then multiplied by an adjustment factor of 1.25 to account for general shape irregularities.

8.1.3 Repair processes and performance

- Prior to repairs, camouflet slabs were shattered and generally heaved greater than the 0.75-in. threshold for fighter aircraft simply due to blasting. Attempts to seat slabs below the 0.75-in. threshold with a loaded 4,000-gal water truck were not effective; however, load-cart trafficking eventually settled slabs to near their original elevations.
- Both material transfer solutions tested, the mini hopper and the tremie funnel, were suitable for transferring cementitious materials from the SVM into the camouflet. The tremie funnel was the preferred device and generally resulted in less excess-spilled material.
- FF-BU, FF-CTS, RSCM, and FI-10S all demonstrated the ability to adequately flow and fill the entire camouflet void. This was verified via post-trafficking forensics of a camouflet repaired with RSCM, which would be the most likely material of the four to exhibit flow issues.
- Camouflets 1 to 3 (Series A) and 10 to 11 (Series D) withstood 1,192 and 1,568 passes, respectively, within the time available for testing. Camouflets 4 to 8 (Series B and C) were no longer trafficable after 112 passes.
- Crack development and growth were not related to repair material or cure time.
- Significant settlement beyond settlement to original elevations was not observed in most cases. Some settlement was observed for Camouflet Series B and C due to factors discussed in Section 6.4.
- HWD tests were limited in usefulness because the slabs were shattered. On average, ISM decreased 75% between pre-blast (i.e., normal slab) and post-blast (i.e. camouflet slab) conditions. After repair, ISMs increased anywhere from -6 to 151% relative to post-blast ISMs. There were no apparent trends in ISM with respect to load cart trafficking. Average post-repair ISMs were between 1,000 and 2,000 kips/in. for Series A and D but were less than 1,000 kips/in. for Series B and C.
- For a given repair material, cure time did not noticeably impact repair performance under load cart trafficking as measured by cracking, settlement, or HWD stiffness measurements.

- In-place concrete thickness and strength factors seemed to control camouflet repair performance more than repair material or cure time.
- Ultimately, care should be taken when considering or approving repair materials to not base decisions solely on the number of load cart passes sustained, as this would be misleading.

8.2 Recommendations

8.2.1 Repair materials

- Obtaining and testing additional blends of FF-CTS formulated for lower strength is recommended. Additionally, it is recommended to further investigate the discrepancies between laboratory and field FF-CTS workability.
- The loss in flexural strength from 1 to 28 days for rapid-setting flowable fill materials should be investigated in the event these materials are anticipated for longer-term repairs.
- FF-BU and RSCM are recommended as suitable camouflet repair materials. FF-CTS is more than adequate and capable of being recommended; however, the FF-CTS formulation tested in this project is likely to be modified to lower its strength before a final production formulation is achieved and ready for use.
- FI-10S should be used with discretion. It may be suitable as a void filler (with minimal structural contribution) for concrete pavements that are sufficiently thick or in good post-blast condition. It may be suitable as a structural material if the camouflet void is determined to be dry.
- Because all materials demonstrated the ability to flow and fully fill camouflets, repair material selections should be based, first, on material strengths and then on availability and cost, not on trafficking performance of the camouflets in this report.

8.2.2 Void characterization

- If a detailed assessment of a large camouflet is desired, the C-ALS is recommended as the most suitable tool. If that is the case, it is recommended to work with the vendor to produce a modified and ruggedized C-ALS developed specifically for this purpose, i.e., scanning camouflets rather than underground mines.
- For normal material quantity estimations, it is recommended that both camouflet radius and depth be measured. The MLRF is recommended for quickly determining camouflet radius, and a simpler tool (e.g.,

plumb bob or tape measure) is recommended for determining depth. These measurements can be used to calculate the volume of an ellipsoid (i.e., idealized camouflet) and an adjustment factor of 1.25 can be applied to account for shape irregularities. This procedure is fully outlined in Appendix B.

8.2.3 Repair processes

- For foam repairs, hand mixing appears to be the best material production solution at present. However, foam dispensing systems currently in development by ERDC for crater backfilling are anticipated to present more optimal dispensing systems than previous systems discussed in Section 2.3; the newer systems should be considered as an alternative to hand mixing for foam camouflet repairs.
- For cementitious repairs, the simplified volumetric mixer is recommended for mixing and placing material. In this project, the SVM was primed prior to conducting repairs, a step that is not typically performed for crater repair. It is possible that priming the SVM is unnecessary and should be investigated.
- The tremie funnel is recommended as a material transfer solution for camouflet repairs; the mini hopper is recommended as a secondary alternative.
- It is recommended that a more robust frame be designed to support the tremie funnel that also includes handles for easy manual lifting and fork pockets for lifting with a skid steer or telehandler.
- To facilitate the timely shutoff of material when slightly overfilling a camouflet, it is recommended that the addition of a pull-handle gate valve or similar to the tremie funnel be considered.
- A method for tracking fill level inside the camouflet is needed. At present, the simplest solution recommended is to simply slightly overfill the camouflet and clean any excess material from the surrounding slab.
- It is recommended that 30-min cure times be considered for camouflet repairs in place of the 2-hr cure times used for crater repairs.
- Lastly, a recommended camouflet assessment and repair procedure was drafted based on the findings of this project and is detailed in Appendix B.

References

American Society for Testing and Materials (ASTM). 2016. *Standard test method for compressive strength of cylindrical concrete specimens*. Designation C39/C39M-16. West Conshohocken, PA: American Society for Testing and Materials.

_____. 2015. *Standard test method for flexural strength of concrete (using simple beam with third-point loading)*. Designation C78/C78M-15b. West Conshohocken, PA: American Society for Testing and Materials.

_____. 2013. *Standard test method for time of setting of hydraulic cement by Vicat needle*. Designation C191-13. West Conshohocken, PA: American Society for Testing and Materials.

_____. 2016. *Standard practice for making and curing concrete test specimens in the laboratory*. Designation C192/C192M-16a. West Conshohocken, PA: American Society for Testing and Materials.

_____. 2014. *Standard test method for air content of freshly mixed concrete by the pressure method.* Designation C231/C231M-14. West Conshohocken, PA: American Society for Testing and Materials.

_____. 2008. *Standard test method for time of setting of concrete mixtures by penetration resistance*. Designation C403/C403M-08. West Conshohocken, PA: American Society for Testing and Materials.

_____. 2016. *Standard test method for linear drying shrinkage of concrete masonry units*. Designation C426-16. West Conshohocken, PA: American Society for Testing and Materials.

_____. 2017. *Standard test method for static segregation of self-consolidating concrete using column technique*. Designation D1610/D1610M-17. West Conshohocken, PA: American Society for Testing and Materials.

_____. 2016. *Standard test method for compressive properties of rigid cellular plastics*. Designation D1621-16. West Conshohocken, PA: American Society for Testing and Materials.

_____. 2016. *Standard test method for preparation and testing of controlled low strength material (CLSM) test cylinders*. Designation D4832-16. West Conshohocken, PA: American Society for Testing and Materials.

_____. 2015. *Standard test method for density (unit weight), yield, cement content, and air content (gravimetric) of controlled low-strength material (CLSM)*. Designation D6023-15. West Conshohocken, PA: American Society for Testing and Materials.

_____. 2016. *Standard test method for ball drop on controlled low strength material (CLSM) to determine suitability for load application*. Designation D6024/D6024M-16. West Conshohocken, PA: American Society for Testing and Materials.

_____. 2004. *Standard test method for flow consistency of controlled low strength material (CLSM)*. Designation D6103-04. (Withdrawn 2013). West Conshohocken, PA: American Society for Testing and Materials.

Austin, C. F., C. C. Halsey, and T. E. Eastler. 1984. *Damage-resistant pavement: A state-of-the-art survey*. Report ESL-TR-83-41. China Lake, CA: Naval Weapons Center.

Bell, H. P., L. Edwards, W. D. Carruth, J. S. Tingle, and J. R. Griffin. 2013. *Wet weather crater repair testing at Silver Flag exercise site, Tyndall Air Force Base, Florida*. ERDC/GSL TR-13-42. Vicksburg, MS: U.S. Army Engineer Research and Development Center.

Bull, J. W., and C. H. Woodford. 1996. *The numerical modelling of camouflets to determine their effect on overlaying runways*. 3rd International Conference in Computational Structures Technology, Advances in Finite Element Technology. Budapest, pp. 349-356.

_____. 1998a. Camouflets and Their Effect on Runway Support. *Computers and Structures*, Vol. 69, pp. 695-706.

_____. 1998b. The Prevention of Runway Collapse Following an Underground Explosion. *Engineering Failure Analysis*, Vol. 5, No. 4, pp. 279-288.

_____. 1999. The Effects of Camouflets on Subgrade Surface Support. *Computers and Structures*, Vol. 73, pp. 315-325.

_____. 2000. Stress and Displacement Effects Due to Subsurface Barriers Laid Under Cement Concrete Runways. *Computers and Structures*, Vol. 78, pp. 375-383.

_____. 2001. The Effect of Large Subgrade Voids on the Fatigue Life of Runways. *Computers and Structures*, Vol. 79, pp. 2431-2441.

_____. 2003. The Effect of Increasing the Depth of an Underground Void on the Surface Displacements of an Airfield Runway. In: Bull, J.W. ed. *Numerical Analysis and Modelling in Geomechanics*. New York: Spon Press, pp. 1-25.

Carruth, W. D., L. Edwards, H. P. Bell, J. S. Tingle, J. R. Griffin, and C. A. Rutland. 2015. *Large crater repair at Silver Flag exercise site, Tyndall Air Force Base, Florida*. ERDC/GSL TR-15-27. Vicksburg, MS: U.S. Army Engineer Research and Development Center.

Carruth, W. D., and I. L. Howard. 2016. *Evaluation of flowable fill surface performance*. ERDC/GSL TR-16-33. Vicksburg, MS: U.S. Army Engineer Research and Development Center.

Davis, L. K. 1976. *Vulnerability of airfield runway pavements to conventional munitions*. TR-N-76-2. Vicksburg, MS: U.S. Army Engineer Waterways Experiment Station.

Edwards, L., H. P. Bell, W .D. Carruth, J. R. Griffin, and J. S. Tingle. 2013. *Cold weather crater repair testing at Malmstrom Air Force Base, Montana*. ERDC/GSL TR-13-32. Vicksburg, MS: U.S. Army Engineer Research and Development Center.

Folliard, K. J., D. Trejo, C. Halmen, S. Sabol, and D. Leshchinsky. 2008. *Development of a recommended practice for use of controlled low-strength material in highway construction*. NCHRP Report 597. Washington, DC: Transportation Research Board.

Griffin, J. R., and E. R. Brown. 2011. *Flowable fill for rapid pavement repair*. Transportation Research Record No. 2235. Washington, DC: National Research Council, pp. 88-94.

Gurtowski, L., M. Mejías-Santiago, C. Griggs, J. Johnson, B. Ruiz-Cruz, and D. Felt. 2016. *Refinement of foam backfill technology for expedient airfield damage repair – phase 1: Laboratory evaluation of foam materials*. ERDC/GSL TR-16-16. Vicksburg, MS: U.S. Army Engineer Research and Development Center.

Kyzar, J. D., L. P. Priddy, and J. F. Rowland. 2010. *Field evaluation of the Navy foam dispenser for threat munition crater repair*. ERDC/GSL TR-10-20. Vicksburg, MS: U.S. Army Engineer Research and Development Center.

Priddy, L. P. 2009. *Field evaluation of the Navy injectable foam airfield damage repair concept*. ERDC/GSL TR-09-2. Vicksburg, MS: U.S. Army Engineer Research and Development Center.

_____. 2011. *Development of laboratory testing criteria for evaluating cementitious, rapid-setting pavement repair materials*. ERDC/GSL TR-11-13. Vicksburg, MS: U.S. Army Engineer Research and Development Center.

Priddy, L. P., and W. D. Hodo. 2009. *Constitutive analysis of polyurethane foam composite mixtures: A literature review*. ERDC/GSL SR-09-3. Vicksburg, MS: U.S. Army Engineer Research and Development Center.

Priddy, L. P., and J. K. Newman. 2010. Full-scale field testing for verification of mechanical properties of polyurethane foams for use as backfill in PCC repairs. *Journal of Materials in Civil Engineering* 22(3):245-252.

Priddy, L. P., and T. W. Rushing. 2012. *Development of laboratory testing protocol for rapid-setting cementitious material for airfield pavement repairs*. Transportation Research Record No. 2290. Washington, DC: National Research Council, pp. 89-98.

Priddy, L. P., J. S. Tingle, T. J. McCaffrey, and R. S. Rollings. 2007. *Laboratory and field investigations of small crater repair technologies*. ERDC/GSL TR-07-27. Vicksburg, MS: U.S. Army Engineer Research and Development Center.

Priddy, L. P., C. Moore, and E. Padilla-Salinas. 2008. *Advanced airfield damage repair technologies-phase 1*. ERDC/GSL TR-08-27. Vicksburg, MS: U.S. Army Engineer Research and Development Center.

Priddy, L. P., S. R. Jersey, and R. B. Freeman. 2009. *Determining rapid-setting material suitability for expedient pavement repairs: Full-scale traffic tests and laboratory testing protocol*. Transportation Research Record No. 2113. Washington, DC: National Research Council, pp. 140-148.

Priddy, L. P., S. R. Jersey, and C. M. Reese. 2010a. *Full-scale field testing for injected foam stabilization of portland cement concrete repairs*. Transportation Research Record No. 2155. Washington, DC: National Research Council, pp. 24-33.

Priddy, L. P., M. Mejías-Santiago, and J. F. Rowland. 2010b. *Evaluation of foam backfill technologies for crater repair*. ERDC/GSL TR-10-5. Vicksburg, MS: U.S. Army Engineer Research and Development Center.

Priddy, L. P., J. R. Griffin, and J. S. Tingle. 2011a. *Live-flight certification testing of CRATR technologies, Avon Park Air Force Range, Florida*. ERDC/GSL TR-11-7. Vicksburg, MS: U.S. Army Engineer Research and Development Center.

Priddy, L. P., T. W. Rushing, and J. S. Tingle. 2011b. *Live-flight certification of deployable crater repair technologies*. ERDC/GSL TR-11-1. Vicksburg, MS: U.S. Army Engineer Research and Development Center.

Priddy, L. P., J. S. Tingle, M. C. Edwards, J. R. Griffin, and T. J. McCaffrey. 2013a. *CRATR technology demonstration: Limited operational utility assessment 2, Tyndall Air Force Base, Florida*. ERDC/GSL TR-13-39. Vicksburg, MS: U.S. Army Engineer Research and Development Center.

Priddy, L. P., J. S. Tingle, J. R. Griffin, M. C. Edwards, and T. J. McCaffrey. 2013b. *CRATR technology demonstration: Operational utility assessment, Avon Park Air Force Range, Florida*. ERDC/GSL TR-13-33. Vicksburg, MS: U.S. Army Engineer Research and Development Center.

Priddy, L. P., M. Mejías-Santiago, and J. S. Tingle. 2016. *Development of foam backfill repair techniques for airfield pavement repairs*. Transportation Research Record No. 2569. Washington, DC: National Research Council, pp. 53-61.

Tingle, J. S., L. P. Priddy, M. C. Edwards, C. A. Gartrell, and T. J. McCaffrey. 2009. *CRATR limited operational utility assessment 1 (LOUA1), Tyndall Air Force Base, Florida*. ERDC/GSL TR-09-12. Vicksburg, MS: U.S. Army Engineer Research and Development Center.

Appendix A: Photographs of Camouflet Slabs

Figure A1. Camouflet 1 after blasting and before repair.

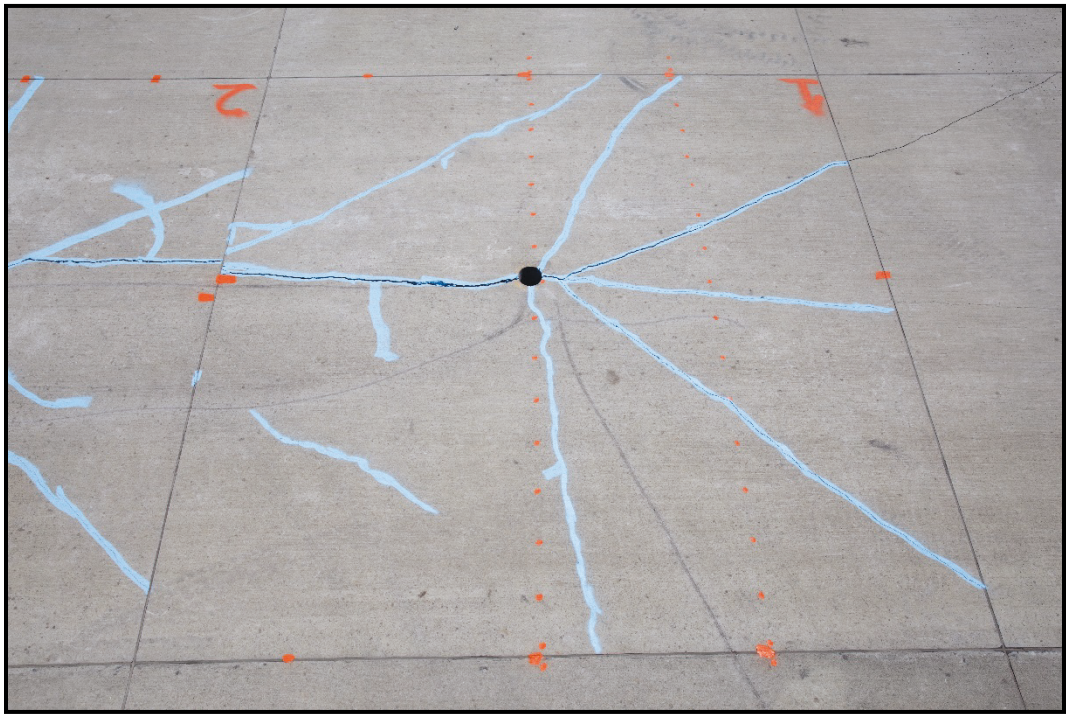

Figure A2. Camouflet 1 after 1,192 passes of the C-17 load cart.

Figure A3. Camouflet 2 after blasting and before repair.

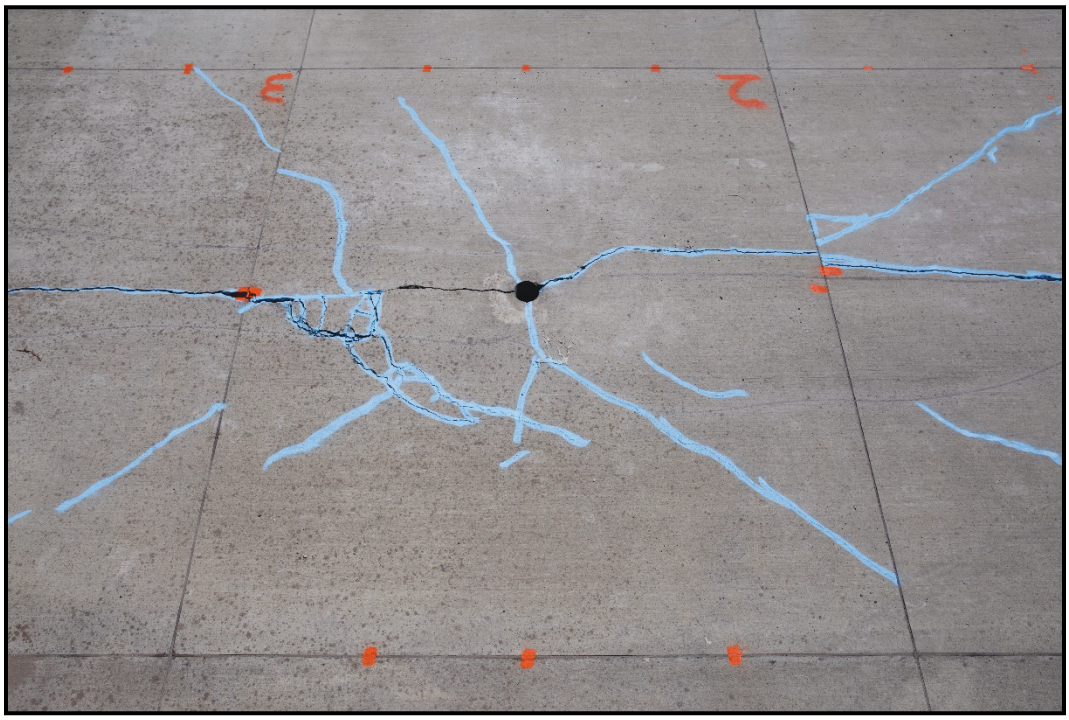

Figure A4. Camouflet 2 after 1,192 passes of the C-17 load cart.

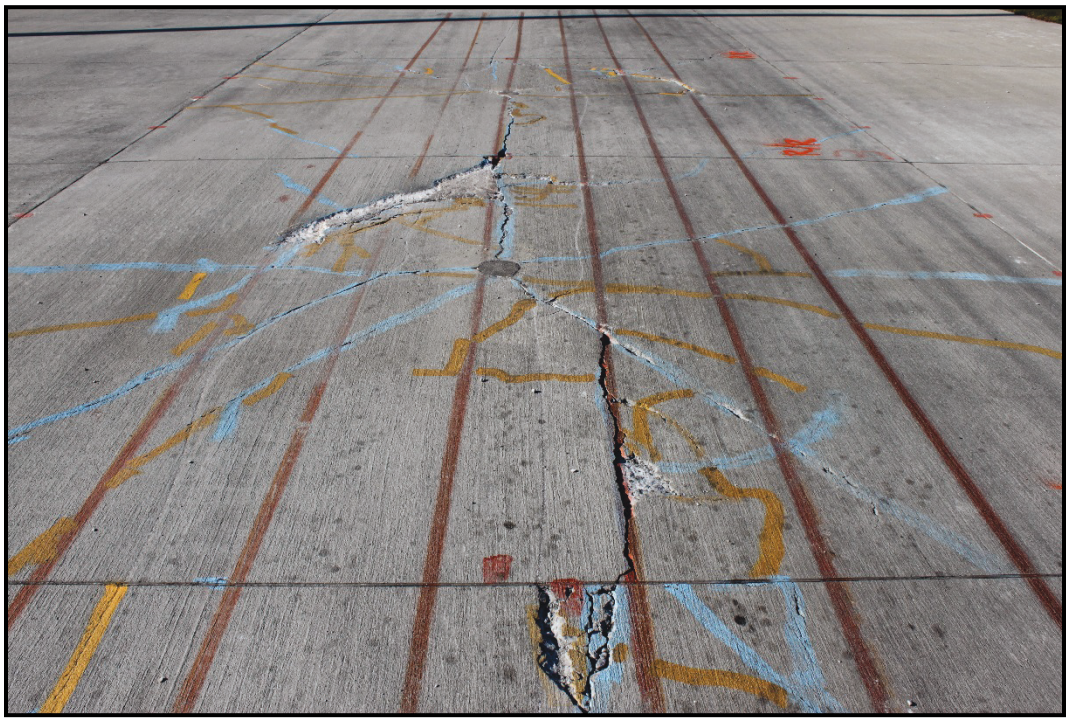

Figure A5. Camouflet 3 after blasting and before repair.

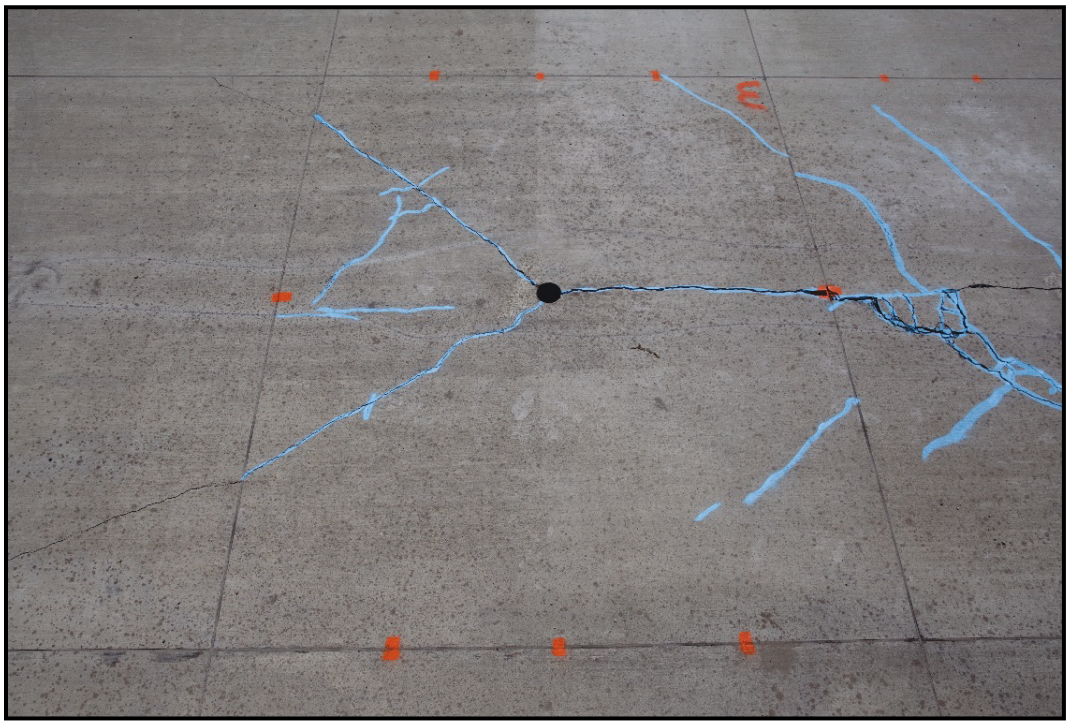

Figure A6. Camouflet 3 after 1,192 passes of the C-17 load cart.

Figure A7. Camouflet 4 after blasting and before repair.

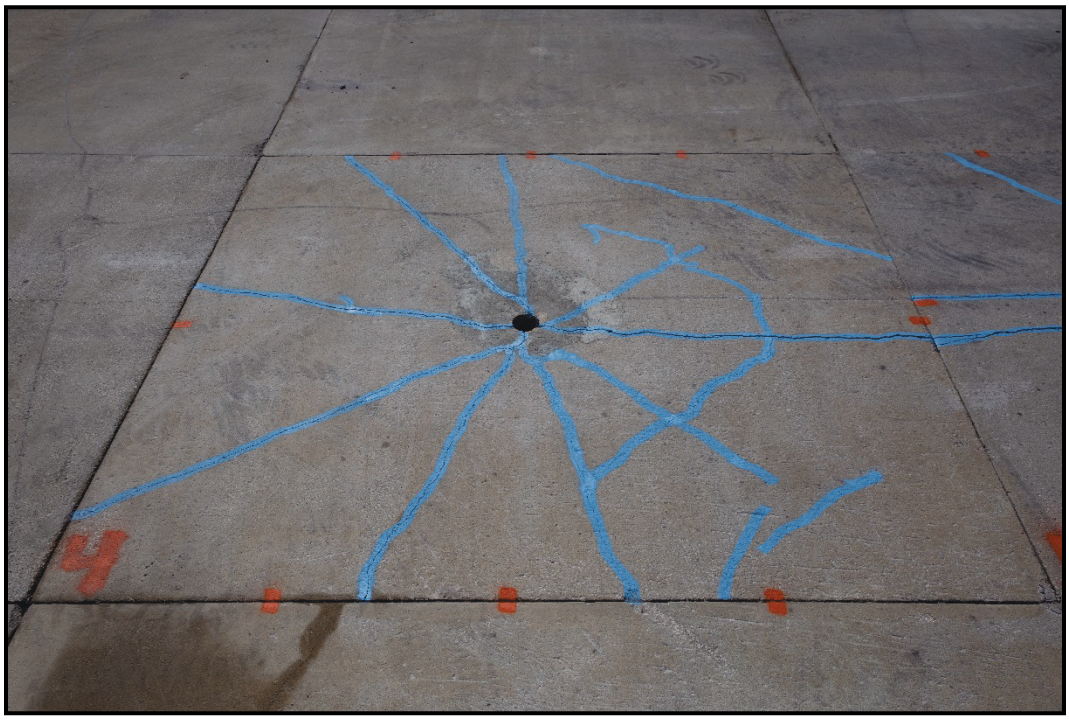

Figure A8. Camouflet 4 after 112 passes of the C-17 load cart.

Figure A9. Camouflet 5 after blasting and before repair.

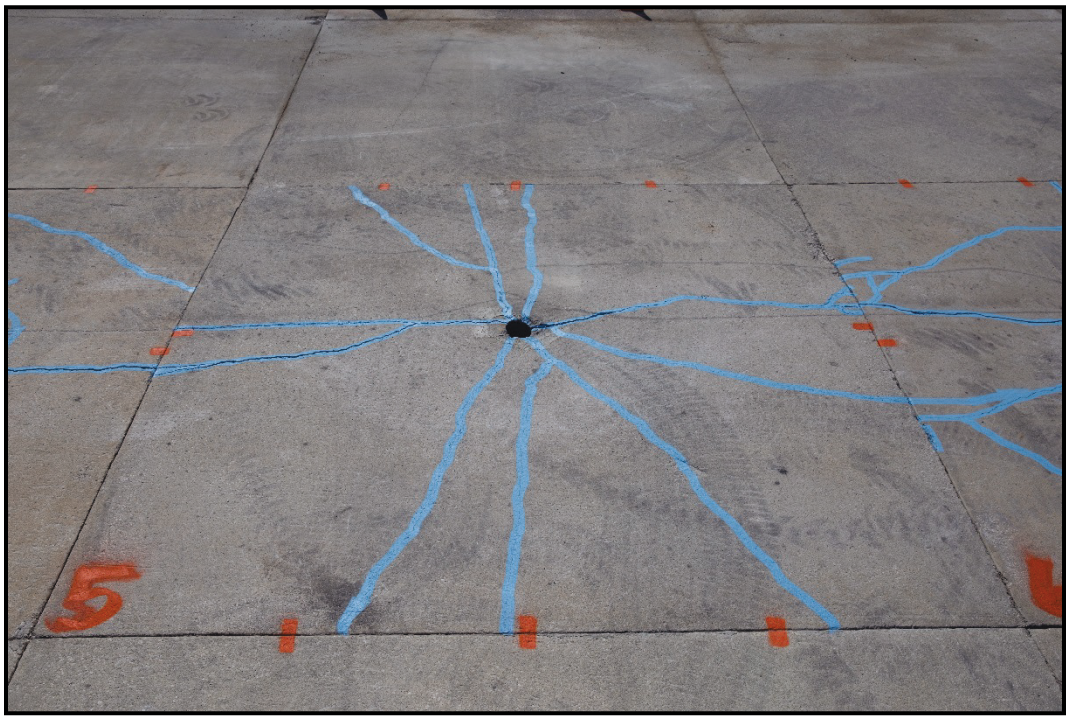

Figure A10. Camouflet 5 after 112 passes of the C-17 load cart.

Figure A11. Camouflet 6 after blasting and before repair.

Figure A12. Camouflet 6 after 112 passes of the C-17 load cart.

Figure A13. Camouflet 7 after blasting and before repair.

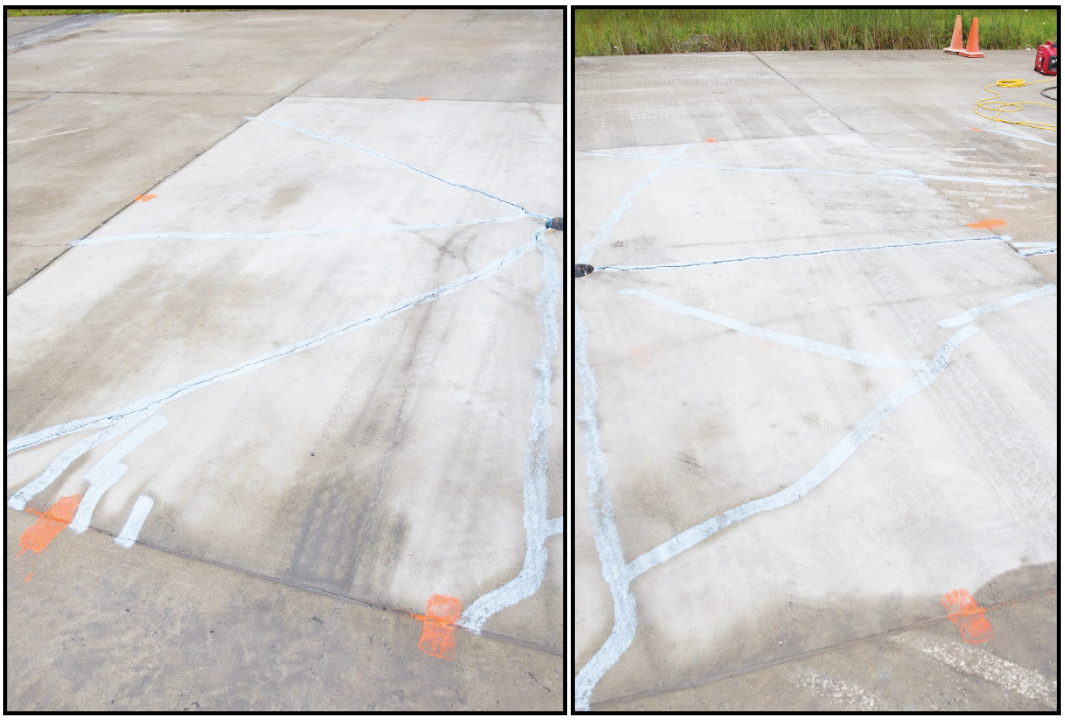

Figure A14. Camouflet 7 after 112 passes of the C-17 load cart.

Figure A15. Camouflet 8 after blasting and before repair.

Figure A16. Camouflet 8 after 112 passes of the C-17 load cart.

Figure A17. Camouflet 10 after blasting and during repair.

Figure A18. Camouflet 10 after 1,568 passes of the C-17 load cart.

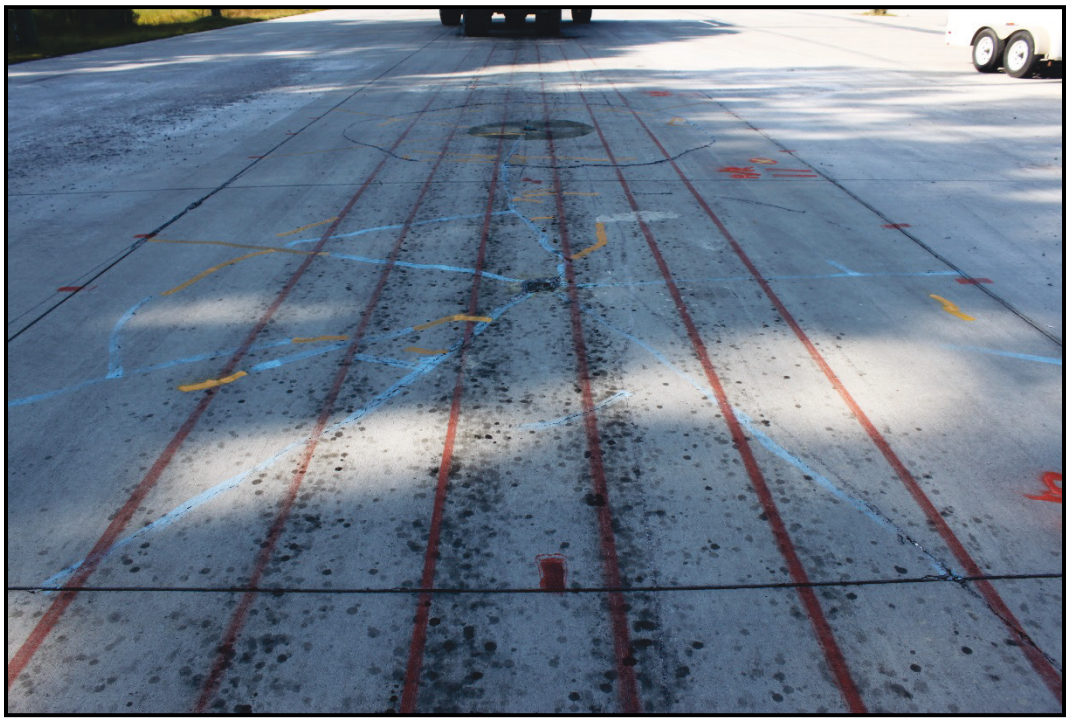

Figure A19. Camouflet 11 after blasting and before repair.

Figure A20. Camouflet 11 after 1,568 passes of the C-17 load cart.

Appendix B: Camouflet Repair Procedure

1. **Assess Camouflet Damage.** Damage caused as a result of the camouflet to the overlying slab must be assessed to determine if camouflet repair procedures can be employed or traditional crater repair procedures are required (i.e., saw-cut and excavate slab, backfill, cap). Traditional crater repair procedures are likely required if (1) the slab is shattered such that it creates a potential FOD hazard, or (2) the slab is heaved upward more than 0.75 in. (fighter aircraft roughness criteria).

2. **Void Characterization.** An estimate of the camouflet void volume is necessary to determine the extent and timing of repair operations as well as an estimate of required material quantities.

   2.1 ***Determine Camouflet Depth.*** Measure the total depth from the pavement surface to the bottom of the camouflet with a plumb bob, tape measure, folding rule, or equivalent. Measure the thickness of the concrete and any observable base material present between the concrete and the camouflet. Subtract the pavement thickness from the total depth to obtain the camouflet depth, H.

   2.2 ***Determine Average Camouflet Radius***. Lower the Modified Laser Range Finder (MLRF) into the camouflet and monitor the real-time distance on the display. Find the depth at maximum radius by adjusting the height of the MLRF until the distance on the display is at its maximum. Lock the MLRF collar to maintain this depth. Rotate the MLRF taking a minimum of 4 measurements at 90° intervals. More densely spaced measurements can be taken and are preferred. Since measurements are saved in the MLRF memory or sent to a Bluetooth-enabled device, little additional effort is required to process a greater number of measurements. Average the recorded radius measurements to obtain the average camouflet radius, A.

   2.3 ***Estimate Camouflet Volume.*** Use camouflet depth, H, and average radius, A, to determine camouflet volume. This can be accomplished using Equation 1 or Table 1. The volume is

calculated by idealizing the camouflet as an ellipsoid with depth, H, and radius, A, and then applying an adjustment factor of 1.25 to the ellipsoid volume to account for shape irregularities between the idealized ellipsoid and a realistic camouflet. Note that for material quantity estimates, it may be desired to multiply the camouflet volume estimate by 1.10 (or a similar factor) to obtain a more conservative estimate to ensure sufficient material quantities are requested.

$$V = AF\left[\frac{4}{3}\pi\left(A^2\frac{H}{2}\right)\right] \quad \textbf{(1)}$$

Where:

V = estimated camouflet volume (ft^3)
AF = adjustment factor to account for shape irregularities between an ellipsoid and a camouflet, 1.25
A = average camouflet radius (ft)
H = total depth of camouflet (ft)

Table B1. Camouflet volumes for given A and H.

	Estimated Camouflet Volume (ft^3) by Depth, H (ft)											
A (ft)	0.25	0.50	0.75	1.0	1.5	2.0	2.5	3.0	3.5	4.0	4.5	5
0.50	0.2	0.3	0.5	0.7	1.0	1.3	1.6	2.0	2.3	2.6	2.9	3.3
0.75	0.4	0.7	1.1	1.5	2.2	2.9	3.7	4.4	5.2	5.9	6.6	7.4
1.0	0.7	1.3	2.0	2.6	3.9	5.2	6.5	7.9	9.2	10.5	11.8	13.1
1.5	1.5	2.9	4.4	5.9	8.8	11.8	14.7	17.7	21	24	27	29
2.0	2.6	5.2	7.9	10.5	15.7	21	26	31	37	42	47	52
2.5	4.1	8.2	12.3	16.4	25	33	41	49	57	65	74	82
3.0	5.9	11.8	17.7	24	35	47	59	71	82	94	106	118
3.5	8.0	16.0	24	32	48	64	80	96	112	128	144	160
4.0	10.5	21	31	42	63	84	105	126	147	168	188	209
4.5	13.3	27	40	53	80	106	133	159	186	212	239	265
5.0	16.4	33	49	65	98	131	164	196	229	262	295	327

-- Volumes reported in this table were calculated by Equation 1 using an adjustment factor of 1.25.

3. **Material Selection.** Traditional crater repair materials have been evaluated for use in camouflet repair procedures. Rapid-setting flowable fill (Buzzi Unicem Utility Fill 1-Step 750) and rapid-setting concrete (CTS Rapid Set® Concrete Mix) are both suitable repair materials that have demonstrated (1) the ability to be placed with the Simplified Volumetric Mixer (SVM), (2) adequate strength

characteristics even when placed in less than ideal conditions, and (3) adequate flow characteristics needed to fully fill camouflets.

Rigid polyurethane foam, such as Foam-iT! 10 SLOW, is less versatile as it is sensitive to the presence of moisture and exhibits lower strengths. If necessary, foam should only be used with sound judgment and where overlying concrete slabs are (1) considerably thick (e.g., 10 in. or greater), (2) composed of high-strength concrete (e.g., greater than 5,000 psi), or (3) located outside the minimum operating strip (MOS) area.

Beyond these considerations, other material availability, logistics, and economic considerations may also be considered.

4. **Site Preparation.** Prior to conducting a camouflet repair, various preparations must be made, many of which are similar to steps in traditional crater repair procedures. The area around the camouflet should be cleared of debris. For cementitious repairs, the SVM should be prepared for production (e.g., water tanks filled, material bin loaded with supersacks of repair material, auger sprayed with release agent, etc.). If available, a CTL with a bucket attachment is useful for cleaning excess material that overfills the camouflet. Various tools typical of concrete work should be acquired (e.g., square-nose shovels, push broom, trowel, concrete immersion vibrator, etc.) The material transfer device (e.g., tremie funnel) should be prepared. For foam repairs, appropriate mixing containers and tools should be acquired.

5. **Repair Process.**

   5.1 ***Cementitious Materials.*** Rapid-setting flowable fill and concrete should be placed with the SVM following operating procedures for typical crater repairs. The water pump gear selector should be set to the speed corresponding to either flowable fill or concrete. The auger should be lowered to an angle of approximately 15°. An initial SVM gate setting of 6 is suggested. Lower gate settings are likely desirable in order to produce a more fluid mix so long as segregation does not become an issue. Lower gate settings will result in a slightly weaker material but will be compensated by the fact that the

material is more flowable and will better ensure all areas of the camouflet void are filled.

A material transfer device such as the tremie funnel is required to direct material from the SVM into the camouflet hole. One person should operate the SVM and begin filling the camouflet, while a second person should watch the camouflet hole to monitor the camouflet fill level. When the camouflet is filled, the funnel operator should, after first allowing a small amount of excess material to overflow the camouflet, close the valve on the funnel outlet and signal to the SVM operator to cease production.

An immersion-style concrete vibrator should be inserted into the camouflet to consolidate the material and aid it in flowing into all areas of the camouflet void. Care should be taken to avoid over-vibrating the material as this may segregate the mix. If the level of material falls below the pavement surface upon consolidation, excess material around the camouflet hole should be pushed into the hole to return the fill level to flush with the surrounding pavement. A trowel may be used to create a smooth finish on the repair material in the camouflet hole, and the remaining excess should be removed with shovels and brooms.

5.2 ***Foam Materials.*** Unless a camouflet is very large, hand mixing of foam in 5-gal buckets with an electric drill and paddle attachment is recommended. Foam-iT! 10 SLOW expands approximately 6 times its liquid volume; therefore, a 4.5-gal batch of liquid foam mixed in a 5-gal bucket can fill approximately 3.5 ft^3 when expanded. For a camouflet with a 2.0-ft depth and 1.5-ft radius equaling 15.7 ft^3 of volume (Table 1), this would require approximately 4.5 batches of foam to be mixed.

Foam components A and B are to be mixed at a 1:1 ratio by volume. Components should be measured into separate buckets and then combined into a mixing bucket immediately prior to mixing. The foam should be mixed vigorously for 1 min and then quickly poured into the camouflet. To prevent upheaval of the slab, it is recommended to add one batch of foam to the

camouflet at a time and allow it to expand. While one batch of foam is expanding inside the camouflet, the next batch, if required, can be batched and mixed. Batching and mixing foam on plastic sheeting or a tarp will facilitate site cleanup.

The actual amount of foam the camouflet will allow may vary from the estimated amount if the volume estimate was incorrect or if moisture is present in the camouflet and the foam overreacts. While the estimated number of foam batches is useful for estimating material quantities, ultimately, foam should continue to be introduced into the camouflet one batch at a time until it expands out of the camouflet. Once set, the excess foam can be removed by shearing it at the pavement surface with a CTL bucket.

In critical areas such as where high-tire-pressure fighter aircraft will be operating, it is recommended that some foam be removed from the camouflet hole and replaced with a suitable patching material. The depth of this patch should extend a minimum of 6 in. below the pavement surface but should ideally be equivalent to the thickness of the parent slab.

6. **Repair Curing.** Cementitious materials and foam materials (to a lesser degree) gain strength with time and, therefore, require a minimum curing time to support aircraft loads. Each camouflet repair should be allowed a 30-min cure time before being subjected to aircraft traffic.

Appendix C: Modified Laser Range Finder Drawings

Detailed drawings of the modified laser range finder are provided in this appendix to facilitate reproduction. Original drawings are scaled to print on ANSI D-size sheets and may be provided electronically upon request. Drawings herein have been compressed to print in this report.


FRONT VIEW
SCALE 1:4
TOP VIEW
SCALE 1:4
SIDE VIEW
SCALE 1:4
ISOMETRIC VIEW
SCALE 1: 2
DRAWINGS PREPARED FOR ANSI D-SIZE SHEET
SHEET ID
G-101
MODIFIED LASER RANGE FINDER (MLRF)
SHEET TITLE 2
U.S. ARMY CORPS OF ENGINEERS
GEOTECHNICAL AND STRUCTURES LAB
3909 HALLS FERRY ROAD
VICKSBURG, MS 39180
DESIGNED BY
J. DESIGNER
DRAWN BY
S. SPANGLER
CHECKED BY:
J. CHECKER
SUBMITTED BY:
J. SUBMITTER
SIZE
ANSI D
ISSUE DATE:
SOLICITATION NO.:
CONTRACT NO.:
MARK
DESCRIPTION
DATE
US Army Corps of Engineers

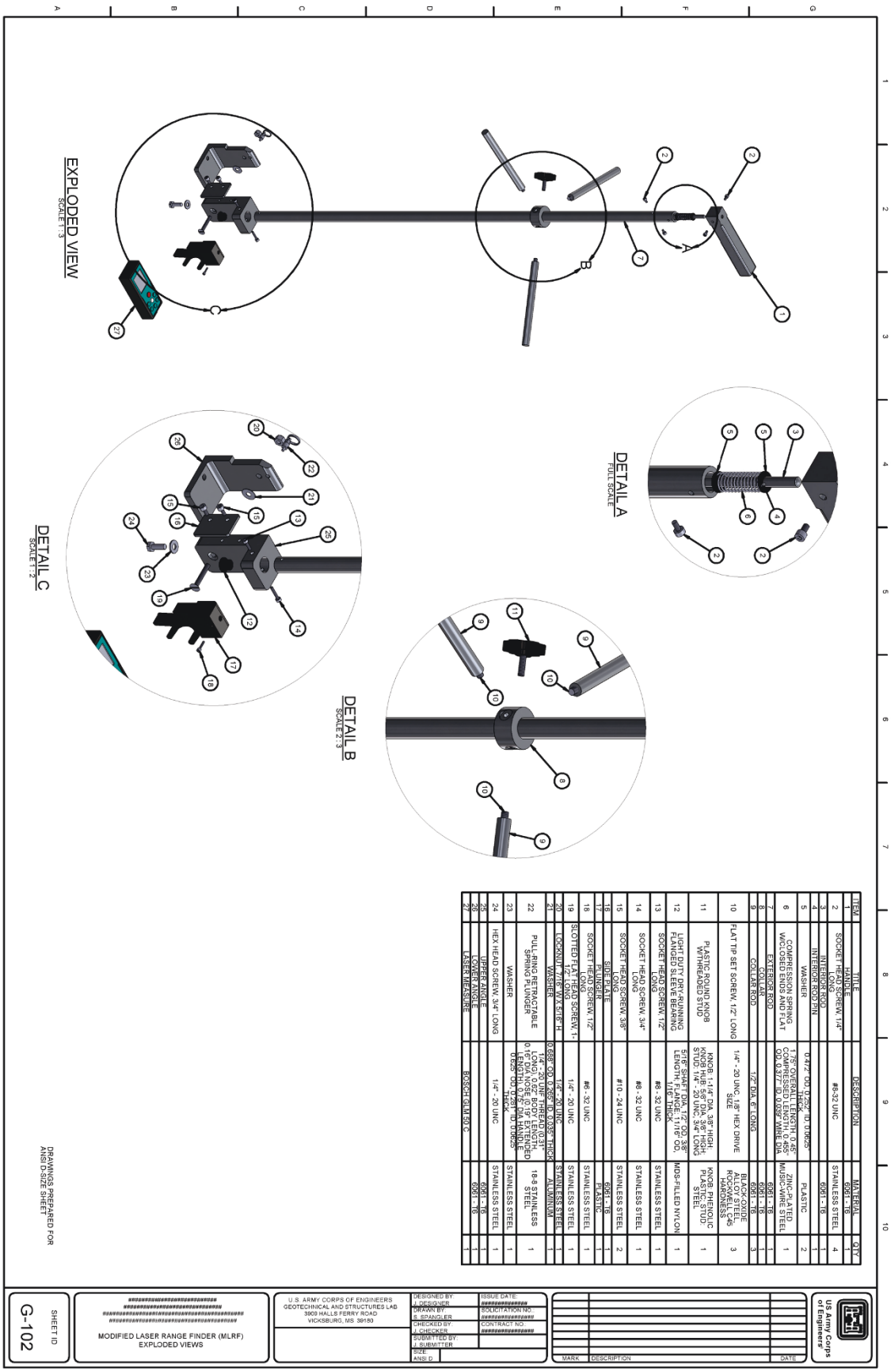

ITEM	TITLE	DESCRIPTION	MATERIAL	QTY
1	HANDLE		6061 - T6	1
2	SOCKET HEAD SCREW, 1/4" LONG	#8-32 UNC	STAINLESS STEEL	4
3	INTERIOR ROD		6061 - T6	1
4	INTERIOR ROD PIN	0.472" OD, 0.250" ID, 0.062" THICK	PLASTIC	2
5	WASHER	1.75" OVERALL LENGTH, 0.45" COMPRESSED LENGTH, 0.054" OD, 0.007" WIRE DIA	ZINC-PLATED MUSIC-WIRE STEEL	1
6	COMPRESSION SPRING W/CLOSED ENDS AND FLAT		6061 - T6	1
7	EXTERIOR ROD		6061 - T6	1
8	COLLAR	1/2" DIA, 6" LONG	6061 - T6	1
9	COLLAR ROD		6061 - T6	3
10	FLAT TIP SET SCREW, 1/2" LONG	1/4"- 20 UNC, 1/8" HEX DRIVE SIZE	BLACK OXIDE ALLOY STEEL, ROCKWELL C45	3
11	PLASTIC ROUND KNOB W/THREADED STUD	KNOB: 1-1/4" DIA, 3/8"-HIGH; KNOB HUB: 5/8" DIA, 3/8"-HIGH; STUD: 1/4" - 20 UNC, 3/4" LONG	KNOB: PHENOLIC PLASTIC; STUD: STEEL	1
12	LIGHT DUTY DRY-RUNNING FLANGED SLEEVE BEARING	5/16" SHAFT DIA, 1/2" OD, 3/8" LENGTH, 1/16" THICK FLANGE	MOS-FILLED NYLON	1
13	SOCKET HEAD SCREW, 1/2" LONG	#8 - 32 UNC	STAINLESS STEEL	1
14	SOCKET HEAD SCREW, 3/4" LONG	#8 - 32 UNC	STAINLESS STEEL	1
15	SOCKET HEAD SCREW, 3/8" LONG	#10 - 24 UNC	STAINLESS STEEL	2
16	SIDE PLATE		6061 - T6	1
17	SIDE PLATE		PLASTIC	1
18	SOCKET HEAD SCREW, 1/2" LONG	#8 - 32 UNC	STAINLESS STEEL	1
19	SLOTTED FLAT HEAD SCREW, 1-1/4" LONG	1/4" - 20 UNC	STAINLESS STEEL	1
20	LOCKNUT, TYPE WX STYLE H	0.688" OD, 0.266" ID, 0.035" THICK	STAINLESS STEEL	1
21	WASHER	1/4" - 20 UNC	ALUMINUM	1
22	PULL-RING RETRACTABLE SPRING PLUNGER	LONG: 0.75" BODY LENGTH, 0.16" DIA NOSE @ 0.19" EXTENDED LENGTH, 0.28" PULL HANDLE	18-8 STAINLESS STEEL	1
23	WASHER		STAINLESS STEEL	1
24	HEX HEAD SCREW, 3/4" LONG	1/4" - 20 UNC	STAINLESS STEEL	1
25	UPPER ANGLE		6061 - T6	1
26	LOWER ANGLE		6061 - T6	1
27	LASER MEASURE	80/SCH 316L-50-C		1

DRAWINGS PREPARED FOR ANSI D-SIZE SHEET

US Army Corps of Engineers

MARK	DESCRIPTION	DATE

U.S. ARMY CORPS OF ENGINEERS
GEOTECHNICAL AND STRUCTURES LAB
3909 HALLS FERRY ROAD
VICKSBURG, MS 39180

DESIGNED BY: J. DESIGNER	ISSUE DATE: ##########
DRAWN BY: S. SPANGLER	SOLICITATION NO.: ##########
CHECKED BY: J. CHECKER	CONTRACT NO.: ##########
SUBMITTED BY: J. SUBMITTER	
SIZE: ANSI D	

MODIFIED LASER RANGE FINDER (MLRF)
EXPLODED VIEWS

SHEET ID
G-102

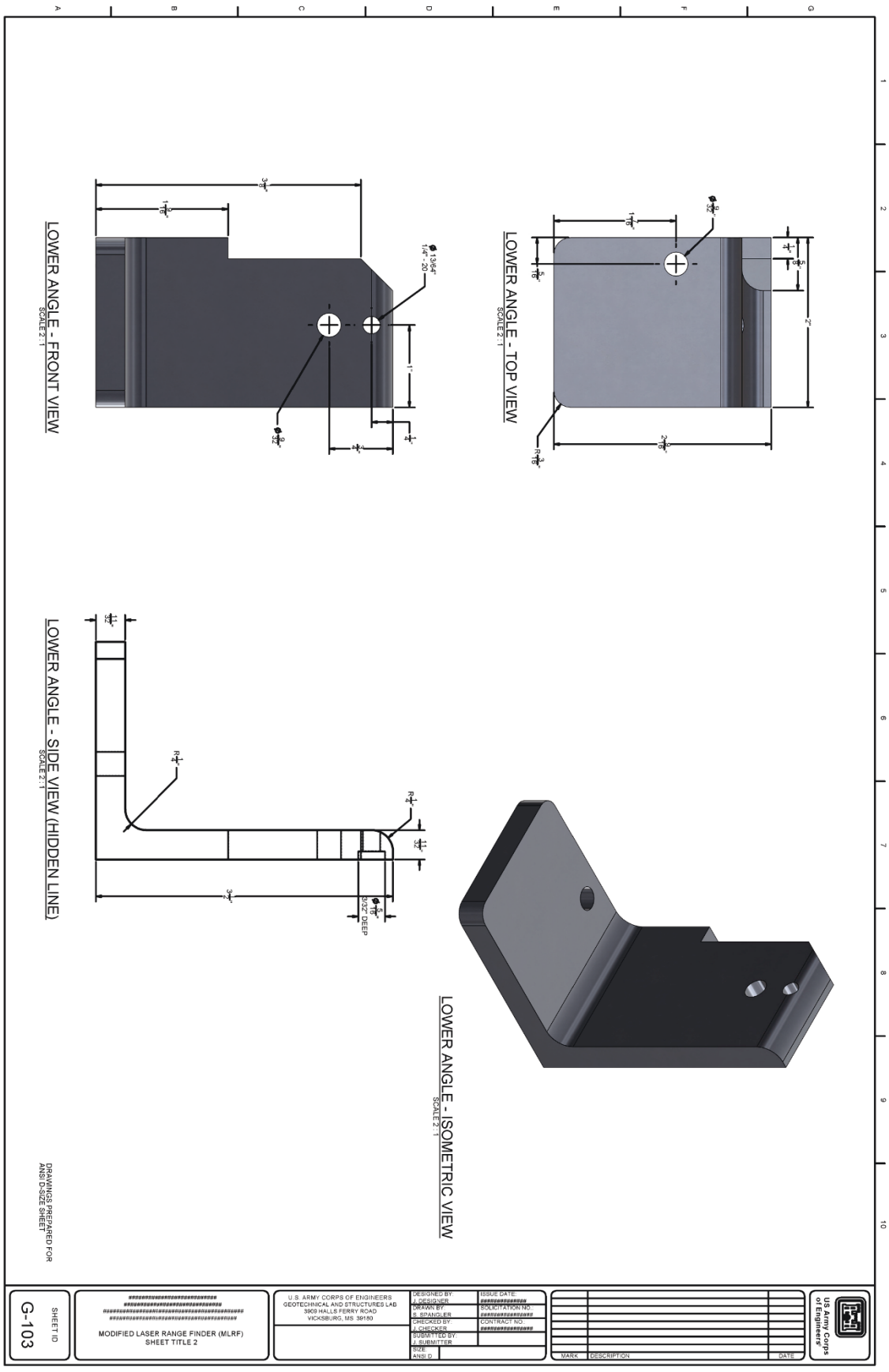
LOWER ANGLE - FRONT VIEW
SCALE 2 : 1
LOWER ANGLE - TOP VIEW
SCALE 2 : 1
LOWER ANGLE - SIDE VIEW (HIDDEN LINE)
SCALE 2 : 1
LOWER ANGLE - ISOMETRIC VIEW
SCALE 2 : 1
DRAWINGS PREPARED FOR ANSI D-SIZE SHEET
MODIFIED LASER RANGE FINDER (MLRF)
SHEET TITLE 2
U.S. ARMY CORPS OF ENGINEERS
GEOTECHNICAL AND STRUCTURES LAB
3909 HALLS FERRY ROAD
VICKSBURG, MS 39180
SHEET ID
G-103
US Army Corps of Engineers

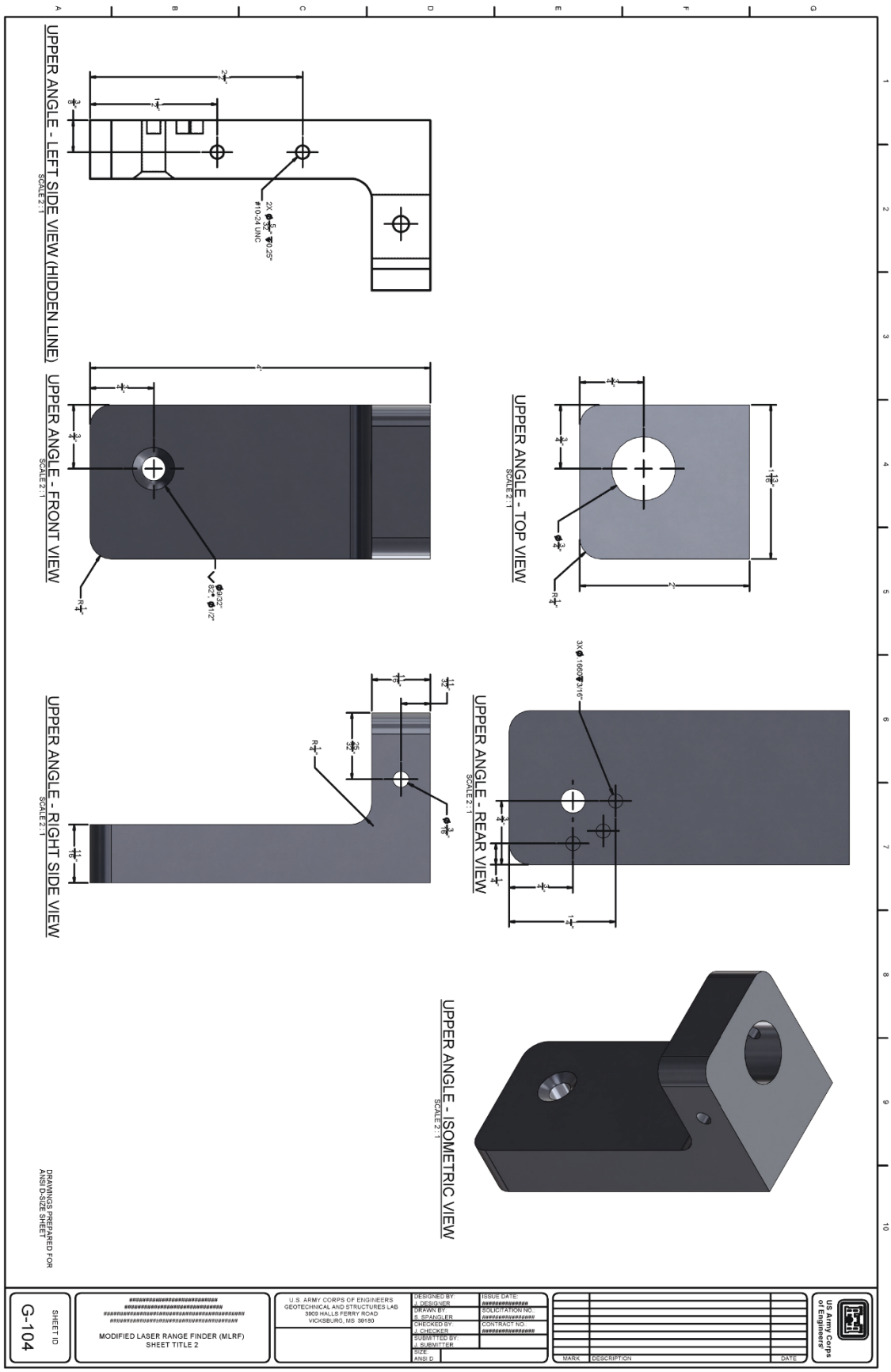
UPPER ANGLE - LEFT SIDE VIEW (HIDDEN LINE)
SCALE 2:1
UPPER ANGLE - FRONT VIEW
SCALE 2:1
UPPER ANGLE - TOP VIEW
SCALE 2:1
UPPER ANGLE - REAR VIEW
SCALE 2:1
UPPER ANGLE - RIGHT SIDE VIEW
SCALE 2:1
UPPER ANGLE - ISOMETRIC VIEW
SCALE 2:1
MODIFIED LASER RANGE FINDER (MLRF)
SHEET TITLE 2
G-104
U.S. ARMY CORPS OF ENGINEERS
GEOTECHNICAL AND STRUCTURES LAB
3909 HALLS FERRY ROAD
VICKSBURG, MS 39180
US Army Corps of Engineers
DRAWINGS PREPARED FOR ANSI D-SIZE SHEET

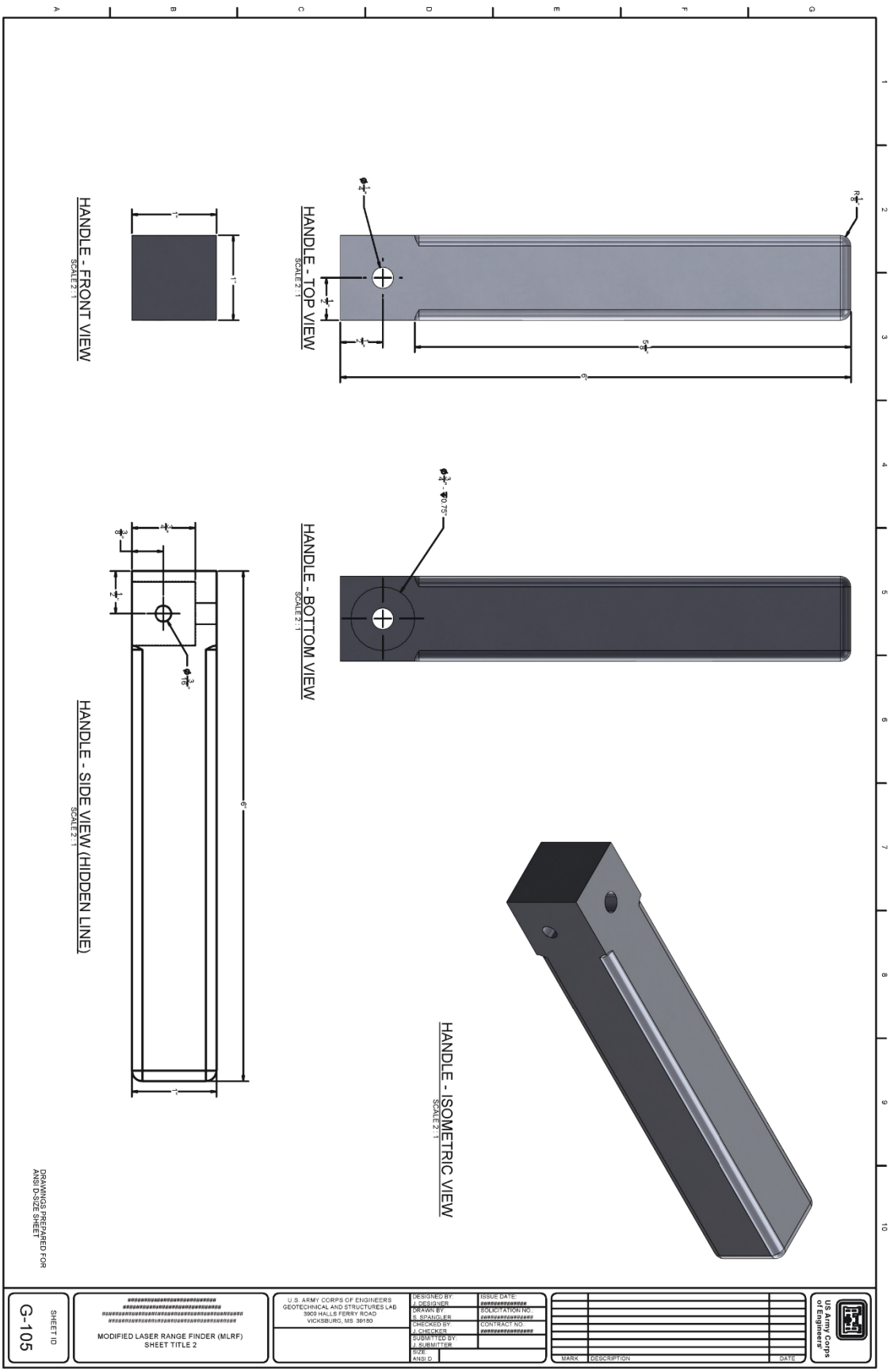
HANDLE - FRONT VIEW
SCALE 2 : 1
HANDLE - TOP VIEW
SCALE 2 : 1
HANDLE - BOTTOM VIEW
SCALE 2 : 1
HANDLE - SIDE VIEW (HIDDEN LINE)
SCALE 2 : 1
HANDLE - ISOMETRIC VIEW
SCALE 2 : 1
DRAWINGS PREPARED FOR ANSI D-SIZE SHEET
MODIFIED LASER RANGE FINDER (MLRF)
SHEET TITLE 2
SHEET ID
G-105
U.S. ARMY CORPS OF ENGINEERS
GEOTECHNICAL AND STRUCTURES LAB
3909 HALLS FERRY ROAD
VICKSBURG, MS 39180
DESIGNED BY: J. DESIGNER
DRAWN BY: S. SPANGLER
CHECKED BY: J. CHECKER
SUBMITTED BY: J. SUBMITTER
SIZE: ANSI D
ISSUE DATE: ##########
SOLICITATION NO.: ##########
CONTRACT NO.: ##########
MARK
DESCRIPTION
DATE
US Army Corps of Engineers

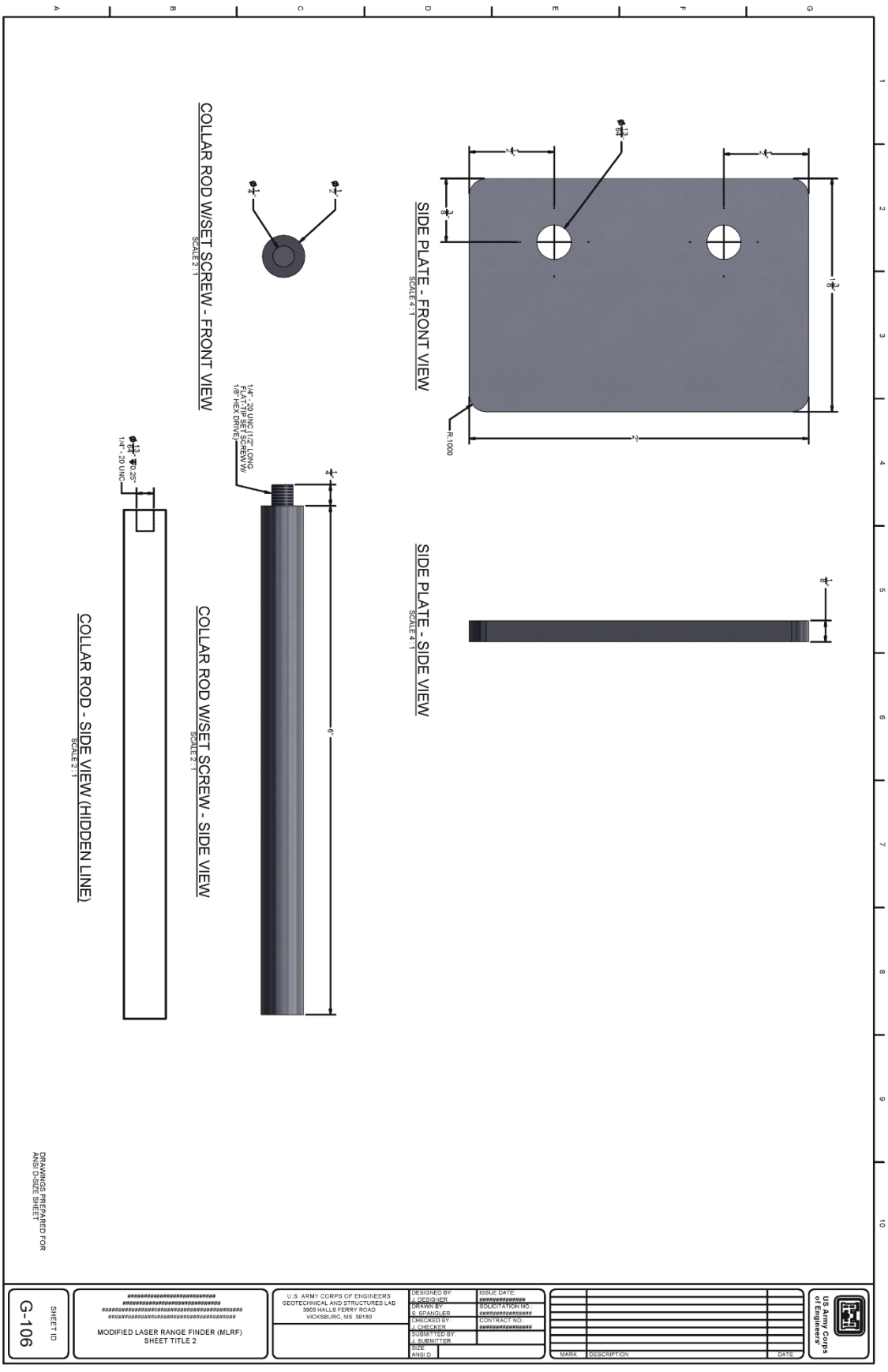
SIDE PLATE - FRONT VIEW
SCALE 4 : 1
SIDE PLATE - SIDE VIEW
SCALE 4 : 1
COLLAR ROD W/SET SCREW - FRONT VIEW
SCALE 2 : 1
1/4" - 20 UNC 1/2" LONG FLAT TIP SET SCREW W/ 1/8" HEX DRIVE
COLLAR ROD W/SET SCREW - SIDE VIEW
SCALE 2 : 1
6"
COLLAR ROD - SIDE VIEW (HIDDEN LINE)
SCALE 2 : 1
1/4 - 20 UNC
0.25"
R.1000
DRAWINGS PREPARED FOR ANSI D SIZE SHEET
MODIFIED LASER RANGE FINDER (MLRF)
SHEET TITLE 2
SHEET ID
G-106
U.S. ARMY CORPS OF ENGINEERS
GEOTECHNICAL AND STRUCTURES LAB
3909 HALLS FERRY ROAD
VICKSBURG, MS 39180
DESIGNED BY: J. DESIGNER
DRAWN BY: S. SPANGLER
CHECKED BY: J. CHECKER
SUBMITTED BY: J. SUBMITTER
SIZE: ANSI D
ISSUE DATE:
SOLICITATION NO.:
CONTRACT NO.:
MARK
DESCRIPTION
DATE
US Army Corps of Engineers

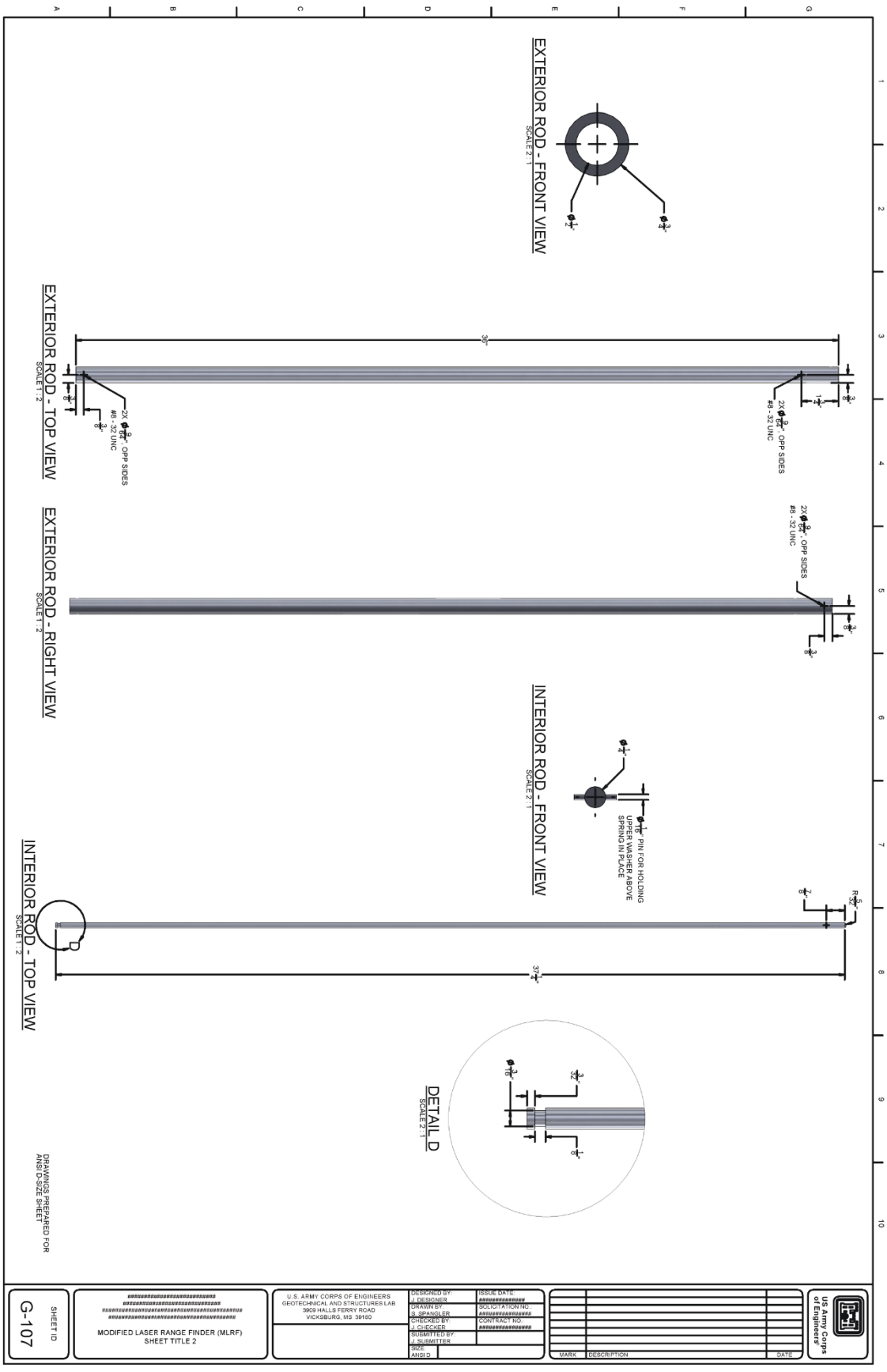
EXTERIOR ROD - FRONT VIEW
SCALE 2 : 1
EXTERIOR ROD - TOP VIEW
SCALE 1 : 2
EXTERIOR ROD - RIGHT VIEW
SCALE 1 : 2
INTERIOR ROD - FRONT VIEW
SCALE 2 : 1
INTERIOR ROD - TOP VIEW
SCALE 1 : 2
DETAIL D
SCALE 2 : 1
35"
37"
2X Ø#8 - 32 UNC, OPP SIDES
PIN FOR HOLDING UPPER WASHER ABOVE SPRING IN PLACE
DRAWINGS PREPARED FOR ANSI D SIZE SHEET
MODIFIED LASER RANGE FINDER (MLRF)
SHEET TITLE 2
G-107
SHEET ID
U.S. ARMY CORPS OF ENGINEERS
GEOTECHNICAL AND STRUCTURES LAB
3909 HALLS FERRY ROAD
VICKSBURG, MS 39180
DESIGNED BY: J. DESIGNER
DRAWN BY: S. SPANGLER
CHECKED BY: J. CHECKER
SUBMITTED BY: J. SUBMITTER
SIZE: ANSI D
ISSUE DATE:
SOLICITATION NO.:
CONTRACT NO.
MARK
DESCRIPTION
DATE
US Army Corps of Engineers

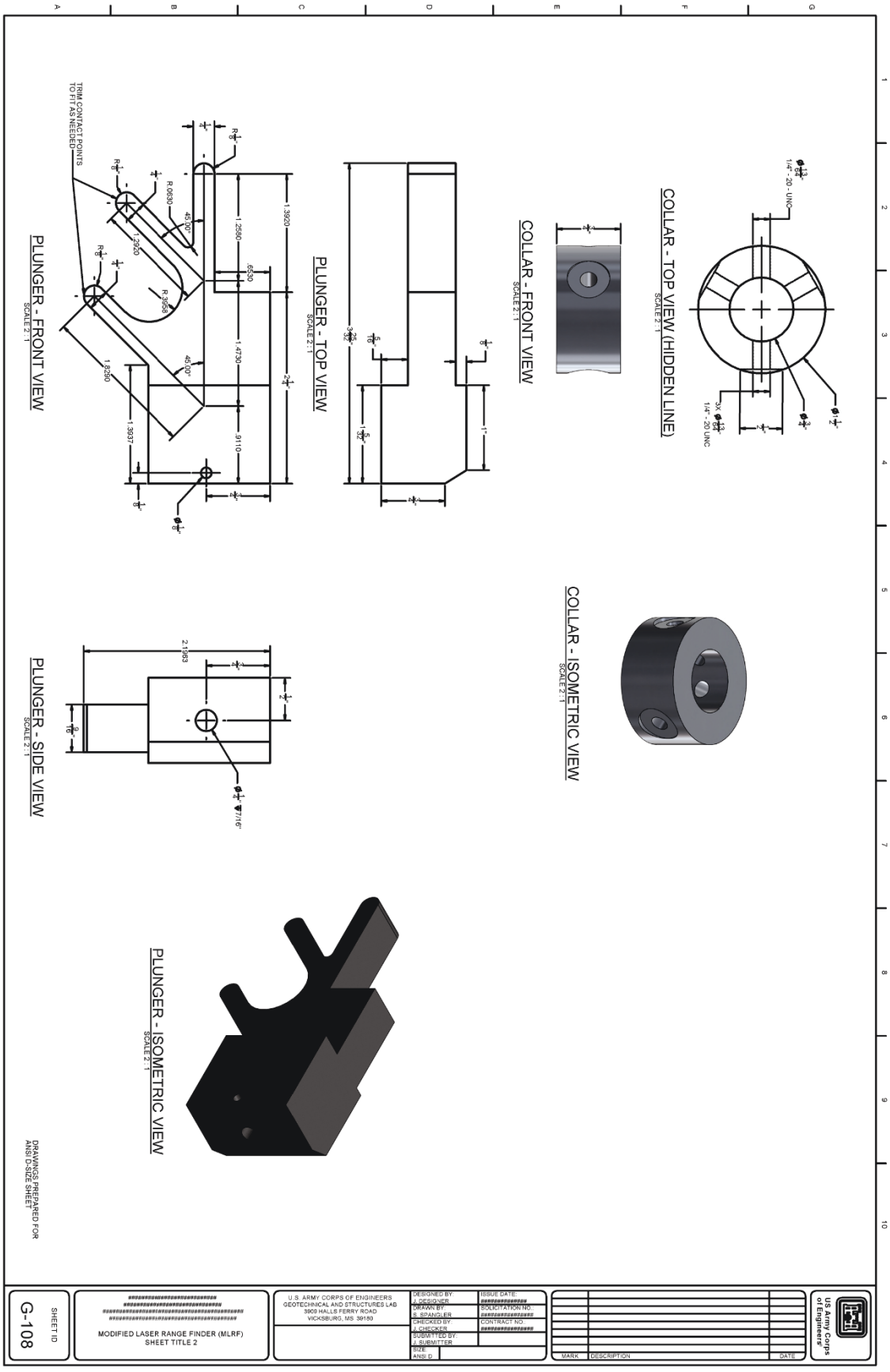
COLLAR - TOP VIEW (HIDDEN LINE)
SCALE 2 : 1
1/4" - 20 UNC
3X
COLLAR - FRONT VIEW
SCALE 2 : 1
COLLAR - ISOMETRIC VIEW
SCALE 2 : 1
PLUNGER - TOP VIEW
SCALE 2 : 1
PLUNGER - FRONT VIEW
SCALE 2 : 1
TRIM CONTACT POINTS TO FIT AS NEEDED
PLUNGER - SIDE VIEW
SCALE 2 : 1
PLUNGER - ISOMETRIC VIEW
SCALE 2 : 1
DRAWINGS PREPARED FOR ANSI D-SIZE SHEET
US Army Corps of Engineers
MARK
DESCRIPTION
DATE
U.S. ARMY CORPS OF ENGINEERS
GEOTECHNICAL AND STRUCTURES LAB
3909 HALLS FERRY ROAD
VICKSBURG, MS 39180
DESIGNED BY: J. DESIGNER
DRAWN BY: S. SPANGLER
CHECKED BY: J. CHECKER
SUBMITTED BY: J. SUBMITTER
SIZE: ANSI D
ISSUE DATE: ##########
SOLICITATION NO.: ##########
CONTRACT NO.: ##########
MODIFIED LASER RANGE FINDER (MLRF)
SHEET TITLE 2
SHEET ID
G-108

REPORT DOCUMENTATION PAGE

Form Approved
OMB No. 0704-0188

1. REPORT DATE *(DD-MM-YYYY)*	2. REPORT TYPE	3. DATES COVERED *(From - To)*
August 2018	Final	

4. TITLE AND SUBTITLE

Camouflet Repair Alternatives

5a. CONTRACT NUMBER

5b. GRANT NUMBER

5c. PROGRAM ELEMENT NUMBER

6. AUTHOR(S)

Ben C. Cox and Thomas A. Carr

5d. PROJECT NUMBER
457442

5e. TASK NUMBER

5f. WORK UNIT NUMBER

7. PERFORMING ORGANIZATION NAME(S) AND ADDRESS(ES)

Geotechnical and Structures Laboratory
U.S. Army Engineer Research and Development Center
3909 Halls Ferry Road
Vicksburg, MS 39180-6199

8. PERFORMING ORGANIZATION REPORT NUMBER

ERDC/GSL TR-18-20

9. SPONSORING / MONITORING AGENCY NAME(S) AND ADDRESS(ES)

Headquarters, Air Force Civil Engineer Center
139 Barnes Avenue, Suite 1
Tyndall AFB, FL 32403-5319

10. SPONSOR/MONITOR'S ACRONYM(S)

11. SPONSOR/MONITOR'S REPORT NUMBER(S)

12. DISTRIBUTION / AVAILABILITY STATEMENT

Approved for public release; distribution is unlimited.

13. SUPPLEMENTARY NOTES

14. ABSTRACT

The inability to operate aircraft on a runway after an attack on an airbase poses significant operational challenges. To address limitations of legacy airfield damage repair (ADR) equipment, materials, and tactics, the U.S. Air Force Air Combat Command began the ADR Modernization program, which eventually transitioned to the Rapid ADR (RADR) program. Within the RADR program, this project's objective was to investigate repair materials and methods for camouflets (i.e., subsurface cavities created by the penetration and detonation of an explosive ordnance).

The objective was accomplished through laboratory testing and full-scale testing at the Silver Flag Exercise Site at Tyndall Air Force Base, FL. A method was developed to quickly provide reasonable camouflet volume estimates. Various repair materials were used to repair simulated camouflets that were trafficked at 30-min to 2-hr cure times with a load cart simulating C-17 aircraft. Repairs sustained 112 passes up to 1,568 passes. Repair performance was controlled primarily by existing concrete slab thickness and strength; repair material strength had no perceivable impact (all other factors being equal, this would not be expected to be the case). Repair performance was not adversely affected for the suggested 30-min cure time.

15. SUBJECT TERMS

Runways – Maintenance and repair
Pavements – Maintenance and repair
Equipment and supplies
Explosions
Blast effect
Cratering

16. SECURITY CLASSIFICATION OF:			17. LIMITATION OF ABSTRACT	18. NUMBER OF PAGES	19a. NAME OF RESPONSIBLE PERSON
a. REPORT	b. ABSTRACT	c. THIS PAGE			19b. TELEPHONE NUMBER *(include area code)*
Unclassified	Unclassified	Unclassified		164	